

Modeling the mass balance of the Morteratsch glacier, Switzerland, using a coupled snow and energy balance model.



Author: W.J.J. van Pelt

Supervisors: dr. C.H. Tijn-Reijmer
prof. dr. J. Oerlemans

January 11, 2010

Abstract

A two-dimensional energy balance model is coupled to a multi-layer snow model in order to simulate the mass balance of the Morteratsch glacier (Switzerland) for the period from 1983 to 2008. The implementation of the snow model enables investigation of the impact of subsurface processes, like refreezing, on the surface mass balance. Meteorological input for the model is derived from measurements at four synoptic stations in the vicinity of the glacier. Weather and mass balance observations on the glacier are used for tuning and validating purposes. The modeled and measured mass balance agree reasonably well. Discrepancies are, besides modeling inaccuracies, most likely caused by uncertainties in the albedo, snow drift and the location of the stake observations. The computed mean specific mass balance is $-0.78 \text{ m w.e. a}^{-1}$. Refreezing of melt and rain water below the surface contributes on average $0.41 \text{ m w.e. a}^{-1}$ to the mass balance. Furthermore, the mean modeled internal accumulation is $0.04 \text{ m w.e. a}^{-1}$, corresponding to 3.5% of the mean accumulation by refreezing and snow fall. Climate sensitivity experiments show that an air temperature deviation of $1 \text{ }^{\circ}\text{C}$ causes a shift in the specific mass balance of $0.63 \text{ m w.e. a}^{-1}$, while a deviation of the precipitation of 10% results in a change of the mass balance of $0.16 \text{ m w.e. a}^{-1}$. The model underestimates the surface temperature on average by $1.7 \text{ }^{\circ}\text{C}$, which is also reflected in the calculated snow temperature profile. The surface temperature is shown to be very sensitive to perturbations in the turbulent fluxes, which leads us to believe that turbulent heat transport towards the surface is currently underestimated.

Contents

1	Introduction	1
2	Observations & data treatment	5
2.1	The Morteratsch area	5
2.2	Observations	7
2.2.1	Measurements around the glacier	8
2.2.2	Measurements on the glacier	8
2.3	Model input	11
2.3.1	Surface topography & grid	11
2.3.2	Data treatment	13
2.3.3	Input values on the grid	13
3	Model description	19
3.1	Theoretical description	19
3.1.1	Energy balance model	20
3.1.2	Multi-layer snow model	29
3.2	Numerical properties	35
3.2.1	Spatial / temporal resolution	35
3.2.2	Numerical methods	37
3.2.3	Calibrating the model	41
3.3	Experiments	42
4	Results	43
4.1	Parameter sensitivity	43
4.2	Components of the mass and energy balance	47
4.2.1	Spatial variations	47
4.2.2	Temporal variations	51
4.3	Subsurface variables	64
4.4	Additional simulations	73
4.4.1	Effect of a changing ice albedo	74
4.4.2	Effect of incorporating the snow model	74
4.5	Climate sensitivity	76
5	Conclusion & discussion	79

Chapter 1

Introduction

Currently, about 10% of the Earth's surface is covered by glacier ice. Small glaciers outside the great ice sheets on Greenland and Antarctica cover an area of about 525×10^3 km², corresponding to only 4% of the total land ice area (Ohmura, 2004; Dyurgerov and Meier, 2005). Nevertheless, melting of these small glaciers (figure 1.1) may have contributed to as much as 30% of sea level rise in the 20th century (Meier, 1984; IPCC, 2007). Small glaciers are mostly situated in rather warm and wet areas, resulting in a higher sensitivity to changes in climate (Oerlemans and Fortuin, 1992).

The relationship between climate variations and the volume and mass balance of glaciers has been studied extensively in the past. Long time-series of mass balance data have proven useful in detecting global climate change and in the explanation of the rising sea level (Kuhn, 1993). The mass balance has been acknowledged as the critical link between glaciers and climate (Meier, 1965) and the importance of glacier monitoring is recognized by the Intergovernmental Panel on Climate Change (IPCC) and the World Glacier Monitoring Service (WGMS). In order to simulate the mass balance, several types of models have been developed that relate the mass balance to climate.

Simple degree-day ablation models relate the melt rate to the mean summer air temperature in order to estimate the annual ablation (Braithwaite, 1995; Hock, 1999). More sophisticated mass balance models evaluate the energy balance of a glacier surface in an attempt to calculate the energy involved in melting (e.g. Arnold *et al.*, 1996; Klok and Oerlemans, 2002; Bougamont *et al.*, 2005). Two-dimensional mass balance models enable calculation of spatial variations in the surface energy fluxes and the mass balance. Several parameters have been shown to have a significant impact on the mass balance. E.g. various studies have demonstrated the importance of accurate simulation of the surface albedo (Oerlemans and Hoogendoorn, 1989; Munro, 1991; Van de Wal *et al.*, 1992).

An other important aspect is to take into account processes acting below the surface. Snow models of varying complexity have been developed in the past to simulate subsurface properties, such as temperature, density and the liquid water content (Jordan, 1991; Greuell and Konzelmann, 1994; Bartelt and Lehning, 2002; Tribbeck *et al.*, 2004). Several studies have shown that the impact of subsurface processes on the surface energy and mass balance cannot be neglected (Rick *et al.*, 2008; Parry *et al.*, 2007; Janssens *et al.*, 2000). Therefore, a coupling between snow models and mass balance models is needed to study



Fig. 1.1: Photograph of the glacier tongue and the recently deglaciated forefield of the Morteratsch glacier, Switzerland (August, 2008).

the impact of density and temperature variations below the surface on the mass balance. Of special interest is the process of refreezing of percolating water, which adds mass to the interior of the glacier and affects the vertical profiles of density, temperature and water content.

For this study, a distributed energy balance model is developed along the lines presented by Klok and Oerlemans (2002). This model is coupled to a multi-layer snow model, based on a routine described by Greuell and Konzelmann (1994), in order to calculate the mass balance of the Morteratsch glacier (Switzerland), while accounting for subsurface processes that affect the energy and mass balance at the surface. The energy balance model computes the surface temperature, for which all the energy fluxes at the surface are in balance. However, the surface temperature cannot be raised above the melting point of ice ($0\text{ }^{\circ}\text{C}$), which may result in a positive energy budget. The excess energy is used for melting of the surface layer. The resulting amount of melt water is used as input for the snow model, which simulates percolation, storage, refreezing and runoff of the water content, while accounting for processes that affect the mass balance either directly or indirectly. Below the surface, accumulation of refrozen water and variations in the subglacial heat flux, which is determined by the distribution of temperature and density, have a significant impact on the mass balance.

Measurements of climate variables around the glacier have been used to calculate input for the model on a two-dimensional grid. On the other hand, the Institute for Marine and Atmospheric research Utrecht (IMAU) has been operating automatic weather stations to measure ice melt, radiative fluxes and weather variables on the glacier. Additionally, stake readings provided information about snow properties and surface melting. The on-glacier observations allowed for tuning and validation of the model.

The evolution of the mass balance is simulated over the period from 1983 to 2008. Several experiments are performed to test the sensitivity of the mass balance and snow properties to perturbations of the model parameters and

to changes in climate variables (temperature and precipitation). Furthermore, additional simulations have been done to investigate the impact of refreezing and the influence of darkening of the ice by debris deposition on the mass balance.

The observations on and around the glacier and the treatment of the data to derive input for the model are described in chapter 2. Chapter 3 gives a theoretical and numerical description of the energy balance model and the snow model. The model results are presented and discussed in chapter 4. Finally, the main conclusions and suggestions for further research are given in chapter 5.

Chapter 2

Observations & data treatment

2.1 The Morteratsch area

The Morteratsch glacier is situated in the Bündner Alps in the southeast of Switzerland, close to the Italian border ($46^{\circ}24'N$, $9^{\circ}56'E$). The valley glacier originates at the northern slopes of the high mountains of the Bernina Range: Piz Bernina (4049 m a.s.l.), Crast Aguzza (3869 m a.s.l.), Piz Zupo (3996 m a.s.l.), Bella Vista (3922 m a.s.l.), Piz Palü (3901 m a.s.l.) and Piz Cambrena (3602 m a.s.l.). The Pers glacier and the Morteratsch glacier flow around a rock formation, called Isla Persa ('Lost Isle'), and right below this rock formation, the two glaciers join and continue as one about 2 km from the snout. In this study, the Pers glacier and the Morteratsch glacier are treated as one, the Morteratsch glacier. With a length of 7 km and an area of about 17 km^2 , the Morteratsch glacier is the largest glacier of the Bernina Range. However, over the last few decades, the glacier tongue has been retreating with an increasing rate of up to 30 meter per year, resulting in a total retreat of about 2 km since the start of the length record in 1878. The large side moraines are still an indication of the glacier thickness at the end of the little ice age in the 19th century, as shown in figure 2.1(c). The Morteratsch glacier is classified as a temperate glacier. Temperate glaciers are at melting point ($0 \text{ }^{\circ}\text{C}$) throughout their mass, except for the layers near the surface. Especially in winter, snow temperatures near the surface may drop to values well below freezing point.

The climatological conditions in the Morteratsch area are strongly variable and they are not only determined by the large scale conditions, but also by processes acting on a smaller scale. The glacier surface itself has a marked influence on the local climate, for example when a glacier wind is established after cooling of the air by the glacier surface. Figure 2.2 shows the wind speed versus the wind direction at the glacier tongue. This figure clearly shows that either a downslope glacier wind (wind direction around 180°) or an upslope valley wind (wind direction around 360°) is present most of time. Rapid changes in temperature, wind and cloudiness are not exceptional in this region and they provide a great challenge to researchers to measure, describe and model the associated processes in a proper way. Over the last few decades, significant progress has



(a)



(b)



(c)



(d)

Fig. 2.1: Photographs of the glacier tongue (a), the AWS at station M1 (b), a large side moraine (c) and the accumulation zone on the northern slopes of the Piz Palü (d). Photographs are taken in August 2008. Note the significant darkening of the ice at the tongue near the side moraines.

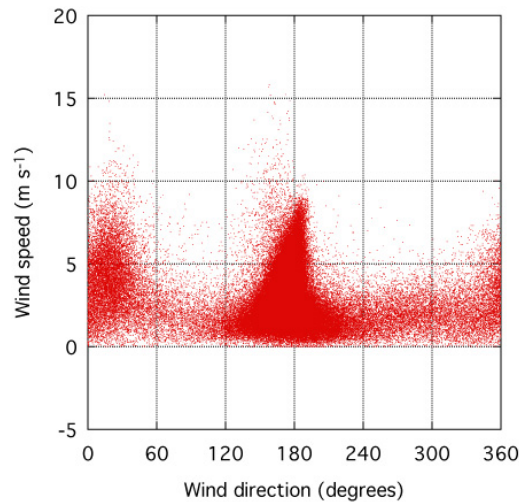


Fig. 2.2: Observed half-hourly mean wind speed versus the wind direction at the glacier tongue (2100 m a.s.l.) for the period from 8 July 1998 to 14 May 2007. A wind direction of 180° corresponds to a southward down-glacier flow.

been made in the understanding of the physics behind the processes that determine the mass and energy balance at the surface. Very useful formulations and parameterizations have been developed, often supported by extensive measurements. These expressions are at the basis of the model developed for this study, since they enable us to calculate the different components of the mass and energy budget using measurements of climatic variables around the glacier.

The equilibrium line is a term used to describe the altitude where the accumulation and ablation are in balance on average over a year. Since the equilibrium line is directly reacting on changes in precipitation and temperature, it is often regarded as an indicator for climate change. At the end of the ablation season, the equilibrium line altitude can roughly be estimated as the height above which snow is still present. The rather steep and rugged terrain above the equilibrium line is called the accumulation zone (positive mass balance) (figure 2.1(d)). On the other hand, the area below the equilibrium line is known as the ablation zone (negative mass balance) (figure 2.1(a)). Super-imposed ice formation in the accumulation zone may lead to an overestimation of the equilibrium line altitude by visual inspection. At the Morteratsch glacier the equilibrium line is located at a height of approximately 3000 m a.s.l..

2.2 Observations

As stated before, weather conditions in mountainous (and glacierized) regions, like the Morteratsch area, can be highly variable in space and time. Therefore, accurate input data of the local weather conditions on the glacier are needed to force the model. Measurements of climate variables *around* the glacier contain valuable information on the large-scale weather conditions. Long time-series observations (since 1981) are available from multiple stations in the vicinity of the glacier. On the other hand, measurements of weather variables *on* the glacier

started in 1995 and are carried out at a single location. The data gathered on the glacier contain more accurate information on the local glacier climate. In spite of this the on-glacier measurements are not used as input for the model, since the shorter time-series observations and the unavailability of climatic data at multiple locations do not allow for determination of reliable input values for the weather conditions on the grid. Instead, the aforementioned observations of the weather variables at stations in the vicinity of the glacier are used to acquire the desired model input. Furthermore, measurements of energy fluxes, snow properties and weather variables on the glacier are used for tuning and validating purposes.

2.2.1 Measurements around the glacier

Meteorological data from four synoptic weather stations in the vicinity of the glacier were provided by MeteoSchweiz. A summary of the measured variables is given in table 2.1. The geographic location and altitude of the measurement sites is shown in figure 2.3. A complete set of data is available since 1983, except for the daily precipitation measurements at Pontresina, which are available since 1989. Therefore, we start our simulations in 1983. Data gathered during the last three months prior to the start of the simulation are used as input for an initialization run. Pressure observations are not available during these three months and therefore an estimated average value is taken as input.

2.2.2 Measurements on the glacier

The Institute for Marine and Atmospheric research Utrecht (IMAU) has been measuring weather variables and ice melt at five different locations since 1995 in order to improve our understanding of the local glacier climate and to study its connection with large scale climate variations. In this study, measurements on the glacier are very important for validation and tuning of the model results. The geographic location of the measurement sites on the glacier is shown in figure 2.4. The first automatic weather station (AWS) was set-up at the glacier tongue at location M1 (± 2110 m a.s.l.) in October 1995 (figure 2.1(b)). In July 1998, the sensors were replaced and new devices, measuring longwave radiation, air pressure and relative humidity, were installed. In order to maintain an approximately constant altitude, the measurement sites have been displaced upstream over short distances every 2 to 3 years. In 2007, the AWS at M1 was getting close to the retreating glacier terminus and the station was therefore moved up over a larger distance to an altitude of around 2300 m a.s.l.. In the present study, only measurements of the AWS at the initial location on the glacier (M1) are used for evaluation. An overview of the observations on the glacier is given in table 2.2.

Stake measurements provide insight in the specific mass balance in the ablation zone. On the Morteratsch glacier, readings of the stakes are done manually about four times a year. Another way to measure the surface height is to make use of a sonic ranger. Sonic rangers simply measure the distance between the device and the glacier surface. Unlike the stake readings, sonic rangers give a more detailed evolution of the surface height, which makes it possible to discriminate between individual snow and melting events. The temperature profile and mean density of the snow pack are measured about 4 times a year

Table 2.1: Observations at stations around the glacier used in this study. The synoptic stations are located at Corvatsch (C), Samedan (S), Bernina-Curtinatsch (BC) and Pontresina (P).

<i>Variable</i>	<i>Station</i>	<i>Time resolution</i>	<i>Starting date</i>
Incoming shortwave radiation	C	10 min	01-01-1981
	S	10 min	01-01-1981
Air pressure	C	10 min	01-01-1983
	S	10 min	01-01-1983
Air temperature	C	10 min	01-01-1981
	S	10 min	01-01-1981
Relative humidity	C	10 min	13-05-1981
	S	10 min	13-05-1981
Precipitation	BC	1 day	01-10-1989
	P	1 day	01-01-1981
	S	10 min	01-01-1981

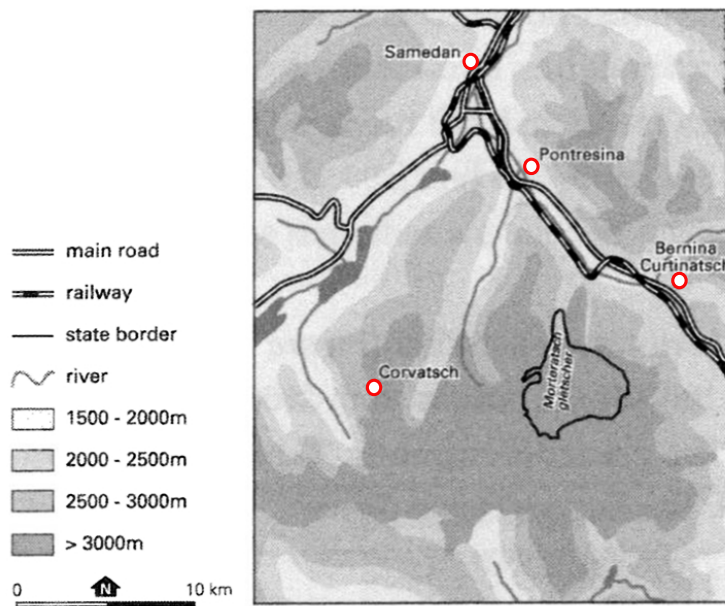


Fig. 2.3: Map of the Morteratsch glacier and its surroundings, showing the location of the synoptic weather stations at Pontresina (1774 m a.s.l.), Bernina Curtinatsch (2095 m a.s.l.), Samedan (1705 m a.s.l.) and Corvatsch (3315 m a.s.l.). The thick black line represents the outline of the glacier [source: Klok and Oerlemans (2002)].

Table 2.2: Overview of the observations on the glacier used in this study.

<i>Variable</i>	<i>Stations</i>	<i>Time resolution</i>	<i>Starting date</i>
Incoming shortwave radiation	M1	30 min	01-10-1995
Outgoing shortwave radiation	M1	30 min	01-10-1995
Incoming longwave radiation	M1	30 min	08-07-1998
Outgoing longwave radiation	M1	30 min	08-07-1998
Air pressure	M1	30 min	08-07-1998
Air temperature	M1	30 min	01-10-1995
Relative humidity	M1	30 min	08-07-1998
Ice melt / snow depth (stakes)	M1	irregularly	16-12-1995
	M2	irregularly	21-10-2005
	M3	irregularly	02-08-1999
	M4	irregularly	02-08-1999
	M5	irregularly	20-10-2000
Ice melt (sonic ranger)	M1	30 min	01-10-1995
Snow depth (sonic ranger)	M1	30 min	01-10-1995
Snow temperatures	M1	irregularly	19-11-1997
Snow density	M1	irregularly	16-12-1995

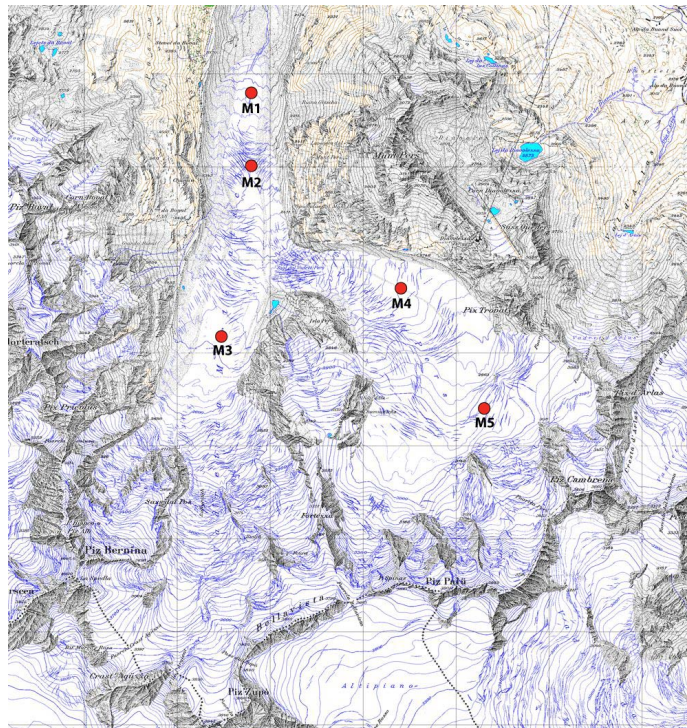


Fig. 2.4: Map of the Morteratsch glacier. The thick black line marks the boundaries of the glacier and the red dots indicate the locations of the IMAU measurement sites at M1 (2110 m a.s.l.), M2 (2270 m a.s.l.), M3 (2500 m a.s.l.), M4 (2700 m a.s.l.) and M5 (2910 m a.s.l.) [source: Swisstopo].

Table 2.3: Mean observations at M1 over the period from 8 July 1998 to 14 May 2007. T_{atm} is the air temperature, RH is the relative humidity, p_{air} is the air pressure, SW_{in} is the incoming shortwave radiation, α is the albedo, LW_{in} is the incoming longwave radiation and LW_{out} is the outgoing longwave radiation. Values for the extrema and the standard deviation are based on half-hourly averages, except for the wind speed and the albedo, which are based on daily averages. The albedo is determined as the ratio of the outgoing and incoming solar radiation; the mean measured snow depth is derived from measurements with the sonic ranger.

<i>Variable</i>	<i>Mean</i>	<i>Minimum</i>	<i>Maximum</i>	<i>Standard Deviation</i>
T_{atm} ($^{\circ}\text{C}$)	1.5	-21.9	19.1	7.1
RH (%)	62.5	1.9	100.0	19.4
p_{air} (mbar)	788.1	753.4	807.1	7.3
Wind speed (m s^{-1})	3.0	0.0	15.8	1.7
SW_{in} (W m^{-2})	136.9	0.0	1239.2	237.5
α	0.60	0.09	0.93	0.33
LW_{in} (W m^{-2})	252.9	110.5	376.6	55.1
LW_{out} (W m^{-2})	294.3	181.6	345.6	27.9
Snow depth (m)	0.32	0.00	1.99	0.43

by digging a snow pit and taking snow samples at different depths. Averaged values of the observations at M1 over the period from October 1995 to May 2007 are given in table 2.3. More information on the instruments can be found in Oerlemans and Knap (1998) and Oerlemans (2000a). In addition, images of the instruments and the field location can be found on the project website: http://www.phys.uu.nl/~oerlemns/site_Mort/morteratsch.html

2.3 Model input

In order to obtain input values for the model, the measurements at Corvatsch and Samedan are combined and projected onto the grid. Regarding the precipitation estimates, daily mean values at Pontresina and Bernina-Curtinatsch are combined with half-hourly observations at Samedan.

Section 2.3.1 discusses the use of a Digital Elevation Model (DEM) to determine the surface topography and related quantities and to specify the model grid. In section 2.3.2, a description is given of how outliers in the measured data around the glacier are removed and how missing values are estimated by inter- and extrapolation. Finally, section 2.3.3 summarizes how measured climate variables are interpolated with height and used to derive the necessary model input on the grid.

2.3.1 Surface topography & grid

Calculations in the model are carried out on a regular grid with an equal grid spacing in the east-west and north-south direction. All the processes that affect the energy and mass balance are evaluated on the grid after every modeled time-step. Additionally, the snow model calculates subsurface properties in up to 11 vertical layers with varying depths, as explained in section 3.2.

The height profile of the glacier and the surrounding terrain is derived from a Digital Elevation Model (DEM) provided by the Bundesamt für Landestö-

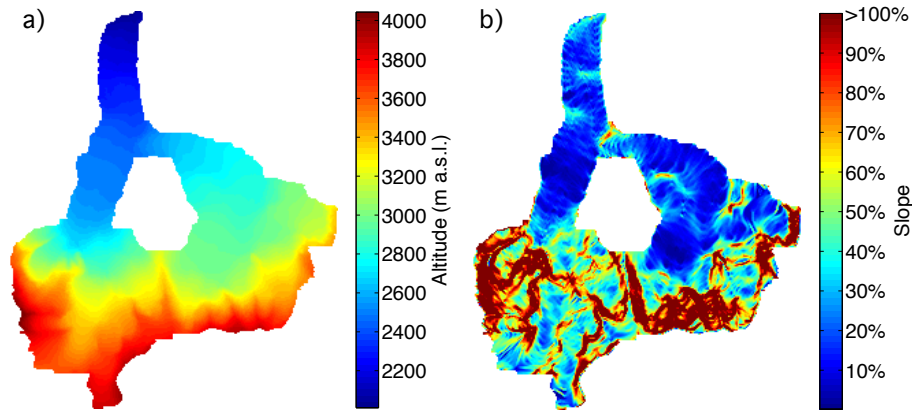


Fig. 2.5: Height profile (a) and the absolute slope (b) of the glacier. Heights are indicated in meters above sea level (m a.s.l.) and the absolute slope is given as a percentage ($100\% \equiv 45^\circ$).

pographie of Switzerland. The DEM not only provides altitudinal grid points, it also enables calculation of the slope and aspect of the grid cells. A 2D-height profile of the ice grid and the slope is given in figure 2.5. The DEM contains a total of 167241 grid points covering an area of 105 km^2 . Grid points covered by ice have been selected manually, resulting in a total of 29240 ice grid cells. It should be noted that not all the selected ice grid cells are actually covered by ice, especially in the accumulation zone. However, snow falling on these grid cells is most likely transported to nearby ice-covered grid cells by wind-driven snow drift or avalanches. It is therefore a reasonable assumption to treat these ice-free cells as part of the glacier. The resolution of the model grid equals the DEM resolution, so no resampling of the input data is needed.

The model computes the surface energy balance (equation (3.2)) and mass balance (equation (3.1)) only at the grid cells covered by the glacier. Elevation data of grid points on the glacier are used to derive height-dependent input parameters, as described in section 2.3.3. The elevation data of terrain surrounding the glacier are used in the calculation of the terrain parameters and shading (section 3.2.2).

All the grid cells are treated independently in the model with the only exception being the interaction between cells occurring in the calculation of the amount of solar radiation that is reflected by the surrounding terrain before reaching the grid cell. In the model, water that has run off from a grid cell is not added to the water content of the neighboring cells. Melt water tracks at the surface are mainly determined by the surface slope, which may vary strongly over short distances (figure 2.5(b)). With the time-independent surface topography and the DEM resolution of 25 meters we were not able to detect small-scale temporal and spatial variations in the surface slope. The presence of crevasses (due to stretching of the ice) plays an important role in the transport of melt water into the glacier. However, simulating this transport requires a very detailed surface profile and is beyond the scope of this study.

2.3.2 Data treatment

In general, the relative amount of data from stations around the glacier that is incorrect or missing is very small. No gaps larger than a few days are contained in the data sets of the relative humidity, precipitation, air temperature and incoming shortwave radiation. The pressure observations at Corvatsch and Samedan are in some cases absent for a longer period (up to 90 days). In most cases, the irregularities in the measurements could be solved using standard techniques, like interpolation between recent correct values. The method used to derive values for missing or incorrect data is dependent on the amount of successively missing data. Small gaps in the data sets are filled by linear interpolation between correct values. Generally, if measurements are absent at either Corvatsch or Samedan for more than one day, then data from the other station are used in combination with the height gradient of the measured variable of the previous day. If measurements are missing at both stations, then previous day values are used. The strategy described above is used to correct measurements of air temperature and relative humidity. Gaps in the air pressure measurements are always filled by linear interpolation, even in case of a long period of missing data. Precipitation data at Samedan are interpolated when less than a day of measurements is missing. In case of a larger interruption, previous day values are taken. Finally, shortwave radiation data are also interpolated for gaps smaller than a few hours. However, in order to preserve the daily pattern, large gaps are filled by means of theoretically derived values for the insolation and the atmospheric transmissivity.

2.3.3 Input values on the grid

Some of the input variables for the model are directly measured at the synoptic stations around the glacier. In that case, only altitudinal corrections have to be applied to the measured values. However, a different approach has to be used when the desired model input variables are not measured directly (e.g. cloud cover). These input variables need to be estimated using the available data.

Air temperature & relative humidity

The atmospheric temperature T_{atm} plays an important role in the calculation of the energy budget. First of all, the incoming longwave radiation is strongly dependent on the temperature of the sky (equation (3.20)). Furthermore, the turbulent fluxes (equation (3.26) and (3.27)) and the heat supplied by rain water (equation (3.29)) are also depending on the atmospheric temperature. Relative humidity estimates are used in the computation of the turbulent fluxes and the incoming longwave radiation by means of the vapor pressure. Estimates of the potential temperature are needed to compute the potential temperature lapse rate (γ_L), which is used in the calculation of the katabatic exchange coefficient (equation (3.28)). The air temperature (T_{atm}), relative humidity (RH) and potential temperature (θ) are assumed to be linearly dependent on altitude. Hence, the grid values of these parameters are determined by interpolating the measured values at Corvatsch and Samedan linearly with height.

Air pressure & density

Grid values of the air pressure are required to calculate the transmission coefficient for Rayleigh scattering τ_R and gas absorption τ_g (equation (3.8)). The air pressure p_{air} on the grid can be computed using the following relation:

$$p_{air} = p_{ref} \left(\frac{\theta}{T_{atm}} \right)^{\frac{R_d}{c_p}}, \quad (2.1)$$

where p_{ref} is a reference pressure, R_d is the gas constant for dry air and c_p is the specific heat of dry air (table 3.2). The air pressure is calculated using interpolated values of the air temperature (T_{atm}) and the potential temperature (θ).

The air density ρ_{air} is needed in the calculation of the turbulent fluxes in equation (3.26) and (3.27). On the grid, ρ_{air} can be determined using the ideal gas law:

$$\rho_{air} = \frac{p_{air}}{R_d T_{atm}}. \quad (2.2)$$

Atmospheric vapor pressure

Values of the atmospheric vapor pressure e_a are required to determine the latent heat flux (equation (3.27)) and the incoming longwave radiation (equation (3.22)). e_a can be described as a function of the air pressure and specific humidity (q), assuming that $q \ll 1$. In addition, the specific humidity is dependent on the specific humidity of saturated air q_s which is in turn a function of the saturation vapor pressure e_{surf} :

$$e_a = \frac{q p_{air}}{\epsilon_R} \quad (2.3)$$

$$q = \frac{RH}{100\%} q_s \quad (2.4)$$

$$q_s = \frac{e_{surf} \epsilon_R}{p_{air}} \quad (2.5)$$

$$e_{surf} = p_0 \exp \left[\frac{L_{s,v}}{R_v} \left(\frac{1}{273.15} - \frac{1}{T_{atm}} \right) \right], \quad (2.6)$$

where R_v is the gas constant for water vapor, ϵ_R is the ratio of R_d and R_v , p_0 denotes the saturation vapor pressure at 273.15 K and $L_{s,v}$ is the latent heat of sublimation or vaporization (table 3.2). Equation (2.6) relates the saturation vapor pressure to the air temperature and is known as the Clausius Clapeyron equation.

Cloud cover

The cloud cover has a significant impact on the shortwave and longwave components of the energy budget. However, no direct measurements of the cloud fraction are available. Therefore, measurements of the insolation at Corvatsch were compared to the theoretical clear-sky radiation (equation (3.4) with $\tau_{cl} = 1$) in order to calculate the cloud transmissivity (Klok and Oerlemans, 2002). The cloud fraction is then computed using a relation suggested by Greuell *et al.* (1997) (equation (3.14)). Interpolation of the cloud cover is necessary during

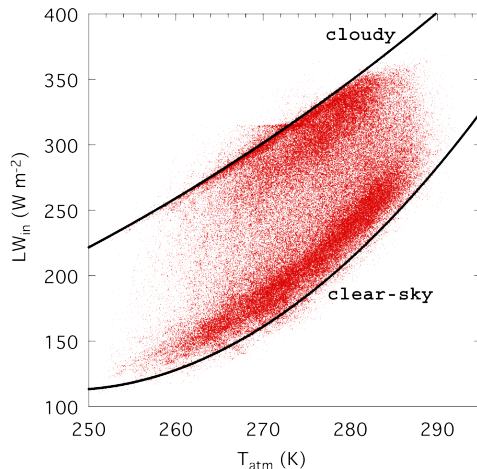


Fig. 2.6: Incoming longwave radiation (LW_{in}) at M1 as a function of the atmospheric temperature. The black lines represent the two boundaries (0 and 100 % cloudiness) between which the cloud fraction is linearly interpolated

the nights, since the absence of sun light hinders the determination of the cloud transmissivity using the method described above. Another problem is that the cloud cover estimate is prone to a large uncertainty when the measured incoming shortwave flux at Corvatsch is small. To account for this, the cloud fraction during the nights is interpolated between the value one hour before sunset and one hour after sunrise. However, especially in winter, daily fluctuations in the cloud cover are rarely represented in the calculated cloud cover. Therefore, we have chosen to compute a 24-hour running mean value, which is used as input for the model.

Additionally, the cloud fraction is also estimated using measurements from the AWS at M1. This is done by assuming that the incoming long wave radiation at a certain atmospheric temperature is linearly dependent on the cloud cover (Van den Broeke *et al.*, 2004, 2006; Kuipers Munneke *et al.*, 2008). Relatively high values of the measured incoming longwave radiation are associated with a large cloud cover, while low values are associated with clear-sky conditions. In order to scale the cloud fraction, two boundaries need to be specified between which the cloud cover is interpolated. The upper boundary will represent overcast conditions and the lower boundary is associated with clear-sky conditions, as shown in figure 2.6. The black line representing cloudy conditions is determined theoretically, using the Stefan-Boltzmann law (equation (3.20)), and thus assuming that the sky emissivity ϵ is equal to 1. In order to determine the lower black line, the incoming longwave radiation is binned in 1 degree K bins before fitting a polynomial least-square fitting curve through the lowest 5% of the data. Finally, the cloud fraction is computed by linear interpolation between the two black lines. The cloud cover estimates from the measurements at Corvatsch are used as input for the model, because the cloud fraction can be determined for the whole simulation period since 1983. Cloud cover estimates, derived from measurements at station M1, are more reliable (also values during nighttime), but they do not cover the entire simulation period. Therefore, these

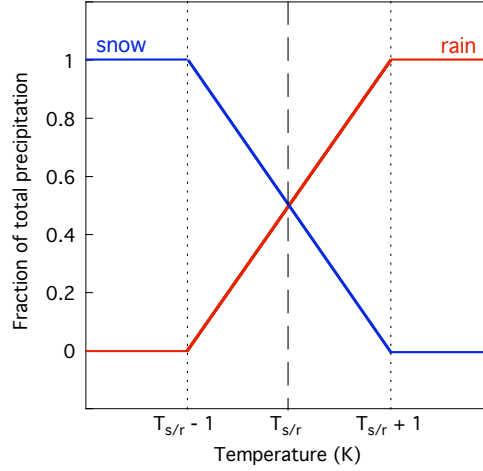


Fig. 2.7: Snow to rain transition as a function of air temperature showing the snow fraction (blue) and the rain fraction (red)

estimates are only used for comparison purposes.

Precipitation

The model distinguishes between two types of precipitation: snow fall and rain fall. The amount of precipitation is derived from daily measurements at Pontresina and Bernina-Curtinatsch in combination with half-hourly values from Samedan to capture diurnal variations. In mountainous areas, the precipitation is generally not constant with height, therefore, a precipitation gradient γ_p is introduced. With this gradient and the mean precipitation between Pontresina and Bernina-Curtinatsch, the precipitation can be calculated for the entire grid. Nevertheless, the measurements contain no information on the type of precipitation. It is clear that the precipitation type is related to the air temperature. Therefore, a threshold air temperature $T_{s/r}$ is introduced as the temperature above which rain fall is most likely and below which snow fall occurs most of the time. Typically, $T_{s/r}$ ranges between 1 °C and 2 °C. Clearly, the transition from snow to rain does not always occur at the same temperature. To account for this in the model, we assume that between $T_{s/r} - 1$ °C and $T_{s/r} + 1$ °C, the snow fraction decreases gradually, while the rain fraction increases, as depicted in figure 2.7. Below $T_{s/r} - 1$ °C precipitation is always snow, above $T_{s/r} + 1$ °C all precipitation is rain. The amount of rain fall and snow fall (in meters water or snow) between $T_{s/r} - 1$ °C and $T_{s/r} + 1$ °C is calculated using the following expressions:

$$rain = P \left[\frac{T_{atm} - T_{s/r} + 1}{2} \right] \quad (2.7)$$

$$snow = P \left[\frac{T_{s/r} - T_{atm} + 1}{2} \right] \frac{\rho_w}{\rho_{frsnow}}, \quad (2.8)$$

where P is the amount of precipitation (m w.e.), ρ_{frsnow} is the density of fresh snow and ρ_w is the density of water. Variations in the snow accumulation have

a direct impact on the mass balance. However, estimates of the precipitation on the grid are quite inaccurate, partly due to uncertainties in the precipitation gradient. Because of the indefinite nature of γ_p , this parameter has been used to tune the height dependence of the mass balance in order to achieve a good agreement between model results and measurements as described in section 3.2.3.

Wind properties

Wind speed and wind direction are additionally observed quantities at measurement site M1. However, wind properties are not needed as input for the model, since all the energy fluxes are formulated in such a way that they do not depend on the wind speed and direction. Formulations of the turbulent fluxes are often based on the Monin-Obukhov similarity theory, in which the fluxes are assumed to be related to the mean gradients of the wind speed, potential temperature and specific humidity. However, simulation of the wind speed in mountainous regions is complicated, due to the strongly variable nature of the wind properties. Oerlemans and Grisogono (2002) managed to develop parameterizations independent of the vertical wind profile (see equations (3.26) and (3.27)), which enabled us to calculate the turbulent fluxes with air temperature and relative humidity measurements at the stations around the glacier.

Chapter 3

Model description

The main goal of this study is to simulate the spatial distribution and the temporal evolution of the mass balance of the Morteratsch glacier for the period from 1983 to 2008, taking into account processes acting below the glacier surface. In order to achieve this, a two dimensional model has been developed along the lines presented by Klok and Oerlemans (2002), which evaluates the evolution of the energy balance at every ice-covered grid point. The surface energy balance is the sum of all the fluxes that add energy to or remove energy from the surface layer. If all the incoming and outgoing energy fluxes are known then the amount of energy involved in melting can be computed from the energy budget.

This energy balance model is coupled to a snow model, which simulates vertical profiles of temperature, density and melt water within the snow pack and the underlying ten meters of ice. The implementation of a snow model is new for this glacier and it enables us to determine the heat flux between the surface and the underlying ice more accurately. Additionally, the mass and energy contribution by refreezing of meltwater can be estimated with the snow model. It will be shown that refreezing of meltwater will have a significant effect on both the subsurface temperature and density profiles. Measurements of meteorological variables at four locations around the glacier are used as input for the model, as described in chapter 2. Moreover, the data measured on the glacier are used to test and fine tune the model results.

In the next section, a theoretical description of the energy balance model (section 3.1.1) and the snow model (section 3.1.2) is given. In section 3.2, the numerical properties of the model are discussed, and section 3.3 summarizes which experiments are performed with the model.

3.1 Theoretical description

The specific mass balance MB at a certain location on the glacier is defined as the accumulated exchange of mass per unit area over a period of time, often expressed in meters water equivalent per square meter (m w.e. m^{-2}). It is the sum of accumulation and ablation. In this model, MB is determined by the amount of melt, snow fall, refreezing of melt and rain water, sublimation,

riming and exchange of vapor through the surface:

$$MB = \int \left[P + V + \frac{Q_{LH}}{L_s} - R \right] dt, \quad (3.1)$$

R denotes the amount of runoff, P is the amount of precipitation, V is the mass exchange due to vapor transport through the surface, Q_{LH} is the latent heat flux and L_s is the latent heat of sublimation (table 3.2). Other contributing processes, such as wind driven snow drift or avalanches, may have a significant influence on the mass balance, but simulating the associated mass transport is complicated and not included in the model. The runoff term R takes into account both the effects of melting and refreezing of water below the surface. Meltwater generated at the surface may refreeze in the snow pack, and may therefore be exposed to melting again at a later time. In traditional mass balance formulations (Klok and Oerlemans, 2002) water that was subtracted from the surface mass balance at a certain time, should be added again to the mass budget at a later time when the refrozen water is melted again. 3.1 addresses this problem by subtracting only excess melt/rain water and slush water that leaves the firn layer (R) from the mass balance. The precipitation term P includes both snow fall *and* rain fall in order to maintain mass continuity, since (excess) rain water is also influencing the runoff term R . Percolating rain water can be stored and frozen in the snow pack and thus contribute to the total accumulation.

The latent heat flux Q_{LH} adds or removes a (small) layer of mass at the surface, while the vapor flux V transports mass through the surface, causing the subsurface density profile to change, thereby affecting the mass balance. Energy fluxes directed towards the surface are defined positive, while fluxes directed away from the surface are negative. The phase change from water vapor to solid ice particles is called riming and this process is associated with a positive latent heat flux and consequently a positive contribution to the mass budget. A negative latent heat flux is associated with a phase change from ice to water vapor and is called sublimation. The effects of R , V , Q_{LH} and P on the surface mass balance are evaluated after every time step and integrated over time to compute the specific mass balance since the start of the simulation at a specific location on the glacier. In figure 3.1(a) an overview of the fluxes that determine the mass budget, is given.

Mass balance data are usually derived from stake measurements on the glacier. These stakes measure the relative surface height, which is determined by the amount of ice melt during the ablation season, and snow accumulation and packing of the snow during the accumulation season. Hence, the relative surface height is affected by all the processes that change the thickness of the glacier. On the other hand, the mass balance only includes processes that exchange mass between the glacier and the atmosphere or the surrounding terrain (runoff) and is therefore a direct measure of the total mass (not the thickness) in a column of ice.

3.1.1 Energy balance model

The surface energy balance includes all the energy fluxes acting on the surface and is used to compute the energy involved in melting (Q_M) and sublimation/riming (Q_{LH}) in equation (3.1). To justify the use of the energy balance

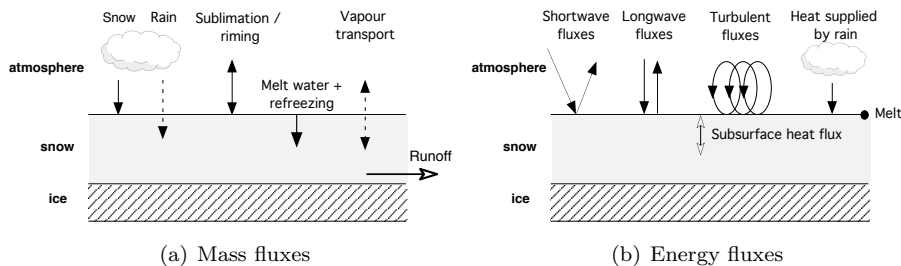


Fig. 3.1: Graphical representation of the fluxes that play a role in the determination of the mass budget (a) and the energy budget (b) at the glacier surface.

for this purpose, we have to be sure that all the relevant incoming and outgoing energy fluxes are considered in the model. The surface energy budget is given by

$$Q_M = SW_{in} + SW_{out} + LW_{in} + LW_{out} + Q_{LH} + Q_{SH} + Q_G + Q_R, \quad (3.2)$$

where SW_{in} and SW_{out} are the incoming and reflected solar radiation, LW_{in} and LW_{out} are the incoming and outgoing longwave radiation, Q_{SH} is the sensible heat flux, Q_G is the subsurface heat flux and Q_R is the heat supplied by rain. The effect of the penetration of shortwave radiation in the upper snow layers has been neglected. LW_{out} , Q_{LH} , Q_{SH} , Q_G and Q_M are dependent on the surface temperature. Since the surface temperature is the only unknown in equation (3.2), this equation can be solved by finding the surface temperature for which the right-hand side (r.h.s.) of equation (3.2) is equal to zero. This procedure is described in section 3.2.2. The surface temperature is limited at 0°C , so Q_M can attain a positive (nonzero) value in order to satisfy equation (3.2). Q_M will be zero when the surface temperature is below freezing point. Note that the heat released by refreezing of meltwater is not considered in equation (3.2), because it does not influence the surface energy balance (and thus the mass balance) directly. However, refreezing does affect the subsurface heat flux Q_G due to increasing subsurface temperatures and densities and therefore it does have an indirect effect on the surface energy balance and thus the mass balance. The increased firn density after refreezing is also affecting the mass balance, since it takes more energy to melt the same ice several times, while the mass loss is only considered once in the mass budget, as described before. The formulations used for the fluxes that contribute to the energy budget are described in the remaining part of this section. In figure 3.1(b) an overview of the fluxes that determine the energy budget, is given.

Incoming shortwave radiation

The incoming solar radiation is an important source of energy at the surface. Calculating this flux is quite complicated, since the amount of incoming shortwave radiation impinging on a grid cell is determined by several factors:

1. Top of atmosphere radiation
2. State of the atmosphere (e.g. cloud fraction, water vapor concentration, aerosol concentration)

3. Topographic shading
4. Angle of incidence (orientation of the grid cell)
5. Visibility and reflectivity of the surrounding terrain
6. Visibility and diffusivity of the sky

If topographic effects (3, 4 and 5) are neglected, then the incident radiation at the surface is given by (Oerlemans and Knap (1998))

$$I = I_0 \cos(\theta_z) \tau_R \tau_g \tau_w \tau_{as} \tau_{cl}, \quad (3.3)$$

where I_0 is the incoming radiation at the top of the atmosphere on a surface normal to the incident solar radiation, θ_z is the solar zenith angle, τ_R , τ_g , τ_w , τ_{as} and τ_{cl} are the transmission coefficients for Rayleigh scattering, gas absorption, water vapor absorption, and scattering and absorption by aerosols and clouds, respectively.

The top-of-the-atmosphere radiation is dependent on the distance between the Earth and the Sun, which is varying throughout the year. The following relation is used to compute I_0 (Meyers and Dale, 1983):

$$I_0 = 1353[1 + 0.034 \cos(2\pi(d - 1)/365)], \quad (3.4)$$

where d is the day number.

For surfaces without a slope the angle of incidence θ of the solar radiation is equal to the solar zenith angle θ_z . In this case the cosine of the incidence angle is given by

$$\cos \theta_z = \sin \phi \sin \delta + \cos \phi \cos \delta \cos \omega, \quad (3.5)$$

where ϕ is the latitude, δ denotes the solar declination, and ω is the hour angle. Figures 3.2(a) and 3.2(b) show the daily mean extraterrestrial irradiance impinging on a horizontal surface and the average irradiance during the day, respectively. For arbitrarily oriented surfaces the relation for the angle of incidence is different and can be written in the following form (Iqbal, 1983):

$$\cos \theta = \cos s \cos \theta_z + \sin s \cos(\psi - \gamma), \quad (3.6)$$

where s is the slope, ψ is the solar azimuth angle and γ is the surface azimuth angle. Figure 3.3 shows the position of the sun relative to an inclined plane and the related angles θ , s , ψ and γ . The solar azimuth angle ψ is used in the computation of the terrain parameters (see section 3.2.2) and can be expressed as a function of the solar declination (δ), the hour angle (ω) and the solar zenith angle (θ_z) as follows:

$$\psi = \arcsin \left(\frac{-\cos \delta \sin \omega}{\sin \theta_z} \right). \quad (3.7)$$

The transmission coefficients for Rayleigh scattering and gas absorption, τ_R and τ_g , are both a function of the air pressure and optical air mass. The product of τ_R and τ_g is determined using the following empirical relationship (Kondratyev, 1969; Atwater and Brown Jr, 1974):

$$\tau_R \tau_g = 1.021 - 0.084 \sqrt{m(949p_{air} \times 10^{-5} + 0.051)}, \quad (3.8)$$

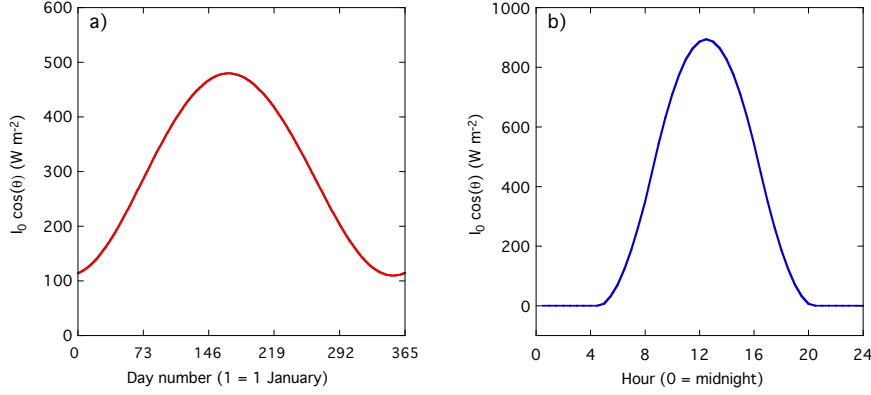


Fig. 3.2: Daily mean extraterrestrial irradiance on a horizontal surface (a), and extraterrestrial irradiance during the day averaged over a year (b) as described by equation (3.3) at a latitude of $46^{\circ}24'N$.

with m the optical air mass and p_{air} the air pressure in kPa. m is calculated empirically after Meyers and Dale (1983) and is formulated as

$$m = 35 \frac{p_{air}}{p_{sea}} (1224 \cos^2 \theta_z + 1)^{-\frac{1}{2}}, \quad (3.9)$$

where p_{sea} is the air pressure at sea level (kPa) (table 3.1).

The transmission coefficient for water vapor absorption, τ_w , is dependent on the optical thickness and the amount of water in the atmosphere. τ_w is computed using an expression by McDonald (1960):

$$\tau_w = 1 - 0.077(um)^{0.3}, \quad (3.10)$$

where u is the amount of precipitable water (cm). This term u can be expressed as a function of the daily average dew point temperature T_{dew} ($^{\circ}F$) as follows (Smith, 1966):

$$u = \exp[0.1133 - \log(\lambda + 1) + 0.0393T_{dew}], \quad (3.11)$$

where λ is a constant, empirically derived for latitude and season, assuming a dependence of the precipitable water on the daily average dew point temperature. An annual mean value for λ for the corresponding latitude was taken from Smith (1966) (table 3.1).

The transmission coefficient for aerosol attenuation, τ_{as} , was computed using the following relation by Houghton (1954):

$$\tau_{as} = h^m, \quad (3.12)$$

where h is an empirical constant, which can be derived by fitting the modeled incoming solar radiation under clear-sky conditions ($\tau_{cl}=1$) to measurements. Klok and Oerlemans (2002) derived values of h for Corvatsch and Samedan for clear-sky days in the summer of 1999. They found a value for h of 0.96 for

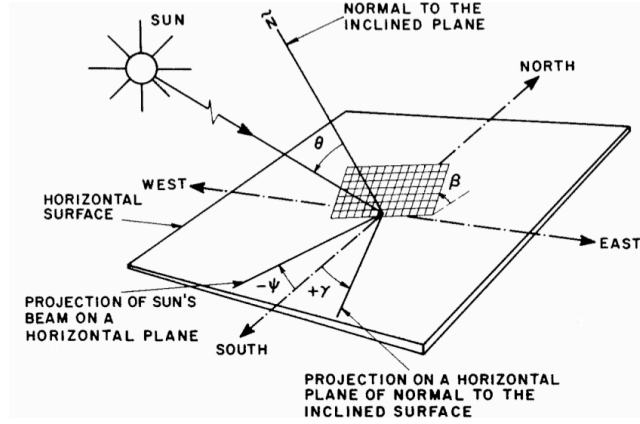


Fig. 3.3: The sun's position relative to an inclined plane and the related angles s (β in the figure), θ , ψ and γ [source: Iqbal (1983)].

Corvatsch and 0.92 for Samedan. These values were linearly interpolated with height in our model to find values for h on the grid.

The cloud transmissivity, τ_{cl} , is calculated by taking the ratio of the measured incoming shortwave radiation to the computed clear-sky radiation ($\tau_{cl}=1$) for Corvatsch (Klok and Oerlemans, 2002).

The total incoming shortwave radiation on the grid can be divided into a part which is coming directly from the sun (I_{dir}), a part which is scattered in the atmosphere before reaching the surface (I_{sky}) and a part which is reflected by the surrounding terrain before reaching the grid cell (I_{refl}). The direct part of the shortwave radiation I_{dir} can be formulated as a function of the cloud cover, following Oerlemans (1992):

$$I_{dir} = I (0.2 + 0.65(1 - n)), \quad (3.13)$$

where n is the fractional cloud cover. We adopted the following relation, suggested by Greuell *et al.* (1997), to calculate the cloud cover as a function of the transmission coefficient for clouds (τ_{cl}):

$$n = -0.281 + 1.20\sqrt{0.0543 + 1.66(1 - \tau_{cl})}. \quad (3.14)$$

Values of τ_{cl} smaller than 0.352 are set to 0.352 in order to prevent the cloud fraction from obtaining values larger than 1. During the nights, n cannot be derived from measurements, because τ_{cl} is unknown in the absence of sun light. Therefore, n is interpolated linearly between sunset and sunrise, before applying the 24-hour running mean, which leads to a rather large uncertainty in the cloud cover estimates.

It becomes important to distinguish between direct and diffuse radiation when topographic effects are considered. When a grid cell is shaded by the surrounding terrain, then the direct component of the shortwave radiation is equal to zero, and consequently the grid cell only receives shortwave radiation coming from the sky and the surrounding terrain. The numerical method applied to determine which grid cells are shaded at a certain time is described in section 3.2.2. Furthermore, the angle of incidence correction (equation (3.6)) is only

applied to the direct part of the solar radiation, since diffuse radiation is coming from all directions where the sky is visible. The amount of diffuse radiation coming from the sky I_{sky} depends on the fraction of the overlying hemisphere which is visible to a grid point, the so-called sky view factor V_{sky} (Dozier and Frew, 1989):

$$I_{sky} = I (0.8 - 0.65(1 - n))V_{sky}. \quad (3.15)$$

The remainder of the overlying hemisphere ($1 - V_{sky}$) is captured in the terrain view factor V_{ter} . This terrain view factor is needed to calculate the amount of solar radiation that is reflected by the surrounding terrain before reaching the grid cell (I_{refl}). The expression used in the model to compute this part of the incoming shortwave radiation is (Klok and Oerlemans, 2002)

$$I_{refl} = V_{ter}[f_{ice}\alpha_{ice} + (1 - f_{ice})\alpha_{ter}]I_{mean}, \quad (3.16)$$

where f_{ice} is the fraction of the visible surrounding terrain covered by ice, α_{ice} is the mean albedo of the glacier, α_{ter} is the albedo of the surrounding terrain, and I_{mean} is the amount of incoming shortwave radiation averaged over the whole glacier after correcting for the incidence angle and shading. If snow is present at the tongue, $\alpha_{ter}=0.5$, if not, $\alpha_{ter}=0.1$. The numerical procedure used to determine the terrain parameters f_{ice} , V_{sky} and V_{ter} is described in section 3.2.2.

The total incoming solar radiation SW_{in} impinging on a grid cell is the sum of the direct radiation, diffuse radiation from the sky and radiation reflected towards the grid cell by the surrounding terrain:

$$SW_{in} = I_{dir} + I_{sky} + I_{refl}. \quad (3.17)$$

Reflected shortwave radiation

The net shortwave budget ($SW_{in} + SW_{out}$) is the major source of energy at the surface. Since it is linearly dependent on the albedo, it can be understood that small variations in the albedo can have a significant impact on the energy and mass balance. The fraction of the incoming shortwave radiation that is reflected at the surface is computed using a parameterization described by Oerlemans and Knap (1998). In this parameterization the albedo of a grid cell at a certain time is a function of the snow depth and the time since the last snow fall event:

$$\alpha(t) = \alpha_{snow}(t) + (\alpha_{ice} - \alpha_{snow}(t)) \exp\left(\frac{-d}{d^*}\right) \quad (3.18)$$

$$\alpha_{snow}(t) = \alpha_{firn} + (\alpha_{frsnow} - \alpha_{firn}) \exp\left(\frac{s-t}{t^*}\right), \quad (3.19)$$

where $\alpha(t)$ is the glacier albedo, $\alpha_{snow}(t)$ is the albedo of snow, α_{ice} is the albedo of ice, α_{firn} is the albedo of firn, α_{frsnow} is the albedo of fresh snow, d is the snow depth (mm w.e.), d^* is characteristic snow depth scale (mm w.e.), s is the time of the last snow fall event (days), t is the actual time (days), and t^* is a characteristic time scale (days).

The albedo can also be expressed as a function of the snow depth and the accumulated maximum temperatures since the last snow fall event (Brock *et al.*, 2000; Winther, 1993). Klok and Oerlemans (2004) concluded that the difference

in mass balance sensitivity between these two methods is negligible. Satellite observations show a significant decrease of the albedo of ice due to the presence of debris (Klok *et al.*, 2003). However, capturing these variations in an expression for the ice albedo is complicated, since the amount of debris, and thus the ice albedo, is not clearly a function of e.g. elevation. Furthermore, large amounts of debris can have an insulating effect, which will also have a significant influence on the energy balance. We assumed the ice albedo prior to the year 2002 to be 0.32, based on measurements of the shortwave fluxes at M1. These measurements reveal a significant drop of the ice albedo for the period from 2002 to 2008, possibly due to an increasing amount of debris deposition (Oerlemans *et al.*, 2009). We simulate the effect of a decreasing ice albedo on the mass balance by manually adjusting the ice albedo during the simulation for the years 2002-2008. The sensitivity of the mass balance to this adjustment is investigated and the results are given in section 4.4.

Incoming longwave radiation

The net longwave budget ($LW_{in} + LW_{out}$) is on average the major sink of energy at the surface. Nevertheless, on very warm and cloudy days, the longwave budget can become positive. The amount of thermal radiation coming from the sky is strongly dependent on the atmospheric temperature and the cloud cover. The following relation is adopted to calculate the incoming longwave radiation:

$$LW_{in} = \epsilon \sigma T_{atm}^4, \quad (3.20)$$

where ϵ is the emissivity of the sky, σ is the Stefan-Boltzman constant and T_{atm} is the atmospheric temperature. For ϵ , we use a parameterization found by Konzelmann *et al.* (1994), which expresses ϵ as a function of the fractional cloud cover. In this parameterization, it is assumed that the contributions of the cloudy and cloudless fraction of the sky can be separated (Kimball *et al.*, 1982; Oerlemans and Hoogendoorn, 1989). The total emissivity of the sky is then given by

$$\epsilon = \epsilon_{cs}(1 - n^c) + \epsilon_{cl}n^c, \quad (3.21)$$

where ϵ_{cs} is the clear-sky emissivity, c is an empirical constant, ϵ_{cl} is the cloud emissivity and n is the cloud cover as in equation (3.14). For the parameter c , we used a value which was determined by Greuell *et al.* (1997) and was based on measurements on the Pasterze, Austria (table 3.1). The clear-sky emissivity can be described as a function of the air temperature and the water vapor pressure as follows:

$$\epsilon_{cs} = 0.23 + b \left(\frac{e_a}{T_{atm}} \right)^{1/8}, \quad (3.22)$$

where e_a is the atmospheric water vapor pressure, which is determined using measurements of the air temperature, relative humidity and air pressure at Corvatsch and Samedan, as described in section 2.3.3. e_a becomes increasingly important for the longwave budget when the cloud cover is decreasing (first term on the r.h.s. of equation (3.21)). The parameters b and ϵ_{cl} have been determined by Klok and Oerlemans (2002) after fitting the measured incoming longwave radiation at M1 in 1999 to the computed radiation (table 3.1). These values are also used in this model.

The main uncertainty in the calculation of the longwave budget is associated with the cloud cover estimates, which are based on measurements of shortwave radiation at Corvatsch (see section 2.3.3). In the model, fluctuations in the cloud cover are smoothed by applying a 24-hour running mean and the cloud cover is assumed to be spatially invariant over the entire glacier. Therefore, the large fluctuations in the cloud cover, which are often seen in reality, are not always represented in the cloud cover estimates in the model.

The method described here to determine the incoming thermal radiation has some drawbacks. First of all, the contribution of longwave radiation coming from the surrounding terrain and the amount of longwave radiation coming from the sky that is blocked by the terrain, have been neglected. Furthermore, it would have been more physically appropriate if ϵ_{cl} was a function of the cloud height and cloud temperature, instead of using the fitting procedure to determine ϵ_{cl} and b .

Outgoing longwave radiation

The formulation used in the model to determine the outgoing longwave radiation is (assuming that the ice surface acts as a blackbody):

$$LW_{out} = \sigma T_{surf}^4, \quad (3.23)$$

where T_{surf} denotes the surface temperature and σ is the Stefan-Boltzmann constant (table 3.2). Therefore, the thermal radiation emitted by the surface is only a function of the surface temperature, which is determined internally in the model.

Turbulent fluxes

After Reynolds decomposition and averaging of the Navier-Stokes equations, the sensible and latent heat flux can be written as a function of the averaged product of perturbations in the vertical wind speed (w'), potential temperature (θ') and specific humidity (q') as follows:

$$Q_{SH} = \rho_{air} c_p \overline{w'\theta'} \quad (3.24)$$

$$Q_{LH} = \rho_{air} L_{s,v} \overline{w'q'}. \quad (3.25)$$

Measuring the mean product of deviations of the wind, temperature and humidity is complicated, therefore, several methods have been developed which usually require knowledge of the surface roughness, humidity and wind speed at two levels (e.g. Dyer, 1974; Holtslag and De Bruin, 1988). For the Morteratsch glacier, a detailed pattern of the wind is hard to estimate, due to its variable nature. Therefore, formulations are used, which express the turbulent fluxes as a function of the vertical temperature and humidity gradient above the surface. The nature of the surface determines to a large extent the amplitude of these gradients. A big problem in this kind of studies is to relate measurements of climate variables, like temperature and humidity, around the glacier to the microclimate on the glacier.

In summer, the temperature gradients between the surface and the air can become large, because the surface temperature is limited at 0 °C. At 0 °C, the ice is at melting point and in that case excess energy will be used for melting

instead of raising the temperature of the medium. As a consequence of a strong positive temperature gradient, a glacier wind may form. A glacier wind is often present in summer, due to cooling of the air above the sloping surface, and may form a circulation with the valley (or large-scale) wind above the glacier boundary layer. In case of a large temperature deficit, the turbulent exchange of heat (sensible heat flux) to the surface can be quite substantial, depending on the wind speed.

The turbulent exchange of moisture (latent heat flux) is dependent on the humidity gradient. If the vapor pressure of the air is larger than the vapor pressure at the surface, then condensation ($T_{surf} = 0 \text{ }^\circ\text{C}$) or riming ($T_{surf} < 0 \text{ }^\circ\text{C}$) of water vapor will heat the surface. In case of a higher vapor pressure at the surface, evaporation or sublimation will result in surface cooling.

The expressions used for the sensible heat flux Q_{SH} and the latent heat flux Q_{LH} are (Oerlemans and Grisogono, 2002):

$$Q_{SH} = \rho_{air} c_p \frac{C_{kat} + C_b}{2} (T_{atm} - T_{surf}) \quad (3.26)$$

$$Q_{LH} = \begin{cases} 0.622 \rho_{air} L_v \frac{C_{kat} + C_b}{2} \frac{e_a - e_{surf}}{p_{air}} & \text{if } T_{surf} = 0 \text{ }^\circ\text{C} \\ 0.622 \rho_{air} L_s \frac{C_{kat} + C_b}{2} \frac{e_a - e_{surf}}{p_{air}} & \text{if } T_{surf} < 0 \text{ }^\circ\text{C} \end{cases}, \quad (3.27)$$

where C_{kat} is the katabatic exchange coefficient, C_b is the background turbulent exchange coefficient (table 3.1), e_{surf} is the saturation vapor pressure at the surface (section 2.3.3), and L_v and L_s are the latent heat of evaporation and sublimation respectively (table 3.2). The katabatic bulk exchange coefficient is given by

$$C_{kat} = k(T_{atm} - T_{surf}) \sqrt{\frac{g}{T_0 \gamma_L Pr}}, \quad (3.28)$$

with k an empirical constant, g the gravitational acceleration, γ_L the potential temperature lapse rate, and Pr the Prandtl number.

The three equations ((3.26)-(3.28)) were obtained from an improved version of the Prandtl model, where the height of the wind maximum is depending on the temperature deficit at the glacier surface. Oerlemans and Grisogono (2002) developed these parameterizations for a katabatic flow over small glaciers. The wind field over these small glaciers is difficult to simulate properly by models, so the turbulent fluxes are expressed as a function of air temperature and humidity, which have a more robust mesoscale structure. With the above described method, the turbulent fluxes can be determined using measurements of meteorological variables from nearby stations. The values for Pr and k are taken from Oerlemans and Grisogono (2002) (table 3.1).

C_{kat} is associated with turbulence generated by the katabatic wind. Note that C_{kat} can only be computed if the potential temperature lapse rate γ_L has a positive value (stable boundary layer). Therefore, γ_L is not allowed to become smaller than 0.0015 K m^{-1} . C_b is associated with turbulence generated by the large-scale wind or the valley wind. It is not clear how large the contribution of this turbulence is, therefore, this parameter has been used, together with other parameters, to calibrate the model results in such a way that measured and modeled melt are in agreement.

Heat supplied by rain

In the model, rainfall occurs at air temperatures above melting point. The temperature of the rain drops is assumed to be similar to the atmospheric temperature. Consequently, rainfall will always add heat to the surface energy budget. During a heavy rainfall event in summer, this can add more than 100 W m^{-2} to the surface layer. However, on average over the year, the contribution to the energy balance is only about 0.5 W m^{-2} . Although the influence is small, it is considered in the energy budget using the following formulation:

$$Q_R = c_w \dot{r} (T_{atm} - T_{surf}), \quad (3.29)$$

where c_w is the specific heat of water and \dot{r} is the rain rate (kg s^{-1}).

Subsurface heat flux

The heat flux from the surface into the glacier or from the glacier to the surface is called the subsurface heat flux. The energy flux between two layers Q_G is a function of the vertical temperature gradient and is given by

$$Q_G = \kappa(\rho) \frac{\partial T}{\partial z}, \quad (3.30)$$

where $\kappa(\rho)$ is the effective conductivity, ρ is the density of the layer and T is the temperature of the ice at a certain depth z , so Q_G is a function of ρ , T and z . In section 3.2.2, the numerical procedure used to calculate Q_G at the surface is explained in more detail. The effective conductivity describes the exchange of energy between layers due to convection, conduction, radiation and vapor diffusion, and is calculated using an expression by Sturm *et al.* (1997):

$$\kappa(\rho) = 0.138 - 1.01 \times 10^{-3} \rho + 3.233 \times 10^{-6} \rho^2, \quad (3.31)$$

where κ is expressed as a function of the firn density only. κ is in fact also dependent on the temperature of the medium. However, no adequate formulation of κ as a function of both density and temperature is available, therefore, κ is only a function of ρ in the model.

In order to compute the subsurface heat flux, vertical profiles of the temperature and density are required. These profiles are calculated on the grid after every time step, taking into account processes, like refreezing of melt and rain water and the gravitational densification of snow and firn. In the next section, a summary of the snow model used to calculate these vertical profiles is given. In addition, the coupling between the surface energy balance model and the snow model through the subsurface heat flux is described.

3.1.2 Multi-layer snow model

In this section, a theoretical description of the multi-layer snow model is given. In the end, the main goal is to assess how large the influence of processes acting up to several meters below the surface is on the energy and mass balance at the surface. Of special interest is the process of refreezing of melt and rain water. Refreezing has a marked influence on the mass and energy balance through its impact on the surface temperature and through the process of melting refrozen

Table 3.1: Model parameters

<i>Description</i>	<i>Symbol</i>	<i>Equations</i>	<i>Value</i>	<i>Units</i>
Threshold temperature	$T_{s/r}$	(2.7), (2.8)	tuning	
Density of fresh snow	ρ_{frsnow}	(2.8)	tuning	
Latitude	ϕ	(3.5)	46°24'N	
Sea level pressure	p_{sea}	(3.9)	1020	hPa
Empirical constant	λ	(3.11)	2.78	
Empirical constant	h	(3.12)	0.92-0.96	
Characteristic depth scale	d^*	(3.18)	11	mm w.e.
Albedo of ice	α_{ice}	(3.18)	tuning	
Albedo of firn	α_{firn}	(3.19)	0.53	
Albedo of fresh snow	α_{frsnow}	(3.19)	0.90	
Characteristic time scale	t^*	(3.19)	21.9	days
Empirical constant	c	(3.21)	2	
Empirical constant	b	(3.22)	0.433	
Cloud emissivity	ϵ_{cl}	(3.22)	0.984	
Background exch. coeff.	C_b	(3.26), (3.27)	tuning	
Empirical constant	k	(3.28)	0.0004	
Prandtl number	Pr	(3.28)	5	
Runoff efficiency factor	μ	(3.36)	10	
Runoff timescale (steep)	τ_{steep}	(3.38), (3.39), (3.40)	0.05	days
Runoff timescale (flat)	τ_{hor}	(3.39), (3.40)	20	days
Runoff timescale (1°)	τ_{1°	(3.40)	2	days
Empirical constant	ν	(3.43)	1	
Empirical constant	β	(3.44)	tuning	
Vapor diffusion coeff.	D_{eff}	(3.46)	1.1×10^{-4}	$m^2 s^{-1}$
Precipitation gradient	γ_p		tuning	
Iteration limit	ΔT_{acc}		0.01	K
Temperature range	ΔT_{max}		40	K

Table 3.2: Physical constants

<i>Description</i>	<i>Symbol</i>	<i>Value</i>	<i>Units</i>
Stefan-Boltzmann constant	σ	5.67×10^{-8}	$W m^{-2} K^{-4}$
Latent heat of vaporization	L_v	2.50×10^6	$J kg^{-1}$
Latent heat of sublimation	L_s	2.83×10^6	$J kg^{-1}$
Latent heat of melting	L_M	3.34×10^5	$J kg^{-1}$
Specific heat of water	c_w	4187	$J kg^{-1} K^{-1}$
Specific heat of dry air	c_p	1006	$J kg^{-1} K^{-1}$
Gravitational acceleration	g	9.81	$m s^{-2}$
Density of ice	ρ_{ice}	917	$kg m^{-3}$
Triple point pressure	p_0	610.5	Pa
Triple point temperature	T_0	273.15	K
Gas constant (dry air)	R_d	287	$J kg^{-1} K^{-1}$
Gas constant (vapor)	R_v	461	$J kg^{-1} K^{-1}$

ice. The subsurface model simulates the vertical profiles in the snow, firn and ice layers of temperature, density and water content, and includes several physical processes that will affect these profiles. The strategy employed for the snow model in this study is based on a routine described by Greuell and Konzelmann (1994). In the coming subsections, a description of the different processes that are contained in the snow model is given.

Melt water percolation, refreezing and runoff

The two sources of water at the surface are melt water and rain water. Melt water is produced as a consequence of a positive energy balance ($Q_M > 0$) at the surface. The total amount of available water per time step W is then given by:

$$W = \left(\frac{Q_M}{L_M} + \dot{r} \right) \Delta t, \quad (3.32)$$

where Δt is the model time step. Note that penetration of shortwave radiation is not included in the model, and thus all the melt water is produced at the surface. If the density of the uppermost subsurface layer is below the density of ice, then the water will percolate into this layer. Refreezing of the percolating water will take place if subsurface temperatures are below freezing point. As a consequence of refreezing, heat is added to the layer and the temperature of the layer will rise. Furthermore, mass is added to the layer, while the thickness remains constant, so the density of the layer will also increase after refreezing. The amount of refreezing in a layer is limited by three factors: the layer temperature (cannot be raised above 0°C), the layer density (not allowed to become larger than the density of ice), and the available amount of water.

After refreezing in the first layer, the remaining water will percolate down into the next layer. A small amount of water is held in the layer by capillary and adhesive forces when no refreezing takes place. This is called irreducible water. The irreducible water content θ_{mi} can be expressed as the ratio of the mass of the irreducible water to the total mass of the layer. We used the following expression by Schneider and Jansson (2004) to describe this ratio as a function of the porosity:

$$\theta_{mi} = 0.0143 \exp(3.3n) \quad (3.33)$$

$$n = 1 - \frac{\rho}{\rho_{ice}}, \quad (3.34)$$

where n is the porosity of the layer, expressed as a function of the layer density (excluding water). The porosity is the ratio of the pore space to the total volume of the layer and has a value between 0 (no pore space) and 1 (100% pore space). Equation (3.33) is an empirical relationship based on laboratory and field measurements. This might explain why θ_{mi} is not equal to zero for a layer with the density of ice. It can be derived that the maximum amount of irreducible water (kg) that can be stored in a layer is equal to

$$m_{liq,max} = \rho_i \Delta z_i \frac{\theta_{mi}}{1 - \theta_{mi}}, \quad (3.35)$$

where Δz_i is the thickness of the i^{th} layer. $m_{liq,max}$ only depends on the density and the thickness of the layer. If the available amount of water in a layer exceeds

$m_{liq,max}$, then the remaining water content will percolate into the next layer ('top-down').

Once all the upper layers are filled to their maximum value with irreducible water and the impermeable ice at the bottom of the firn layer has been reached, the water will start filling the available pore space at the bottom. Now the available water will start accumulating ('bottom-up') and a so-called slush layer is formed.

A fraction of the slush water ($sw(t)$) will runoff every time step following a timescale t_{runoff} , introduced by Zuo and Oerlemans (1996):

$$sw(t) = sw(t - \Delta t) \exp\left(-\frac{\Delta t}{\mu t_{runoff}}\right) \quad (3.36)$$

$$t_{runoff} = c_1 + c_2 \exp(-c_3 \tan s) \quad (3.37)$$

$$c_1 = \tau_{steep} \quad (3.38)$$

$$c_2 = \tau_{hor} - \tau_{steep} \quad (3.39)$$

$$c_3 = -\ln\left(\frac{\tau_{1^\circ} - \tau_{steep}}{\tau_{hor} - \tau_{steep}}\right) (\tan 1^\circ)^{-1}, \quad (3.40)$$

where c_1 , c_2 and c_3 are coefficients, μ is the runoff efficiency factor, s is the surface slope, τ_{steep} , τ_{hor} and τ_{1° are the runoff timescales for water on a steep slope, on a 0° slope and on a 1° slope respectively. Values for τ_{steep} , τ_{hor} and τ_{1° are taken from Reijmer and Hock (2008) (table 3.1). Runoff in the snowpack is less efficient than runoff at the surface. The runoff rate of water in the snowpack is controlled by the efficiency factor μ . The value taken for μ is equal to the value used by Bougamont *et al.* (2005) and Reijmer and Hock (2008) (table 3.1). We assumed that accumulating slush water, which reaches the surface, is removed instantly ($t_{runoff}=0$). When the winter snow pack has disappeared, all the water associated with melting and rain fall will runoff immediately. Note that the amount of irreducible water is not depending on the runoff timescale. The irreducible water content of a layer can only decrease due to a decrease of $m_{liq,max}$ or due to refreezing.

In case of a cold wave penetrating into the firn layer, for example during a clear summer night, temperatures at and below the surface may drop below freezing point. However, refreezing of the available water (slush water + irreducible water) will cause the temperature of the subsurface layers to remain at freezing point. Primarily, the slush water will start refreezing, subsequently followed by the irreducible water in case of absence of slush water.

Temperature profile

The evolution of the subsurface temperature profile in time is described by the thermodynamic equation:

$$\rho c_{p_{ice}} \frac{\partial T_i}{\partial t} = \frac{\partial}{\partial z} \left(\kappa(\rho) \frac{\partial T}{\partial z} \right) + \frac{F_i L_M}{\Delta z_i} - \frac{M_i L_M}{\Delta z_i} + \frac{Q_t}{\Delta z_i}, \quad (3.41)$$

where $c_{p_{ice}}$ is the heat capacity of ice, T_i is the temperature of the i^{th} layer, F_i is the refreezing rate (kg s^{-1}), M_i is the melting rate (kg s^{-1}), and Q_t is the shortwave flux acting on the layer. The first term on the r.h.s. of equation (3.41) is associated with the net heat added to a layer by a vertical gradient in the

diffusive heat flux, as described by equation (3.30). The second term represents the heat added to a layer by refreezing. The third term is the energy loss after melting. This term is always zero in the model, since melting occurs only at the surface and equation (3.41) is only used to calculate temperatures below the surface. The last term describes the heat added to a layer by a penetrating shortwave flux. The contribution of this term is assumed to be negligible and is therefore not taken into account in the model. Finally, the heat capacity of ice $c_{p_{ice}}$ ($\text{J kg}^{-1} \text{K}^{-1}$) is formulated as a function of the layer temperature (Yen, 1981):

$$c_{p_{ice}} = 152.2 + 7.122 T_i. \quad (3.42)$$

Density profile

Density variations below the surface are described by a formulation, which is based on an empirical relation found by Herron and Langway (1980) and later modified and extended by Li and Zwally (2004):

$$\frac{\partial \rho_i}{\partial t} = K_0(T_i) \exp\left(\frac{E(T_i)}{R_d T_i}\right) a_{snow}^\nu \frac{\rho_{ice} - \rho_i}{\rho_{ice}} + \frac{\partial J}{\partial z} + \frac{F_i}{\Delta z_i}, \quad (3.43)$$

where K_0 is the rate factor, E is the activation energy, R_d is the universal gas constant (table 3.2), a_{snow} is the annual snow accumulation (m w.e.), ν is an empirical constant (table 3.1) and J is the water vapor flux.

The three terms on the r.h.s. of equation (3.43) represent the different processes involved in densifying the snow pack. Packing of the snow as a consequence of the pressure developed by the weight of the overlying snow, is expressed in the first term. Herron and Langway (1980) used data from multiple sites in Greenland and Antarctica to find values for E and K_0 . They derived constant values for E and K_0 for snow densities smaller than 550 kg m^{-3} and for snow densities larger than 550 kg m^{-3} . On the other hand, Zwally and Li (2002) assumed the rate factor K_0 and the activation energy E to be a function of the layer temperature T_i :

$$K_0(T_i) = 8.36 \beta |T_i - 273.15|^{-2.061} \quad (3.44)$$

$$E(T_i) = 883.8 |T_i - 273.15|^{-0.885}, \quad (3.45)$$

where β is an empirical constant. These expressions were derived from grain growth data by Jacka and Li (1994), which were used to examine the temperature dependency of the activation energy and the rate factor. The constant β is used to tune the modeled densification rate in such a way that it agrees best with the measured density profiles. A problem with equation 3.45 is that it increases exponentially towards higher temperatures and reaches very large values for snow temperatures close to $0 \text{ }^\circ\text{C}$. This would result in densification rates, due to packing only, of up to 10 kg m^{-3} per half hour, which we assume is only possible when refreezing is taken into account. Therefore, we inferred a cut-off temperature of 272 K above which the densification rate is held constant, as illustrated in figure 3.4.

The second term on the r.h.s. of equation (3.43) is associated with the densification of the snow pack by vapor transport. Unlike the packing process, mass can be added or removed by vapor transport through the surface interface. At the bottom of the snow pack, mass transport between the snow pack and the

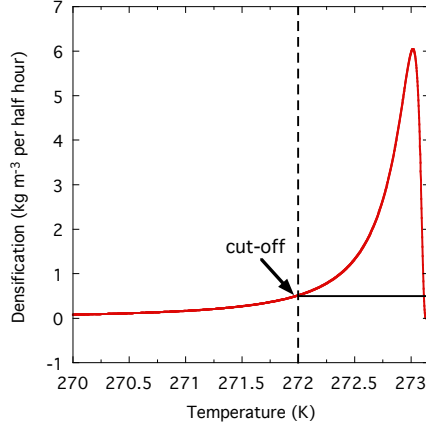


Fig. 3.4: Gravitational densification as a function of snow temperature ($\rho = 300 \text{ kg m}^{-3}$, $\beta = 3$, $a_{snow} = 1000 \text{ mm w.e. yr}^{-1}$). The black line indicates the cut-off at 272 K

impermeable ice is set to zero. The vapor fluxes between the subsurface layers are formulated after Colbeck (1993):

$$J(T_i) = -D_{eff} \frac{p_0}{R_v^2} \frac{L_s - R_v T_i}{T_i^3} \exp \left[\frac{L_s}{R_v} \left(\frac{1}{T_0} - \frac{1}{T_i} \right) \right] \frac{\partial T_i}{\partial z}, \quad (3.46)$$

where D_{eff} is the vapor diffusion coefficient (table 3.1), R_v is the gas constant for water vapor and p_0 and T_0 are the triple-point pressure and temperature, respectively (table 3.2). The vertical temperature gradient $\frac{\partial T_i}{\partial z}$ determines the sign of J . In other words, the direction of the vapor flow between the layers is determined by the vertical temperature profile in the snow pack (vapor flows from higher to lower temperatures). On the other hand, the densification of the snow layers is determined by the vertical gradient of the vapor fluxes $\frac{\partial J}{\partial z}$ (equation (3.43)). If the vapor flux entering a layer is larger than the vapor flux out of the layer, then the layer density will increase. Generally, the net densification due to moisture transport is mainly negative in winter, due to low surface temperatures, especially during the nights. In spring and summer, however, the densification due to vapor transport becomes positive when the sun and atmosphere heat the surface and refreezing releases heat in the upper snow layers, resulting in a downward directed moisture flux. Note that the latent heat fluxes are not responsible for vapor transport through the surface. Q_{LH} only adds or removes mass directly at the surface by sublimation and riming.

The last term on the r.h.s. of equation (3.43) describes the impact of refreezing on the densification rate of the snow pack. The mass added by refreezing is on average of similar magnitude as the densification by gravitational packing. However, refreezing is responsible for the fairly high peak values of densification rate when melting occurs, while the gravitational packing rate is much less variable, as will be shown in section 4.3.

Traditional mass balance measurements do not account for refreezing of percolating water in cold snow/firn and refreezing of irreducible water below the summer surface of the previous year (Schneider and Jansson, 2004). This results in a systematic underestimation of the mass balance in the accumulation zone. The amount of refreezing below the summer surface of the previous year

is called internal accumulation. Note that refreezing *above* the summer surface does not evade accounting in traditional mass balance observations, since density variations above the summer surface are taken into account when measuring the mass balance for the year in question.

Coupling snow model, energy balance model and atmosphere

The subsurface heat flux Q_G is the only component of the surface energy budget (equation (3.2)) that is affected directly by the subsurface snow properties (density and temperature). Due to the impact of Q_G on the surface temperature, other fluxes depending on the surface temperature (LW_{out} , Q_{LH} , Q_{SH} and Q_R) will be influenced too. E.g. after refreezing of meltwater, subsurface temperatures will rise and consequently, the heat flux towards the surface will increase, resulting in a higher surface temperature ($T_{surf} < 0$ °C) or more melting ($T_{surf} = 0$ °C). The energy balance model evaluates all the fluxes at the surface in order to calculate the amount of energy involved in melting (Q_M). The generated melt water together with the rain water forms the input for the snow model, which tracks the water and simulates refreezing, storage and runoff.

The vapor fluxes between the snow pack and the atmosphere are the only direct connection between the snow model and the atmosphere. Mass exchange between the uppermost snow layer and the air directly above the surface will occur as a consequence of vapor transport. The turbulent transport of vapor from the atmosphere to the surface has a direct impact on the surface energy and mass budget and is described by the latent heat flux (equation (3.27)).

3.2 Numerical properties

In the following paragraphs, a description is given of the numerical schemes and methods adopted to implement all the formulations described in the previous sections into the model. Given the amount of formulations that had to be evaluated per time step, the model was set up in such a way that computational costs were minimized. This sometimes resulted in a trade off between accuracy and simulation time, e.g. in choosing the number of subsurface layers. Furthermore, some assumptions had to be made in order to avoid numerical inconsistencies. The flowchart in figure 3.5 gives a summary of the set-up of the model.

3.2.1 Spatial / temporal resolution

The model time step and grid spacing are the main factors controlling the run time of the model. The grid resolution of the model is equal to the resolution of the DEM, which has a horizontal grid spacing of 25 meters in both the north-south and east-west direction. Topographical parameters, like the slope of a grid cell, can vary significantly over small distances. Therefore, a high spatial resolution has been chosen to capture these variations on the expense of more extensive calculations within one time step.

The model time step has been set at half an hour, which was mainly based on the temporal resolution of the measurements. Using a 30-minute time step enabled us to investigate the daily fluctuations in the model results.

The snow model distinguishes between ice ($\rho = \rho_{ice}$) and snow or firn ($\rho < \rho_{ice}$). Depending on the snow thickness, the snow pack is divided into one,

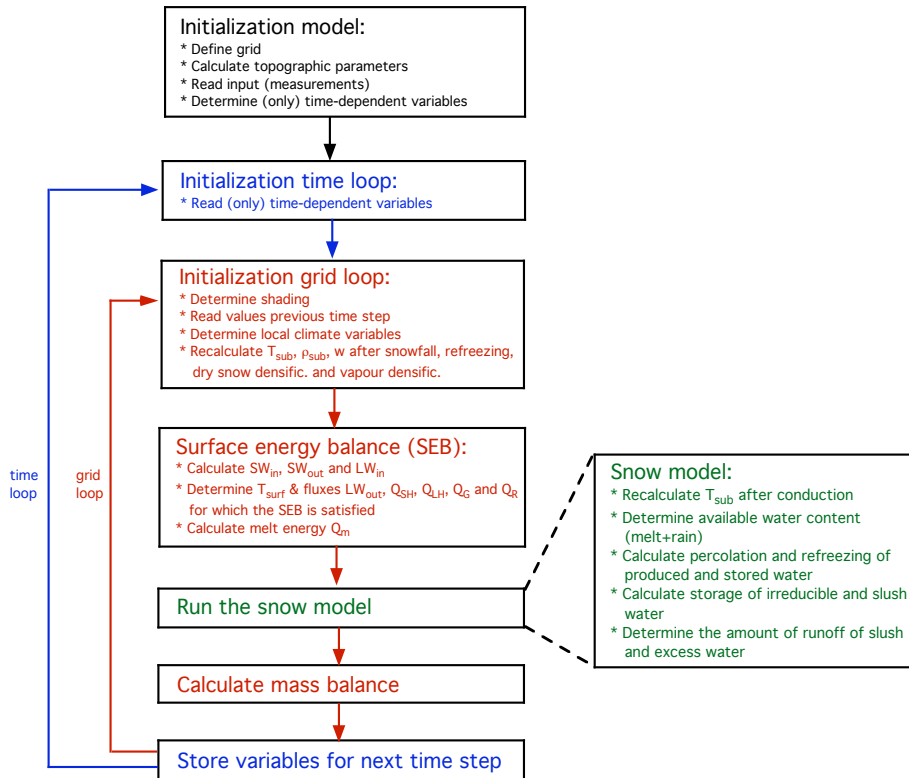


Fig. 3.5: Flow chart of the surface energy model coupled to the subsurface snow model

three or six layers. If the snow thickness is smaller than 0.30 meter, then the entire snowpack is contained in one layer. In case of a snow thickness between 0.30 meter and 1.0 meter, three layers are considered, and if the snow depth is larger than 1.0 meter, then the snow pack is divided into six layers. The thickness of the layers is defined as a certain fraction of the total snow depth, as depicted in figure 3.6. After a change of the number of layers, the vertical profiles are adjusted to the new situation by redistributing the old values. In case of a snow depth smaller than 0.05 meters, numerical artefacts after calculation of the vertical derivatives become significant. Therefore, below this threshold thickness, processes containing these vertical derivatives, like densification and temperature diffusion, are no longer considered in the snow pack. In case of a melting snow pack, the density of this layer has a value equal to the snow density right before reaching the threshold thickness. In case of new snow (<0.05 meter), the density is set to the density of fresh snow ρ_{frsnow} . Underneath the snow pack lies the impermeable ice, of which the upper ten meters are divided into 5 layers (figure 3.6).

Every time the snow thickness changes or when melting of the ice occurs, the vertical distribution of the layer thickness, temperature, density and water content has to be redefined. This procedure takes into account the change of the distance to the surface and the thickness of the layer, and uses this information to adjust profiles to the new situation.

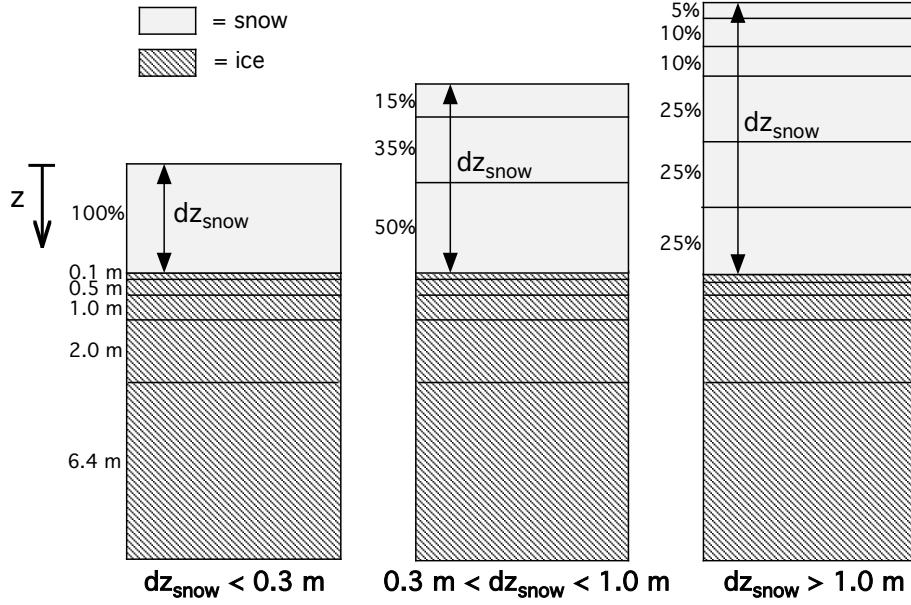


Fig. 3.6: Snow and ice layer distribution. The snow thickness is denoted by dz_{snow} . Percentages indicate the fraction of the total snow depth.

3.2.2 Numerical methods

The techniques used and assumptions made during the development of the model are described here. Numerical schemes were developed to discretize the vertical derivatives, to determine which grid cells are shaded at a certain time and to compute the surface temperature by means of the energy balance. These schemes are summarized in the following paragraphs.

Discretization of vertical derivatives

Discretizing spatial derivatives becomes necessary when a finite amount of spatial steps is considered. Different schemes can be used in models to approximate continuous derivatives. The scheme used here is given in figure 3.7, which shows the method used to calculate subsurface temperature variations after diffusion. A similar scheme is used to calculate the densification due to vapor transport within the snow pack (equation (3.46)), and is therefore not discussed here. The temporal temperature fluctuations $\frac{\partial T_i}{\partial t}$ are depending on the vertical gradient of the subsurface heat flux $\frac{\partial Q_G}{\partial z}$ (equation (3.41)), which again is a function of the vertical derivative of the temperature $\frac{\partial T_i}{\partial z}$ (equation (3.30)). In general, the subsurface heat fluxes are calculated at the interface between two layers by taking the vertical derivative of the temperature of the surrounding layers (central differencing). The derivative is calculated by dividing the temperature difference between the layers by the distance between the mean depths of the two layers. However, at the surface the temperature gradient cannot be defined properly, but a subsurface heat flux at one-fourth of the first layer can be computed (Q_{G_1}). The subsurface heat flux at the surface Q_{G_0} is then calculated by linearly extrapolating Q_{G_1} and Q_{G_2} to the surface, resulting in an expression

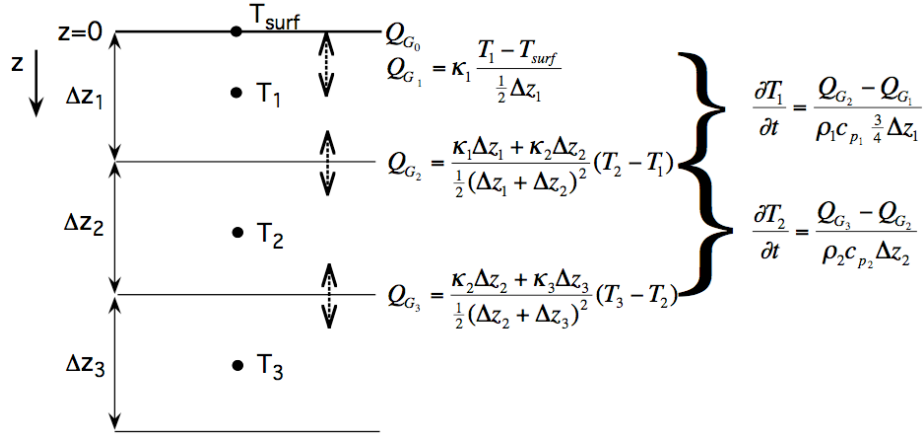


Fig. 3.7: Numerical scheme to calculate vertical gradients of temperature and subsurface heat fluxes.

for Q_{G_0} as a function of Q_{G_1} and Q_{G_2} :

$$Q_{G_0} = \frac{1}{3} (4 Q_{G_1} - Q_{G_2}). \quad (3.47)$$

Once the subsurface heat fluxes are known, we can calculate the temperature deviations by diffusion $\frac{\partial T_i}{\partial t}$ (equation (3.41)) by taking the vertical derivative of Q_G , where the distance over which the derivative is taken is equal to the layer thickness, except for the first layer, where this distance is equal to $\frac{3}{4}$ times the layer thickness.

Topographic shading and terrain factors

Shading occurs when the sun is below the local horizon. The shading module in the model determines whether or not a 'walk' from a grid point to the sun was interrupted by terrain. The walk is prescribed by defining steps in the east-west and north-south direction, depending on the azimuth angle of the sun ψ (equation (3.7)). The model then simulates a walk from a grid point in the direction of the sun's position. For every step, the model determines if the elevation angle of the walk so far is smaller than the solar elevation angle. The walk is stopped when this condition is not met or when the end of the grid (DEM) is reached. If the boundary of the grid is reached, then the grid cell can see the sun and is not shaded at that time. This procedure is repeated every time-step for all the grid points to find the shaded regions at a certain time. The mean shaded fraction of the grid points f_{shad} is shown in figure 3.9(d).

The procedure needed to calculate the terrain factors is quite similar to the method described above. These terrain factors are the sky view factor V_{sky} , the terrain view factor V_{ter} and the ice fraction f_{ice} , which are used in the calculation of the diffuse shortwave radiation coming from the sky I_{sky} and the incoming solar radiation reflected by the surrounding terrain I_{refl} . As in the shading module, once again steps in the direction of the azimuth angle are defined. The main difference with the shading module is that for one grid point the model has to walk in all possible directions of the overlying hemisphere.

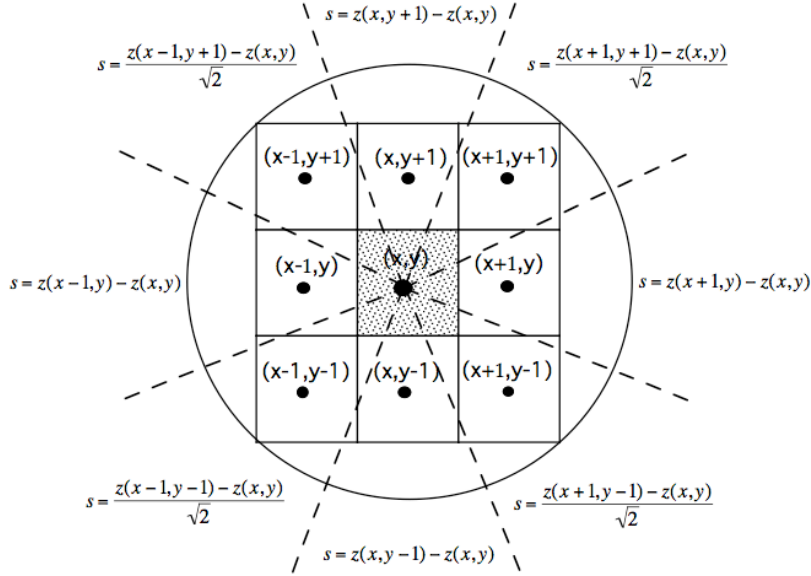


Fig. 3.8: Numerical scheme used to calculate the slope s (on a normalized grid). The slope of the centered grid cell (x, y) is calculated using an expression which is dependent on the azimuth angle. The grid cell is surrounded by eight adjacent grid cells, therefore, eight azimuthal regimes (45° each) are considered. The dashed lines mark the boundaries between the azimuthal regimes. The altitudinal gradient between the centered grid cell and the selected adjacent grid cell determines the slope.

This is done with two loops: one in the azimuthal direction and one from the surface towards the surface zenith angle, using 5° steps in both directions. The loop towards the surface zenith angle starts at an angle that is determined by the slope of the grid cell. Note that the slope of a grid cell varies for different azimuth angles.

Figure 3.8 shows how the surface slope is determined numerically. The slope s is determined by taking the ratio of the height difference between two grid cells and the distance between the cells. For one grid point, the terrain view factor V_{ter} is equal to the ratio of the amount of walks that is interrupted by terrain to the total amount of walks from that cell, resulting in a value between 0 and 1 (figure 3.9(b)). The sky view factor V_{sky} is calculated as one minus the terrain view factor, since the overlying hemisphere is either sky or terrain (figure 3.9(a)). Finally, the ice fraction is the fraction of the visible terrain that is covered by the glacier (figure 3.9(c)).

Computing the surface temperature

Recall that the energy balance (equation (3.2)) is used to determine the surface temperature for which all the incoming and outgoing energy fluxes are in balance. Numerically, this can be done with an iterative procedure that converges towards a value for T_{surf} , for which equation (3.2) is satisfied. It is assumed that the r.h.s. of equation (3.2) is continuously increasing or decreasing with temperature (the derivative with temperature does not change sign). A bi-

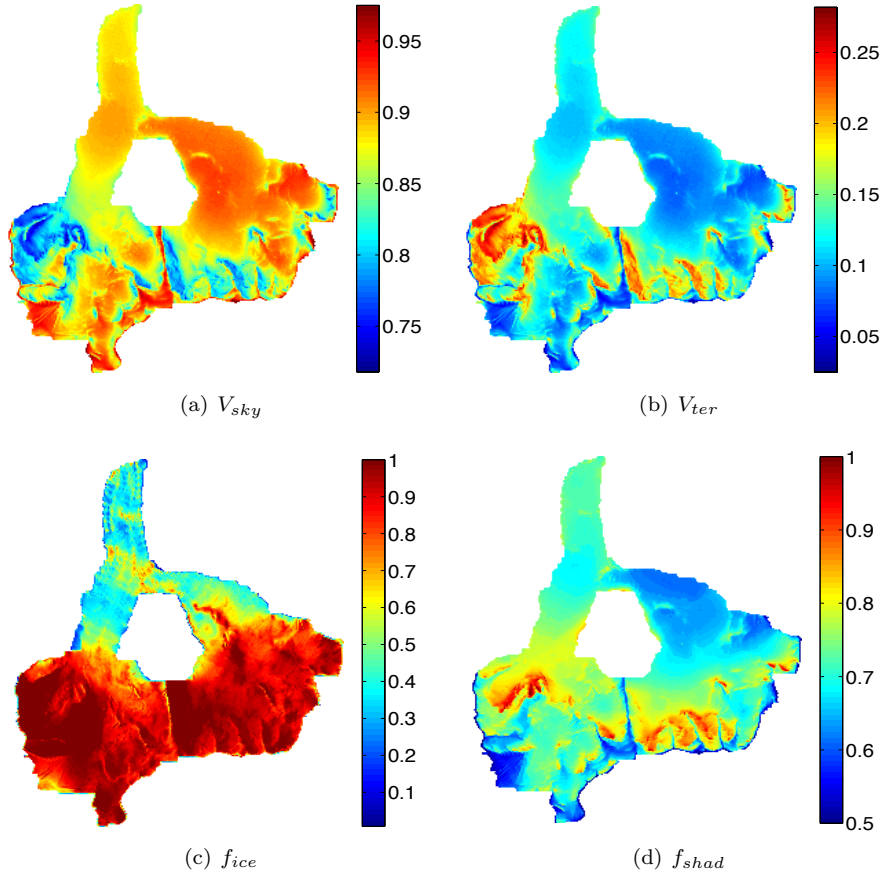


Fig. 3.9: The sky view factor (a), terrain view factor (b), ice fraction (c), and shaded fraction (d).

section routine can then be used to find the value of T_{surf} where the energy budget is equal to zero. The following steps are taken to estimate the surface temperature:

- *Step 1:* Define a starting temperature T_{start} and a maximum temperature range ΔT_{max} . The energy budget at the two extremes has to be of opposite sign, and T_{start} is taken equal to T_{surf} of the previous time step.
- *Step 2:* Compute the energy budget $E(T)$ at the starting temperature.
- *Step 3:* If $E(T_{start})$ and the energy budget at one of the extremes are of opposite sign, then the surface temperature for which E is zero has to lie between T_{surf} and that extreme.
- *Step 4:* Define a new starting temperature halfway between the two temperatures associated with the opposite energy budgets of the previous step, and repeat step 2 and 3.
- *Step 5:* Repeat step 4 until the temperature range ΔT is smaller than a preset limit ΔT_{acc} (table 3.1).

The resulting surface temperature has a numerical accuracy ΔT_{acc} . The energy involved in melting Q_M is not yet included in this method, therefore, surface temperatures higher than 273.15 K can be obtained. In that case, the surface temperature will be set to 273.15 K and $E(273.15)$ is calculated. The resulting positive energy budget is then equal to the melt energy Q_M .

3.2.3 Calibrating the model

Without calibration, the model would not be able to produce results that are in reasonable agreement with measured values. This is a consequence of the imperfection of formulations and input values. To achieve a better agreement, some model parameters are used for calibration. These tuning parameters are usually the constants in the model that are not very well constrained. The main focus of the calibration procedure is to tune the mass balance and its height dependence properly. However, local effects, like wind-driven snow drift and avalanches, which are not taken into account in the model, can have a significant impact on the mass balance, and these uncertainties cannot be fully corrected by changing the parameter set-up of the model.

All the energy fluxes at the surface contribute to the amount of ice melt. However, the turbulent fluxes are probably one of the most uncertain components, because of the generalized formulations. It is therefore justified to use the background turbulent exchange coefficient (C_b) for calibration of the ice melt. Furthermore, the albedo of ice (α_{ice}) is also used to tune the ice melt. The advantage of calibrating the ice melt with either C_b or α_{ice} is that the adjustment mainly affects the mass balance, while the impact on the snow properties (density and depth) is negligible.

The snow depth, snow mass and snow density can be calibrated with several parameters. First of all, the rate factor in the expression for the gravitational densification (β) can be used to tune the densification rate of the snow pack. Secondly, the density of fresh snow (ρ_{frsnow}) can be used to match measured mean snow density at M1 to computed values. Note that the threshold temperature ($T_{s/r}$), related to the transition from snow fall to rain fall and the height dependence of the precipitation (γ_p) can also be adjusted to improve the modeled snow mass and its height dependence. However, adjusting γ_p or $T_{s/r}$ not only affects the snow properties. It also has a significant influence on the amount of ice melt, as will be shown in section 4.1. Since calibrating the mass balance is our main priority, γ_p and $T_{s/r}$ are not used for tuning of the snow properties. On the other hand, changing β or ρ_{frsnow} has an impact on the snow properties, while the effect on the ice melt is negligible.

The shape of snow flakes falling on the glacier may vary strongly from time to time, implying that also the density of fresh snow, ρ_{frsnow} , is not always the same. In the model, the density of fresh snow is taken as a constant, since the measurements reveal little information about the shape and density of the snow flakes. ρ_{frsnow} is tuned (together with the gravitational densification rate β) by comparing with measurements of the mean snow density at M1. However, the chosen value for ρ_{frsnow} is most likely overestimated. On the other hand, it is also likely that the modeled densification rate of the fresh snow right after the snow fall event is underestimated. Thus, picking a larger value for ρ_{frsnow} compensates for the underestimation of the densification rate in the first few days after the snow fall event in order to achieve a better agreement between

modeled and measured mean snow densities.

3.3 Experiments

Sensitivity runs of the tuning parameters play an important role in the determination of the standard set-up for the model. Model results of the relative surface height and snow properties are compared to measurements and deviations are minimized by adjusting the tuning parameters (C_b , α_{ice} , $T_{s/r}$, ρ_{frsnow} , β and γ_p). The amplitude of the adjustments is estimated using the results of previous sensitivity runs. Defining the optimum set-up for the model is a difficult task, mainly caused by the availability of a large amount of observations of several variables at multiple locations on the glacier. First of all, sensitivities are generally not constant with height, making it hard to tune height dependent variables, like the mass balance. Secondly, the model response to perturbations may vary from year to year, which complicated estimation of the model response over a long simulation period. Finally, probably the most important problem is that an adjustment of most of the tuning parameters to improve one variable, also affects several other variables in the model results. It is therefore a great challenge to find a standard parameter set-up for which model results are in good agreement with all the available observations.

Several parameter sensitivity experiments are done with the model in order to test the response to perturbations in the parameter set-up. Not only the response to changes in the tuning parameters, but also the sensitivity to changes in other parameters are investigated. Generally, the model sensitivity to variations in the parameter set-up is calculated after running the model for two years. However, for $T_{s/r}$, the sensitivity of the mass balance as a function of altitude shows a strong year-to-year variability. In this case, a longer simulation period of four years is chosen to reduce the significance of individual events on the mass balance sensitivity. In order to determine the standard set-up of the model, simulations over the period from 1995 to 2008 are performed to compare the model output to observations.

The mass balance sensitivity to prescribed changes in the climate variables (atmospheric temperature and precipitation) are also calculated. The sensitivity of the mass balance to these variations is determined using model runs of five years.

Additional runs are performed to investigate the importance of inclusion of refreezing in the model and to test the effect of a constant ice albedo on the results. Furthermore, the model is also run with the parameter set-up proposed by Klok and Oerlemans (2002) in order to assess the impact of the more comprehensive snow model in this study on the model set-up. Finally, a simulation with the standard set-up of the model is done over the entire measurement timeseries (around the glacier) extending from 1983 to 2008.

Values for the initial subsurface snowdepth, temperatures and densities are derived from the output of an initialization run starting three months before the actual run. For the three months prior to the start of the long run, which starts at 1 January 1983 and ends at 16 August 2008, air pressure data at Corvatsch and Samedan are missing and therefore estimated by taking an estimated (mean) value. The results of all the aforementioned experiments will be addressed in the next chapter.

Chapter 4

Results

In this chapter, the main results of the model are presented and a comparison with observations is made. The chapter is divided into five sections, discussing the parameter sensitivity of the model (section 4.1), the surface mass and energy balance (section 4.2), the subsurface variables (section 4.3), the results of some additional experiments (section 4.4) and finally, the climate sensitivity of the model (section 4.5).

4.1 Parameter sensitivity

Sensitivity experiments provide valuable information on the stability of the model. Furthermore, these runs are useful to examine which parameters, and thus processes, play a dominant role in the calculation of the mass balance. Clearly, the mass balance sensitivity of the model is our main concern. However, also the response of the snow properties (density, mass and depth) to perturbations in the model parameters is investigated and considered in the determination of the standard parameter set-up.

Table 4.1 shows the mean sensitivity of the modeled mass balance, snow density and surface temperature to changes in several model parameters. Both positive and negative perturbations to the standard parameter set-up are applied to test the linearity of the model response. It can be seen that the mass balance is very sensitive to changes in parameters that determine the surface albedo (α_{ice} , α_{frsnow} , t^* and d^*). Additionally, the mass balance is strongly dependent on the amount of snow accumulation, which is mainly affected by the threshold temperature ($T_{s/r}$) and the precipitation gradient (γ_p). The mean density of the snowpack is strongly influenced by variations in the gravitational densification rate factor (β), the fresh snow density (ρ_{frsnow}) and again the albedo parameters (except α_{ice}). Finally, the surface temperature is also depending on the albedo parameters (except α_{ice}) as well as on the background turbulent exchange coefficient (C_b).

Clearly, the albedo parameters have a major impact on several variables in the model output. Note that a small perturbation of α_{frsnow} has a remarkably strong influence on the mass balance. This is due to the fact that the relative amount of absorbed solar radiation is strongly dependent on the value of α_{frsnow} in case of a recent snow fall event. E.g. if the surface albedo, right after snowfall

Table 4.1: Mean mass balance sensitivity (ΔMB), snow density sensitivity ($\Delta\rho$) and surface temperature sensitivity (ΔT_{surf}) to perturbations of the standard model parameters. The main tuning parameters are colored red. A description of the model parameters can be found in chapter 3. Note that Δz_{ice1} is the thickness of the uppermost ice layer. The standard values represent the best estimates after comparing the model results to observations.

<i>Parameter</i>	<i>Standard value</i>	<i>Perturbation</i>	ΔMB (<i>m w.e. a⁻¹</i>)	$\Delta\rho$ (<i>kg m⁻³</i>)	ΔT_{surf} (<i>K</i>)
C_b	0.0032	-0.0010 +0.0010	+0.072 -0.073	-1.22 +1.14	-0.273 +0.247
α_{ice}	0.32	-0.05 +0.05	-0.101 +0.100	+0.97 -0.88	+0.009 -0.009
γ_p (m km ⁻¹)	0.25	-0.1 +0.1	-0.124 +0.121	+0.68 -0.54	+0.007 +0.004
β	3.0	-1.0 +1.0	+0.004 +0.013	-15.87 +11.78	-0.015 +0.013
ρ_{frsnow} (kg m ⁻³)	230	-40 +40	-0.006 +0.002	-22.76 +22.29	-0.025 +0.025
$T_{s/r}$ (K)	274.4	-0.5 +0.5	-0.148 +0.158	-0.39 +1.61	+0.037 -0.032
p_{sea} (hPa)	1020	-10 +10	+0.004 -0.004	-0.19 +0.13	-0.009 +0.010
D_{eff} (m ² s ⁻¹)	1.1×10^{-4}	-0.2×10^{-4} $+0.2 \times 10^{-4}$	+0.002 -0.003	+0.34 -0.38	+0.001 +0.001
ρ_{ice} (kg m ⁻³)	917	-20 +20	-0.004 +0.006	+2.32 +2.02	-0.006 +0.007
α_{frsnow}	0.90	-0.05 +0.05	-0.209 +0.169	+15.32 -12.18	+0.427 -0.426
α_{firn}	0.53	-0.05 +0.05	-0.058 +0.059	+3.01 -2.71	+0.078 -0.078
Δz_{ice1} (m)	0.10	-0.05 +0.05	-0.024 +0.021	+1.62 -0.55	-0.024 +0.019
κ	Eq. (3.31)	$\times 2$ $/2$	+0.077 -0.077	-2.98 +3.38	+0.141 -0.091
μ	10	$\times 5$ $/5$	-0.003 +0.023	+0.63 -0.01	0.000 +0.009
θ_{mi}	Eq. (3.33)	$\times 2$ $/2$	+0.029 -0.018	+1.27 -0.99	+0.016 -0.011
t^* (days)	21.9	$\times 2$ $/2$	+0.197 -0.434	-6.86 +24.33	-0.258 +0.543
d^* (mm w.e.)	11	$\times 2$ $/2$	-0.201 -0.058	+11.83 +0.23	+0.212 +0.119

Table 4.2: Comparison of the modeled mass balance sensitivity to values found by Klok and Oerlemans (2002) for the year 1999.

Parameter	Perturbation	ΔMB (m w.e. a ⁻¹)	
		This study	Klok and Oerlemans (2002)
C_b	+0.0005	-0.037	-0.04
$T_{s/r}$ (K)	-0.5	-0.148	-0.14
γ_p (m km ⁻¹)	-0.05	-0.062	-0.07
α_{ice}	-0.04	-0.081	-0.07
	-0.08	-0.162	-0.15

occurred, is perturbed by 0.05 from 0.90 to 0.95, then the amount of absorbed shortwave radiation will decrease by 50%, leading to a strong lowering of the surface temperature, since other balancing energy fluxes are generally small in wintertime. Perturbations of the firn albedo (0.53) and the ice albedo (0.32) will result in smaller deviations of the surface temperature and thus the ice melt, because the relative effect on the absorbed radiation is smaller and this effect is more easily balanced by the other T_{surf} -dependent energy fluxes, which are generally large in summertime.

For tuning purposes, parameters are chosen, which mainly affect either the mass balance or the mean snow density and snow depth. The mass balance is therefore calibrated by adjusting $T_{s/r}$, C_b , α_{ice} and γ_p . On the other hand, the snow density and depth are tuned with the parameters β and ρ_{frsnow} .

Table 4.1 also shows that the modeled mass balance is not very strongly reacting on perturbations of the subsurface parameters β , ρ_{frsnow} , D_{eff} , ρ_{ice} , κ , μ and θ_{mi} . For most of the sensitivity experiments, the model response to perturbations is approximately linear. Exceptions are the clearly nonlinear response of the model to variations of t^* and d^* .

In table 4.2, simulated mass balance sensitivities over the period 1995-2000 are compared to values found by Klok and Oerlemans (2002) for the year 1999. Generally, the sensitivities agree rather well, which is an indication that the implementation of the snow model in this study has a small impact on the mass balance sensitivity.

Figure 4.1 shows the sensitivity of the mass balance (a), mean snow density (b) and surface temperature (c) as a function of height for the tuning parameters. The height dependence of the mass balance sensitivity is used to pick parameters for the calibration of the relative surface height, which is measured at five different altitudes.

The mass balance sensitivity of the parameter $T_{s/r}$ (snow to rain transition) has a pronounced peak around the equilibrium line altitude, which is caused by a slight shift of the equilibrium line after a change in the snow accumulation. The largest vertical gradients in the mass balance profile are found in this region as a result of strongly varying albedo with height during the melting season. Thus, an upward or downward shift of the mass balance profile has its largest impact on the specific mass balance around the equilibrium line.

Vertical mass balance sensitivity profiles for the turbulent exchange coefficient (C_b) and the ice albedo (α_{ice}) show a steady decrease with height. The parameter C_b depends on the temperature deficit at the surface, which is on average largest in the lower regions, with high atmospheric temperatures and surface temperatures limited at 0 °C. Note that a perturbation of C_b has a rel-

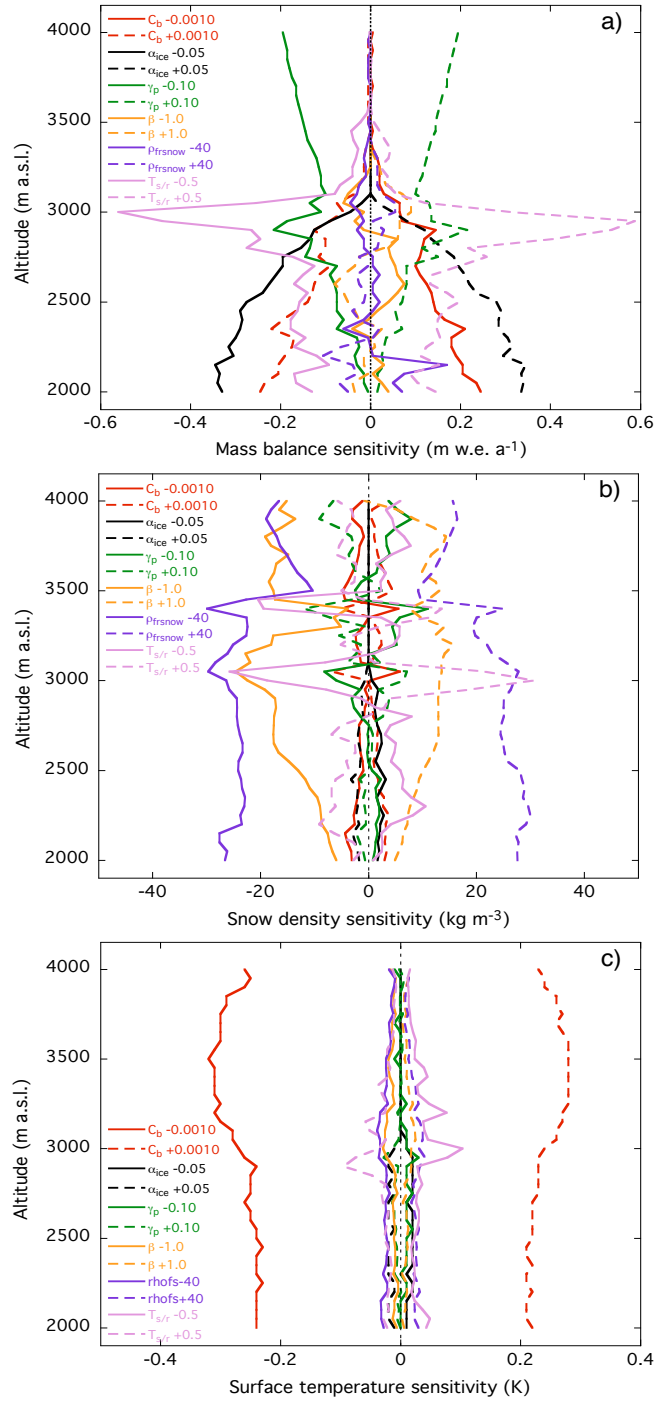


Fig. 4.1: Mass balance sensitivity (a), mean snow density sensitivity (b) and surface temperature sensitivity (c) versus height for perturbations of the standard values of C_b , α_{ice} , γ_p , β , ρ_{frsnow} and $T_{s/r}$.

atively large impact on the surface temperature (figure 4.1(c)), which indicates that turbulent fluxes play a key role in the determination of this temperature, as will be discussed later. The modeled mass balance sensitivity after a change in the ice albedo is largest in regions where the ice surface is exposed initially, resulting in a high sensitivity to perturbations of this parameter at the glacier tongue.

The vertical precipitation gradient (γ_p) is the only tuning parameter showing a mass balance sensitivity that is increasing with height even in the accumulation zone. The peak around the equilibrium line can be explained following the same reasoning as in the explanation of the peak after a perturbation of $T_{s/r}$. The snow density and surface temperature sensitivities for changes in γ_p are small. However, varying γ_p does have a considerable impact on the simulated snow mass and thus on the snow depth.

Finally, the gravitational densification rate factor (β) and fresh snow density (ρ_{frsnow}) have a negligible influence on the mass balance. However, these parameters do have a significant impact on the mean snow density, and thus on the snow depth, as shown in figure 4.1(b), and are therefore used for tuning of the snow properties.

The sensitivity of the mass balance to fluctuations of climatic variables (air temperature and precipitation) is discussed in section 4.5. In the next section, the simulated components of the surface mass and energy balance are presented.

4.2 Components of the mass and energy balance

In this section, the modeled components of the mass and energy budget will be presented. When available, a comparison with observations and other studies is made. The section is divided into two parts discussing first the spatial and then the temporal variations of these components.

4.2.1 Spatial variations

Mass balance

Figure 4.2(a) shows the height dependence of the mass balance and the different mass fluxes that determine the mass balance (see equation (3.1)). The mass balance is mainly controlled by the runoff term (R) in the ablation zone and by the snow accumulation term (P_{snow}) in the accumulation zone. Runoff in the ablation zone is determined by both surface runoff of melt and rain water and runoff of slush water below the surface, while runoff in the accumulation zone is fully determined by the runoff of slush water only. Note that rainwater contributes to the mass balance in case of refreezing (see section 4.3). Both the vapor exchange between the atmosphere and the surface (latent heat flux) and the vapor transport through the surface (V) do not have a major impact on the mass balance. The mean altitude of the equilibrium line over the simulation period (1983-2008) can be estimated from this graph (zero specific mass balance) and is found at a height of approximately 3000 m a.s.l.

Figure 4.2(b) shows the spatial distribution of the specific mass balance. Values of the annual mean mass balance range from -6.56 m w.e. a^{-1} at the tongue to $+1.38$ m w.e. a^{-1} in the accumulation zone. Spatial variations in the mass balance are mainly determined by geographical properties, like the altitude

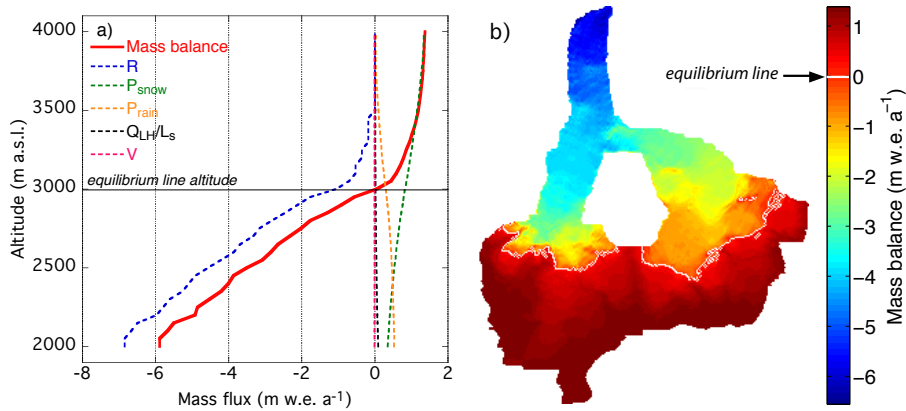


Fig. 4.2: *Left (a):* Yearly mean modeled mass balance (thick red line) and the components that determine the mass balance (dashed lines) as a function of height for the period 1983-2008. The mass balance profile is the sum of the dashed lines. [R =runoff, P =precipitation, Q_{LH}/L_s =sublimation/riming, V =vapor transport through the surface]. *Right (b):* The spatial distribution of the mean annual mass balance over the period from 1983 to 2008. The equilibrium line is represented by the white line (zero mass balance).

and aspect of the grid cell, the amount of shading and the terrain view factor. Small-scale variations in the surface properties, like the slope, sometimes result in strong gradients in the mass balance pattern (note the similarities between the mass balance in figure 4.2(b) and the slope in figure 2.5(b)). Refreezing of melt water also has a significant impact on the mass balance, as will be shown in section 4.3.

Surface energy balance

In figure 4.3, the spatial distribution of the different components that make up the energy budget is given (see equation (3.2)). These patterns will be discussed briefly here.

The *net shortwave radiation* (figure 4.3(a)) is on average the major source of energy at the surface with values ranging from 15 to 73 W m⁻². By virtue of its linear dependence on the albedo, a large gradient in the net shortwave radiation is found around the mean equilibrium line altitude. Furthermore, spatial variations in the geographical parameters, like the terrain view factors and the amount of shading, result in small-scale gradients in the net shortwave budget. The spatial patterns of the mass balance (figure 4.2(b)) and albedo, shown in figure 4.4, look very similar, which is an indication of the mass balance being strongly dependent on the formulation of the albedo, as is already shown in the previous section. Values of the annual mean albedo vary from 0.58 at the tongue to 0.85 in the accumulation zone (figure 4.4). A clear gradient in the mean albedo can be found around the equilibrium line, which marks the extent of the ablation zone during the year. It should be stressed that the altitude of the equilibrium line is not necessarily located at the lower margin of the snow pack at the end of the ablation season. Superimposed ice may reach the surface in the area above the equilibrium line, resulting in a lower albedo, which

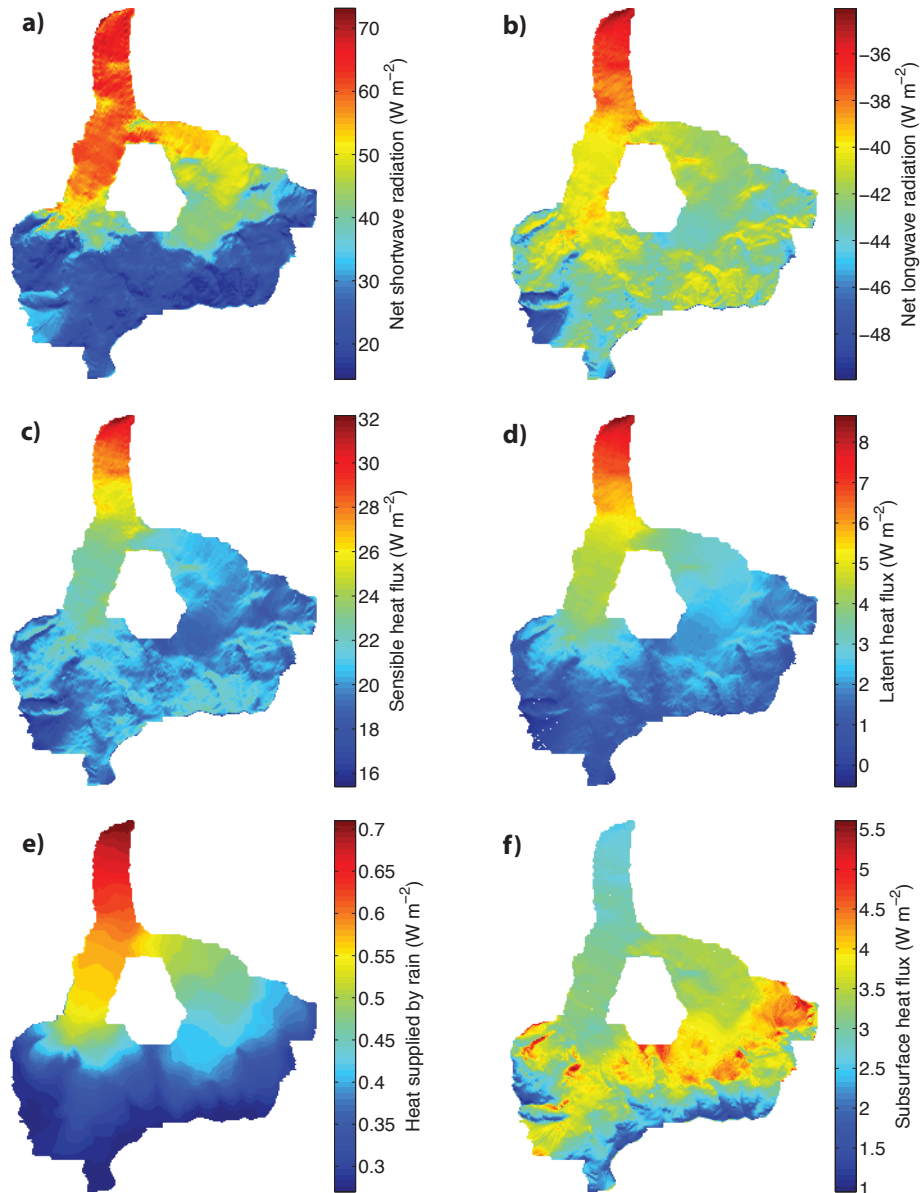


Fig. 4.3: Spatial distribution of the modeled net shortwave radiation (a), net longwave radiation (b), the sensible heat flux (c), the latent heat flux (d), the heat supplied by rain (e) and the subsurface heat flux (f) averaged over the period from 1983 to 2008.

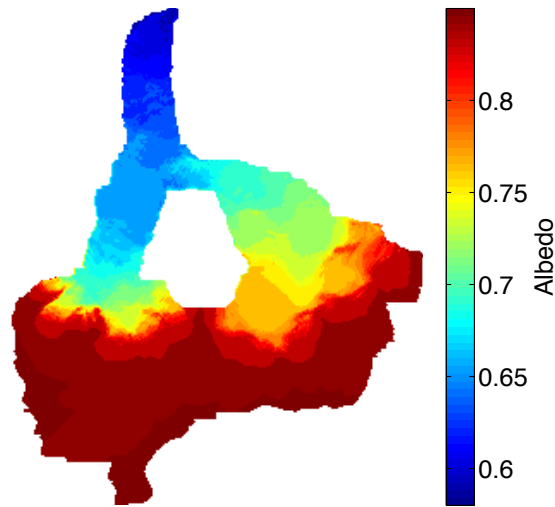


Fig. 4.4: The spatial distribution of the mean albedo over the period from 1983 to 2008.

could make it more difficult to estimate the altitude of the equilibrium line by eye. However, for the Morteratsch glacier, the superimposed ice layer on top of the impermeable ice can be distinguished rather easily from the bare ice in the ablation zone (personal communication, Reijmer, 2009).

The major (and only) sink of energy is the *net longwave radiation* (figure 4.3(b)). At higher altitudes, where air temperatures are usually lower (LW_{in} smaller), most negative values of the net longwave radiation are found, despite the lower mean surface temperatures (LW_{out} smaller). Recall that the cloud cover is spatially invariant over the entire glacier, but it does have a large impact on the amount of incoming longwave radiation.

The turbulent fluxes are on average adding energy to the surface. Both the *sensible heat flux* (figure 4.3(c)) and the *latent heat flux* (figure 4.3(d)) are a function of the temperature gradient between the atmosphere and the surface. Consequently, largest values of the turbulent fluxes are found at the glacier tongue where the air temperature can become much larger than the surface temperature, which cannot be raised above 0 °C. The sensible heat flux is on average about eight times larger than the latent heat flux.

The mean contribution of the *heat supplied by rain* (figure 4.3(e)) to the annual energy budget is small. Values range from ~ 0.3 to ~ 0.7 W m^{-2} , mainly depending on the amount of rainfall. As mentioned before, peak values of the heat supplied by rain of up to 150 W m^{-2} are obtained during heavy rainfall events in summer.

The spatial pattern of the *subsurface heat flux* (figure 4.3(f)) is quite strongly influenced by refreezing of meltwater. The corresponding heat release increases subsurface temperatures, resulting in a more positive subglacial heat flux towards the surface. Therefore, largest values of the glacier heat flux are found in regions where refreezing is prominent, which is in the area around the equilibrium line (see also section 4.3). Above this region, surface temperatures are generally lower and melting occurs less frequently, resulting in less refreezing. Below this region, refreezing is limited by the absence of a snow pack during

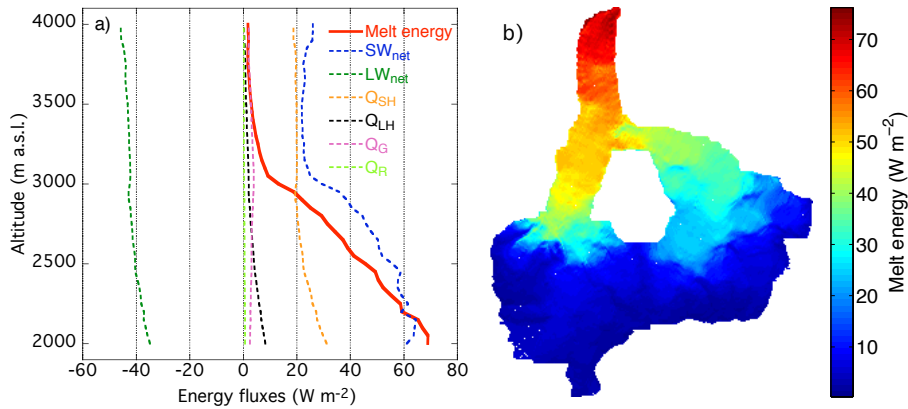


Fig. 4.5: *Left (a):* Mean modeled energy involved in melting (thick red line) and the components that determine the energy budget (dashed lines) as a function of height for 1983–2008. The melt energy profile is the sum of the dashed lines. *Right (b):* Spatial distribution of the mean energy involved in melting over the period from 1983 to 2008.

part of the melting season. In absence of snow, melt water will runoff immediately. The sum of the fluxes in figure 4.3 (a) to (f) is equal to the amount of energy involved in melting (‘melt energy’) and is shown in figure 4.5(b).

Figure 4.5(a) shows the height dependence of the melt energy, together with the different components of the energy budget. The melt energy is greatest at the snout of the glacier and decreases gradually with height towards the equilibrium line, above which the melt energy keeps decreasing at a lower rate towards 0 W m^{-2} . In the ablation zone, the energy involved in melting is strongly influenced by the large contribution of the net shortwave budget. In the accumulation zone, the sensible heat flux and the net shortwave radiation are almost of similar magnitude. Thus, the relative influence of the sensible heat flux on the surface energy budget is very large in the accumulation zone and accurate estimates of the sensible heat flux are therefore of great importance to accurately estimate the surface temperature and specific mass balance, especially at higher altitudes. Note that near the glacier terminus, the sum of the turbulent fluxes (Q_{SH} and Q_{LH}) is on average larger than the magnitude of the net longwave radiation, resulting in a melt energy, which is greater than the net shortwave radiation.

4.2.2 Temporal variations

Net mass balance

Figure 4.6 shows the net mean mass balance over the period 1983–2007. In figure 4.6(a), a comparison to net mass balance observations at six glaciers in the vicinity of the Morteratsch glacier is made. Mass balance data of these six glaciers are provided by National Snow and Ice Data Center (NSIDC). In figure 4.6(b), the net mass balance is shown, together with the summer and winter balance. Until the year 2000, the net mass balance appears to be approximately constant ($\sim -0.60 \text{ m w.e. a}^{-1}$). Thereafter, the year 2001 is the only

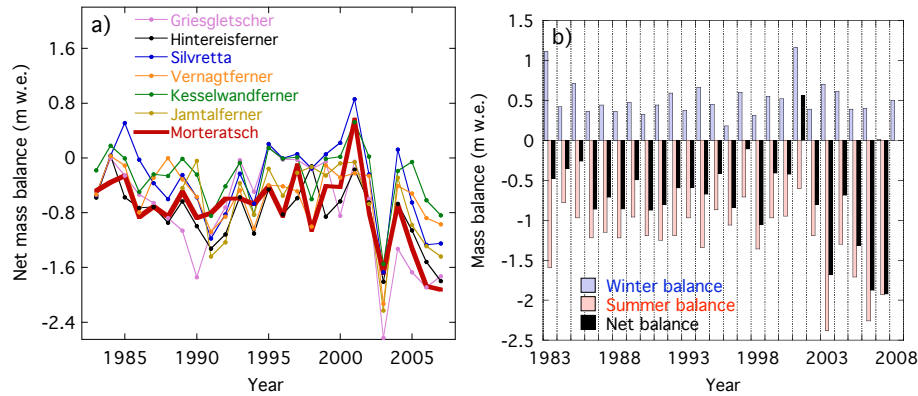


Fig. 4.6: *Left (a):* Simulated net mean mass balance (m w.e. a⁻¹) for the Morteratsch glacier compared to the measured net mass balance of six other glaciers in the Alps. *Right (b):* The net mass balance (black), winter balance (blue) and summer balance (red) of the Morteratsch glacier.

year during the simulation with a positive net mass balance, mainly caused by extensive snow fall. Since 2001, the net mass balance rate becomes increasingly negative with values up to almost -2 m w.e. a⁻¹ for the years 2006 and 2007. The decreasing net mass balance over the last few years is mainly the effect of higher melt rates during the summer, resulting in a more negative summer mass balance, as can be seen in figure 4.6(b). The mean mass balance rate over the entire simulation period is equal to -0.78 m w.e. a⁻¹. For comparison, Klok and Oerlemans (2004) computed a net mean mass balance of -0.76 m w.e. a⁻¹ for the years 1982-2002, using a similar parameterization of the albedo. The modeled net mass balance seems to match rather well with observations of the net mass balance of the six other glaciers when comparing the modeled and measured variability and peak periods (figure 4.6(a)). The relatively negative mass balance values for the years 2005-2007 might well be a consequence of the rather crude assumption that the ice albedo measured at M1 is representative for the ice albedo of the entire ablation zone. A less dramatic decrease of the ice albedo in the higher ablation areas seems more realistic, however, albedo observations at multiple locations on the glacier are required to verify this.

The altitudinal mass balance gradient in the ablation zone is 0.006 m w.e. a⁻¹ m⁻¹, which is a typical value for glaciers in not too dry conditions. The mass balance gradient is mainly the result of the atmospheric temperature lapse rate and the mean albedo gradient with height.

Components of the surface energy budget

Figure 4.7 displays the shortwave fluxes (a), longwave fluxes (b), turbulent fluxes (c) and the subsurface heat flux (d) at M1 (figure 2.4) as a function of time for the period from 1 January 1999 to 1 January 2007. The pronounced seasonality in the incoming shortwave radiation is a direct result of variations of the daily mean incidence angle during the year (figure 3.2(a)). The relative difference between the incoming and reflected radiation is by definition fully determined by the surface albedo. After the snow pack has disappeared, a sudden drop

4.2. COMPONENTS OF THE MASS AND ENERGY BALANCE

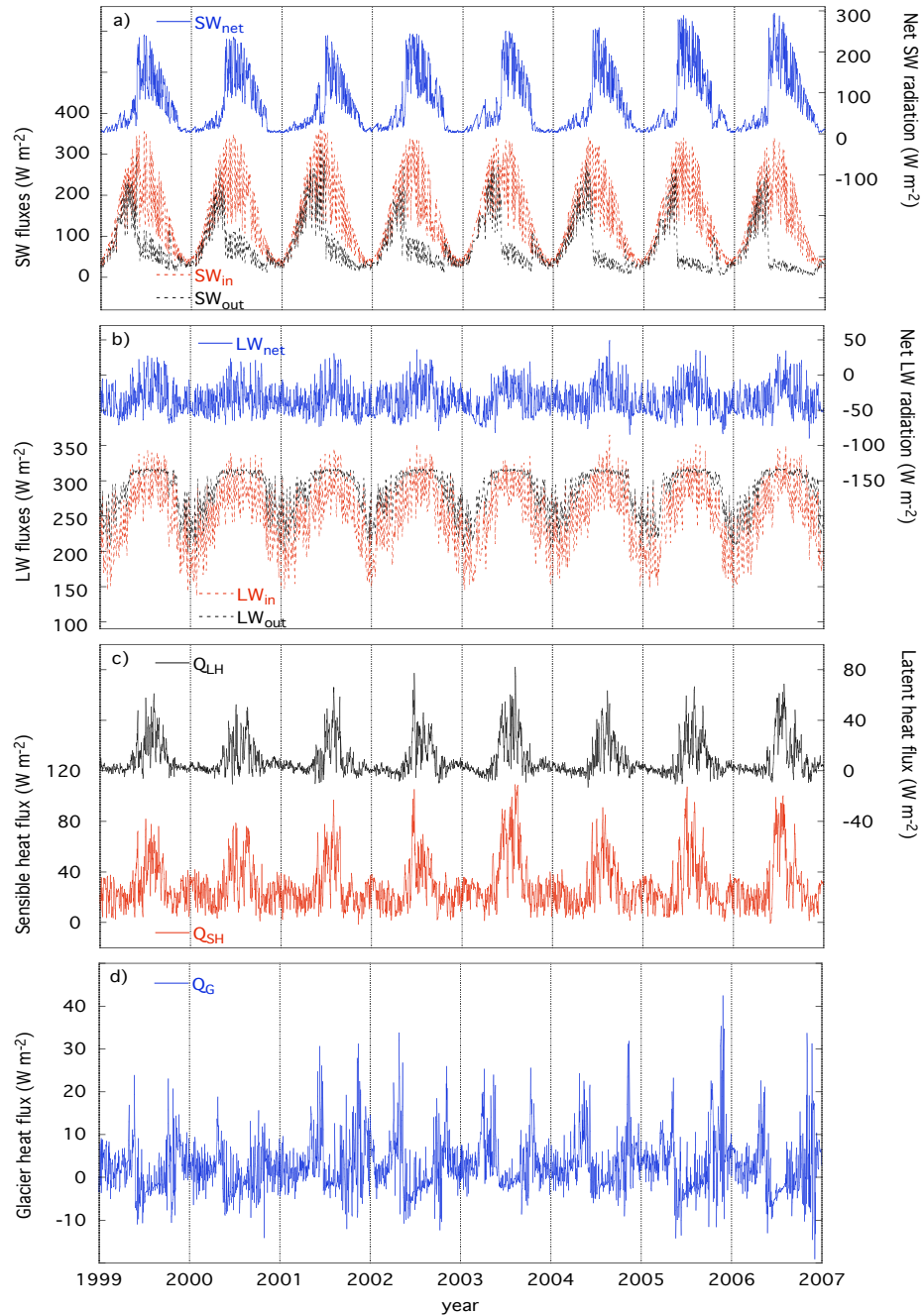


Fig. 4.7: Computed daily mean shortwave radiation (a), longwave radiation (b), turbulent fluxes (c) and the glacier heat flux (d) at M1 (2110 m a.s.l.) for the period from 1 January 1999 to 1 January 2007.

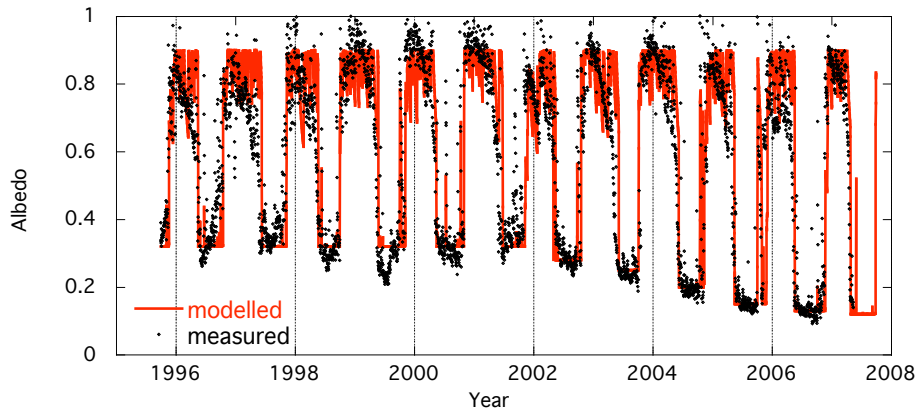


Fig. 4.8: Modeled and measured daily mean albedo at M1 (2110 m a.s.l.). The albedo of ice was taken constant until 2001 and decreases gradually for the period from 2002 to 2008.

in the albedo is observed, since the albedo of bare ice is much lower than the albedo of (old) snow. This results in a much lower reflected shortwave radiation and thus the net shortwave radiation becomes strongly positive, thereby adding a lot of energy to the surface energy budget.

Figure 4.8 shows the modeled and measured albedo at M1 as a function of time. A clear drop in the observed albedo can be seen after 2001. This was the main reason to adjust the parameter α_{ice} manually for the period from 2002 to 2008. Oerlemans *et al.* (2009) argued that this substantial darkening is caused by accumulation of mineral and biogenic dust particles, which is coming from exposed side moraines along the glacier. The height dependence of the debris deposition is to a large extent unknown, which complicates accurate estimation of the albedo of ice especially for the last few years. At M1, the modeled albedo seems to match the measured albedo reasonably well, although in spring the mean albedo is systematically overestimated. Other discrepancies occur when simulated snow fall is under- or overestimated as compared to observations. Summer snow fall events can have a significant temporary effect on the albedo and thus on the ice melt and mass balance as described by Oerlemans and Klok (2004). Furthermore, in winter the observed surface albedo sometimes exceeds the maximum albedo in the model (0.90). The modeled mean albedo is underestimated by 0.013, as is shown in table 4.3. We found a correlation coefficient of 0.81 and a root mean square error (rms) of 0.20 for the years 1995-2007. Oerlemans and Knap (1998) fitted the modeled albedo to a one-year data set by optimizing the albedo parameters in order to minimize the rms, resulting in an optimized rms difference of 0.067 and a correlation coefficient of 0.93.

The computed longwave fluxes in figure 4.7(b) also show a pronounced seasonal cycle, which is directly related to the annual cycle in the atmospheric temperature. During the accumulation season, surface temperatures and air temperatures are generally low, resulting in low values of the outgoing and incoming longwave radiation, respectively. The incoming thermal radiation is mostly smaller than the outgoing radiation, mainly due to a lower emissivity of the sky as compared to the emissivity of the surface, which is assumed to

4.2. COMPONENTS OF THE MASS AND ENERGY BALANCE

Table 4.3: Comparison of mean model results to observations at M1 for the entire period of observations. Absolute differences and correlations are given. The correlations between modeled and measured radiative budgets (SW_{net} , LW_{net}) and input variables (T_{atm} , p_{air} , RH and n) are based on daily mean values.

<i>Variable</i>	<i>Mean modeled</i>	<i>Mean measured</i>	<i>Difference</i>	<i>Correlation</i>
SW_{net} (W m^{-2})	67.2	69.6	-2.4	0.91
LW_{net} (W m^{-2})	-35.4	-41.6	+6.2	0.79
α	0.583	0.596	-0.013	0.81
T_{atm} ($^{\circ}\text{C}$)	0.30	1.44	-1.14	0.97
p_{air} (hPa)	787.6	788.1	-0.5	0.99
RH (%)	74.3	62.5	11.8	0.76
n	0.52	0.49	+0.03	0.79
Snow depth (m)	0.569	0.586	-0.017	0.89
Snow density (kg m^{-3})	287	317	-30	0.66
Snow mass (m w.e.)	0.23	0.26	-0.03	0.91
Snow temperature ($^{\circ}\text{C}$)	-7.5	-3.8	-3.7	0.88

emit as a blackbody. However, on warm summer days, the air temperature is high (LW_{in} large) and the surface temperature is limited at 0°C (LW_{out} small), which may lead to a positive net longwave radiation. Therefore, a seasonal cycle is found in the net longwave budget with on average less negative values during the melting season.

The modeled time-series of the sensible heat flux and the latent heat flux (figure 4.7(c)) shows a somewhat similar pattern, with highest values during the ablation season as a consequence of large temperature gradients between the surface and the atmosphere. Fluctuations in the sensible heat flux tend to be larger than variations in the latent heat flux. The sensible heat flux (equation (3.26)) is mainly a function of the temperature deficit (quadratic relation), while the latent heat flux (equation (3.27)) is mainly determined by both the temperature deficit at the surface (linear relation) and the vapor pressure gradient. During the accumulation season, the latent heat flux is generally very small, due to small gradients in the vapor pressure. The sensible heat flux can still become quite substantial in the winter season through its stronger dependence on the temperature deficit. Recall that the vapor pressure itself is strongly dependent on the air temperature, as described by equation (2.3).

The subsurface heat flux (figure 4.7(d)) is mainly positive during the accumulation season and negative during the ablation season, resulting in cooling and warming of the snow pack, respectively. In wintertime, subsurface temperatures are on average higher than the surface temperature, which reacts more directly to changes in the air temperature, as will be shown in section 4.3. Moreover, negative subsurface heat fluxes during the ablation season are a consequence of the fact that the subsurface temperatures react more slowly to increasing air temperatures than the surface temperature. It can be seen that the glacier heat flux is gradually becoming less negative during the ablation season, as a result of this lagging response of the subsurface temperatures. Note that the temperature at a depth of ten meters below the snow/ice interface is fixed at 0°C , which implies that no downward directed heat transport will occur through the interface at this depth, which is a reasonable assumption for temperate glaciers

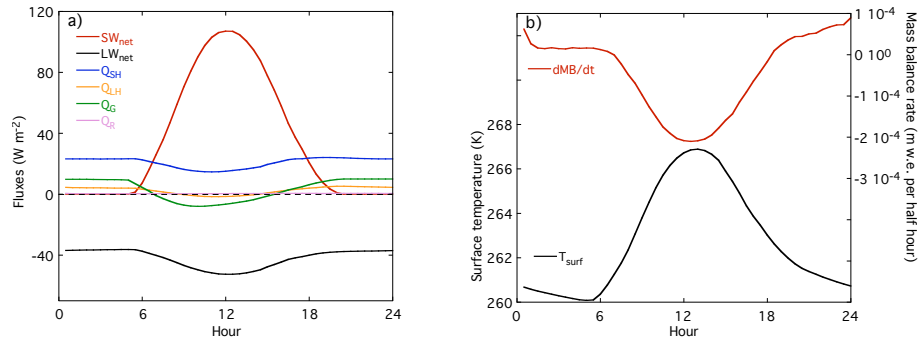


Fig. 4.9: Modeled fluxes (a), surface temperature and mass balance rate (b) during the day at M1 (2110 m a.s.l.) averaged over the period from 1983 to 2008.

such as the Morteratsch glacier. This will result in a glacier heat flux that will be positive on average, since the snow and surface temperature is always equal or lower than the temperature at ten meters below snow/ice interface. The most pronounced peaks in the glacier heat flux are found at the beginning and end of the accumulation season. These mainly positive peaks are most likely caused by refreezing, which can produce strong temperature gradients near the surface.

Figure 4.9 shows the mean daily variations in the surface energy fluxes (a), the surface temperature and the mass balance rate (b). It can be seen that all the energy fluxes, except the net shortwave radiation, have a minimum during the day, while during the night they are approximately constant. The minima during daytime are a result of rising surface temperatures, caused by the positive shortwave budget. Higher surface temperatures will result in a large outgoing longwave flux, a stronger downward directed subsurface heat flux and on average a smaller temperature deficit between the atmosphere and the surface, resulting in weaker turbulent fluxes. The timing of the minimum in the glacier heat flux is determined by the rate of increase of the surface temperature by solar heating and the conductivity of the medium, which affects the response time of the subsurface temperatures to surface temperature variations. If surface temperatures increase more rapidly than subsurface temperatures, then the subsurface heat flux will become more negative. On the other hand, if surface temperatures increase less rapidly than subsurface temperatures, then the glacier heat flux will become less negative.

The surface temperature and mass balance rate in figure 4.9(b) both show a pronounced peak around noon. They are strongly anti-correlated, since the mass balance rate is mainly determined by the amount of melting which requires the surface temperature to be at melting point. It is remarkable to see that the mass balance rate in the evening is significantly larger than the mass balance rate in the early morning, which is mainly a consequence of more frequent snow fall during the evening, as shown in figure 4.10 for station M1. Note that especially the rainfall curve shows a pronounced peak around midnight, which is most likely a consequence of more frequent convective rainfall in summer during the evening.

Figure 4.11 shows scatterplots of the (daily mean) modeled versus the measured shortwave and longwave fluxes. The computed incoming shortwave ra-

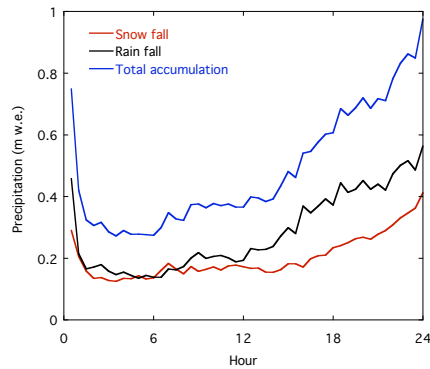


Fig. 4.10: Modeled mean diurnal pattern of the snow fall (red), rain fall (black) and total accumulation (blue) at M1 (2110 m a.s.l.) over the period from 1983 to 2008.

diation agrees rather well with the observations. However, for large fluxes the model tends to slightly overestimate the incoming shortwave radiation. For the outgoing shortwave radiation, the overestimation of the computed values is somewhat more pronounced. The fact that the shortwave fluxes are depending on several factors, makes it difficult to explain discrepancies between the calculated and observed solar radiation. Nevertheless, the overestimation of the reflected shortwave radiation, especially for larger values, is most likely related to an overestimation of the albedo of melting snow in the model. Furthermore, uncertainties related to the cloud cover, orientation of the grid cell, tilt of the mast, albedo of the grid cell, albedo of the surrounding terrain, the atmospheric transmissivity and accuracy of the measurement devices can all have a significant impact on the computed and measured shortwave fluxes. On average, the net shortwave radiation is underestimated by 2.4 W m^{-2} (table 4.3).

The scatterplot of the incoming longwave radiation shows that, despite the large spread due to uncertainties in the cloud cover, the mean measured and modeled values agree reasonably well, which is not very surprising, since the parameters ϵ_{cl} and b in equation (3.21) have been calibrated with observations done on the glacier in 1999 by Klok and Oerlemans (2002). On the other hand, the computed outgoing longwave fluxes are significantly lower than measured values. The net longwave radiation is therefore overestimated by 6.2 W m^{-2} (table 4.3), mainly as a result of the underestimation of the outgoing longwave fluxes. The outgoing longwave radiation is underestimated by 7.2 W m^{-2} , which corresponds to a mean underestimation of the surface temperature of $1.7 \text{ }^\circ\text{C}$. For comparison, Klok and Oerlemans (2002) underestimated the surface temperature by $1.8 \text{ }^\circ\text{C}$.

In the model, the outgoing longwave radiation is formulated as a function of the surface temperature, which is determined internally by solving the energy balance equation (equation (3.2)). This implies that the underestimation of the surface temperature is the result of uncertainties in the full set of formulations that determine the energy budget. In section 4.1, it was shown that the surface temperature is strongly affected by the amplitude of the turbulent fluxes. It is therefore very well possible that the calculated turbulent fluxes are currently underestimated. A comparison of the computed turbulent fluxes to observations would provide more information on this issue. The glacier heat flux is most

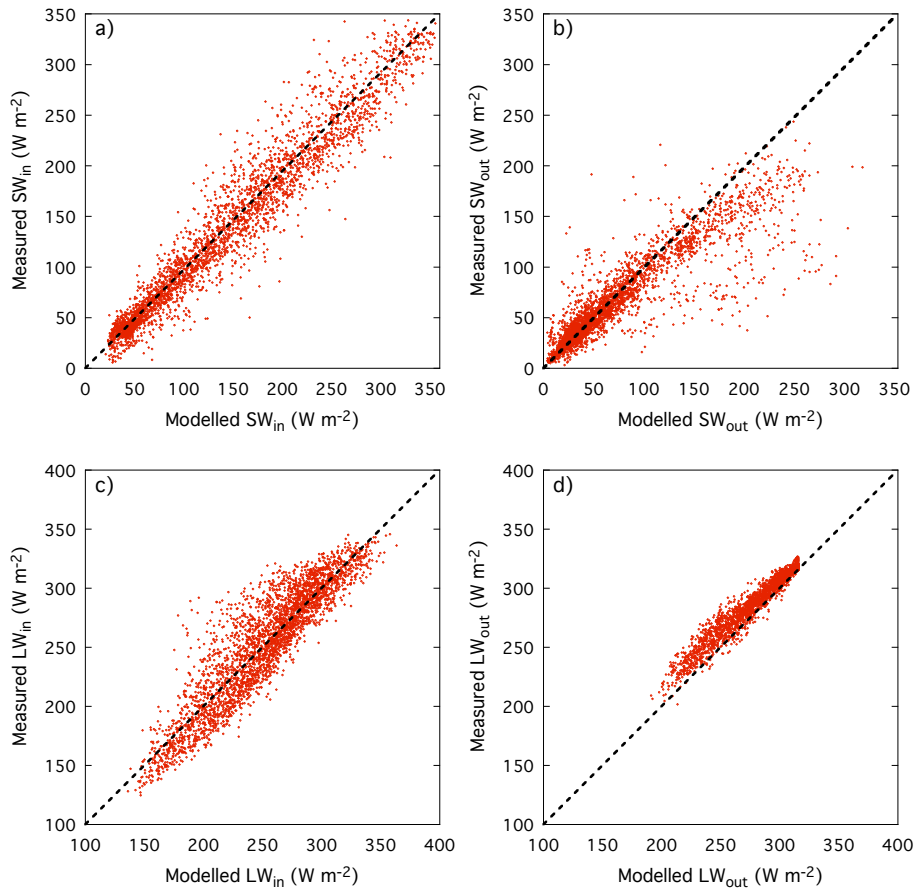


Fig. 4.11: Scatterplots of modeled versus measured daily mean incoming shortwave radiation (a), outgoing shortwave radiation (b), incoming longwave radiation (c) and outgoing longwave radiation (d) for the period from 8 July 1998 to 15 May 2007.

likely not responsible for the underestimation of the surface temperature, since the sensitivity of the surface temperature to perturbations of the subsurface parameters is found to be small (section 4.1).

Relative surface height

Figure 4.12 shows the relative surface height as a function of time for the five stake measurement sites (M1-M5). At station M1 (figure 4.12(a)), observations and modeled values agree very well. This is partly due to the availability of data of multiple variables at M1, which enables more extensive tuning with the model parameters. Over the last few years (2005 to 2008) the model tends to slightly overestimate the amount of melting. Note that the albedo of ice in the model is based on measurements of the shortwave fluxes at M1. Therefore, deviations between the modeled and measured amount of ice melt are most likely a consequence of inaccurate simulation of specific events (precipitation) or the length of the ablation season. Taking an ice albedo which is constant in

4.2. COMPONENTS OF THE MASS AND ENERGY BALANCE

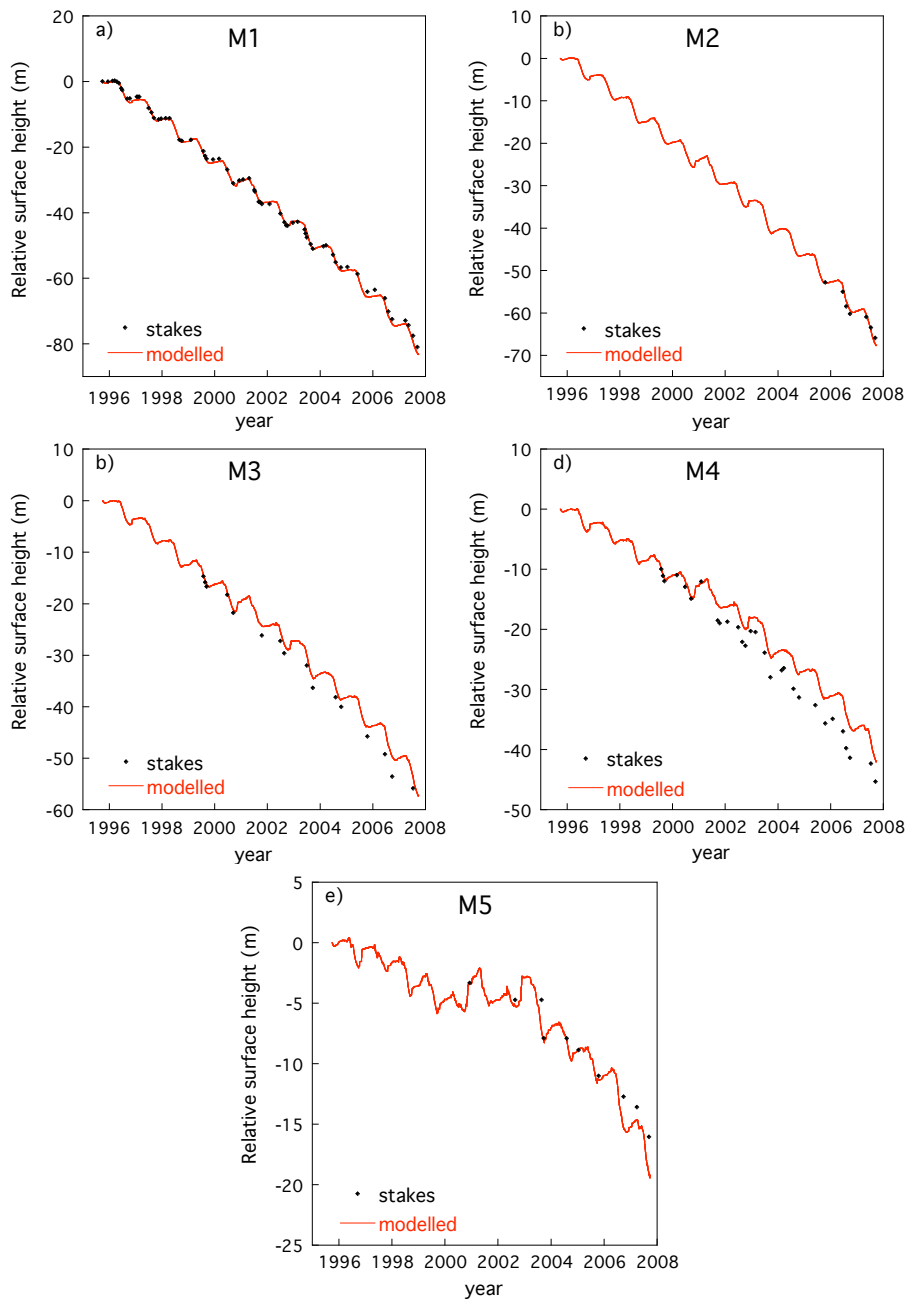


Fig. 4.12: Modeled and measured relative surface height at M1 (2110 m a.s.l.) (a), M2 (2270 m a.s.l.) (b), M3 (2500 m a.s.l.) (c), M4 (2700 m a.s.l.) (d) and M5 (2910 m a.s.l.) (e).

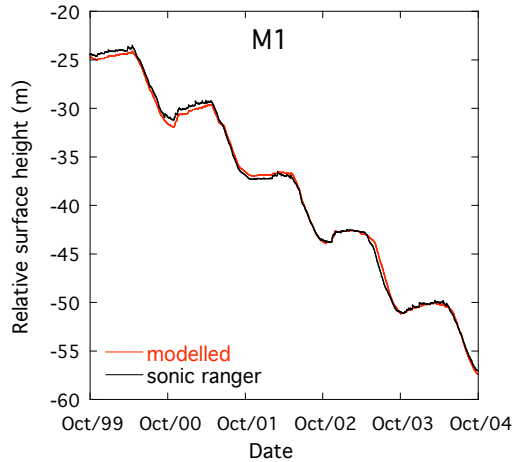


Fig. 4.13: Comparison of the modeled relative surface height to observations with the sonic ranger at M1 (2110 m a.s.l.).

time would lead to a large underestimation of the relative surface height, as will be discussed in section 4.4.

At station M2 (figure 4.12(b)), the relative surface height is only measured since 2005. Thereafter, the simulated relative surface height is in good accordance with observations. At M3 (figure 4.12(c)), the pattern of the relative surface height agrees rather well with the observations. However, during certain years (2001 and 2006) the amount of melting is underestimated by the model, leading to a maximum deviation in the relative surface height of 3.7 m at the end of the year 2006. At M4 (figure 4.12(d)), the model also predicts more melt than is observed (note the difference in axis scaling between the figures). Simulated relative surface heights at M5 (figure 4.12(e)) are in rather good agreement with measurements.

In figure 4.13, the modeled relative surface height is compared to the observed surface height, measured with a sonic ranger at M1. Generally, the time-series agree very well, since the major observed accumulation and melting events are also represented in the model results. The striking resemblance between the two curves clearly demonstrates the ability of the model to simulate mass balance variations on very short time-scales.

From the parameter sensitivity experiments (section 4.1), it can be concluded that the height dependence of the mass balance (and thus the relative surface height) can to a certain extent be calibrated with the tuning parameters (C_b , α_{ice} , γ_p and $T_{s/r}$). This resulted in a relatively good agreement of the evolution of the relative surface height at the lowest (M1) and highest (M5) measurement sites. However, at other stations (M3 and M4), the observed relative surface height is not always very well reproduced.

These local deviations of the relative surface height are mainly caused by uncertainties in the computed net shortwave radiation, e.g. by wrongly estimating the surface albedo or surface orientation. Station M4 is known to be located rather close to a side moraine, which could lead to more significant darkening of the ice during the ablation season (Oerlemans *et al.*, 2009). Other processes that could have affected the relative surface height are snow drift by wind or

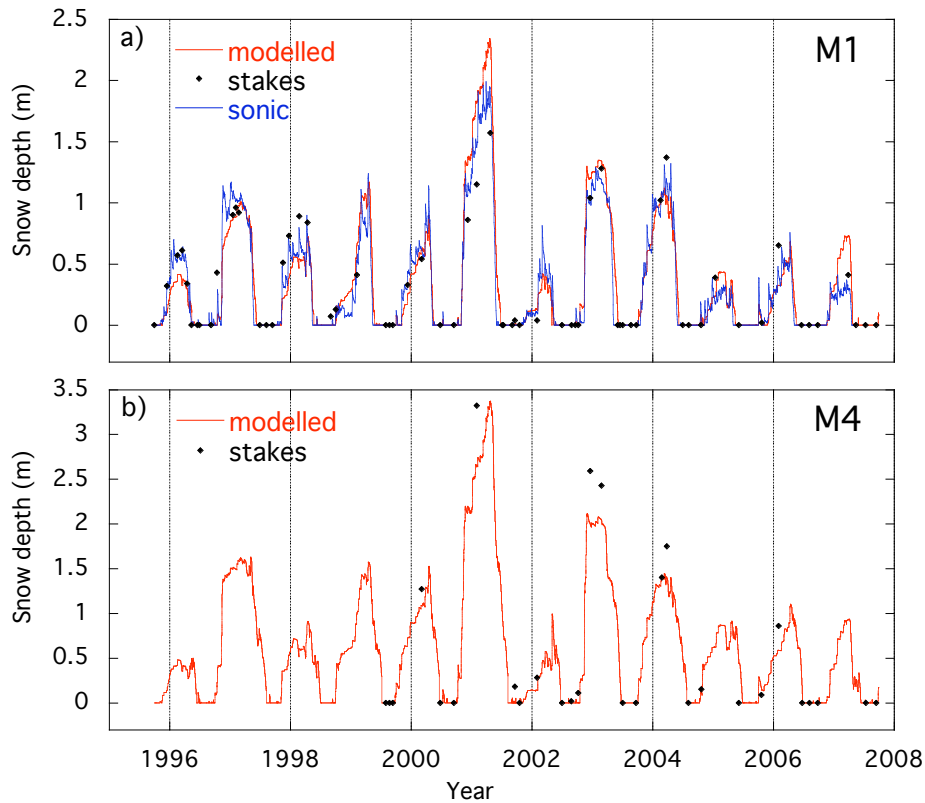


Fig. 4.14: Modeled and measured snow depth at M1 (2110 m a.s.l.) and M4 (2700 m a.s.l.). Measurements were done with stakes (M1 & M4) and a sonic ranger (M1).

avalanches, which may transport significant amounts of mass. More detailed information on the wind pattern on the glacier and the grain size of the snow could provide more insight in the significance of wind-driven snow drift on the mass balance. Also keep in mind that the measurement sites are allowed to move freely with the glacier before being displaced to their initial position. The mean velocity of the ice flow at the surface is about 10 to 20 meters per year. This will result in variations in the location of the stakes, which are not considered in the model. GPS data at the measurement sites in order to track the location of the stations can be used to allow for dynamic positioning of the stations in the model.

Snow accumulation

The evolution of the modeled and measured snow depth at stations M1 and M4 is depicted in figure 4.14. Measurements at M1 (sonic ranger and stakes) started in 1995 and the modeled snow depth seems to agree rather well with these observations. Note that the differences between the stake readings and the surface height measurements by the sonic ranger are generally small, but they can be quite significant for some of the data points. The computed snow depth is tuned with the parameters β (gravitational densification rate factor)

and ρ_{frsnow} (fresh snow density) in order to minimize deviations in the snow properties between the results and observations at M1. With the standard model set-up, the snow depth is underestimated by 1.7 cm on average when computed values are compared to stake measurements (table 4.3).

The majority of the large snow fall events is reasonably well reproduced by the model, as can be seen by comparing the modeled snow depth with observations by the sonic ranger (figure 4.14(a)). The largest differences are found in the amplitude of the small peaks (during the year), which is related to errors in the calculation of the amount of snow accumulation during a single snow fall event.

The modeled start of the accumulation season (first snow fall) coincides in most cases rather well with the observed start. However, the model tends to slightly overestimate the length of the period with a snow cover, which is probably caused by an underestimation of the albedo of melting snow (figure 4.8). Expressing the albedo as a function of accumulated maximum temperatures since the last snow fall event will most likely result in a better estimate of the albedo of melting snow (Brock *et al.*, 2000; Winther, 1993). Furthermore, including the effect of melt water accumulation in the albedo formulation, would also lead to a better estimate of the albedo of melting snow (Greuell, 2000).

At M4 (figure 4.14(b)), stake measurements are rather scarce. The measured values are on average somewhat larger than the simulated snow depths. Many processes, like wind-driven snow drift, avalanches and the height dependence of the precipitation, can have a large impact on the snow depth. In the model, the amount of precipitation increases linearly with height (250 mm per km). One might suggest to increase this gradient (γ_p) in order to achieve a thicker snow pack at M4. This would indeed lead to a better agreement between measured and modeled snow depth at M4. However, increasing γ_p will also result in a more positive mass balance with height, which is not in accordance with observations. Therefore, the precipitation gradient has not been used to tune the snow depth, since calibrating the mass balance is our main priority.

Figure 4.15 shows the observed and calculated snow density (a) and snow mass (b) at M1. On average the snow density is underestimated by 30 kg m^{-3} and the snow mass is underestimated by 0.03 m w.e. (table 4.3). The fresh snow density and the densification rate are the factors that control the evolution of the snow density. The densification rate can to a certain extent be controlled with the parameter β , while the fresh snow density (ρ_{frsnow}) is a model parameter itself. ρ_{frsnow} is set at 230 kg m^{-3} , which is very likely an overestimation of the real fresh snow density, as explained in section 3.2.3. The scarceness of the density measurements creates difficulties in assessing the quality of the modeled densification rate. Snow density measurements with a higher time resolution might avoid this problem. Recall that the influence of ρ_{frsnow} and β on the mass balance is very small (table 4.1). The snow mass (figure 4.15(b)) is not affected by the densification of the snow pack, and is therefore fully determined by the amount of precipitation, melting and refreezing.

Model input

As a quality check of the estimated input variables on the grid, model input is compared to observed weather conditions on the glacier with the mast. In the model, all the input variables are derived from measurements at the surrounding

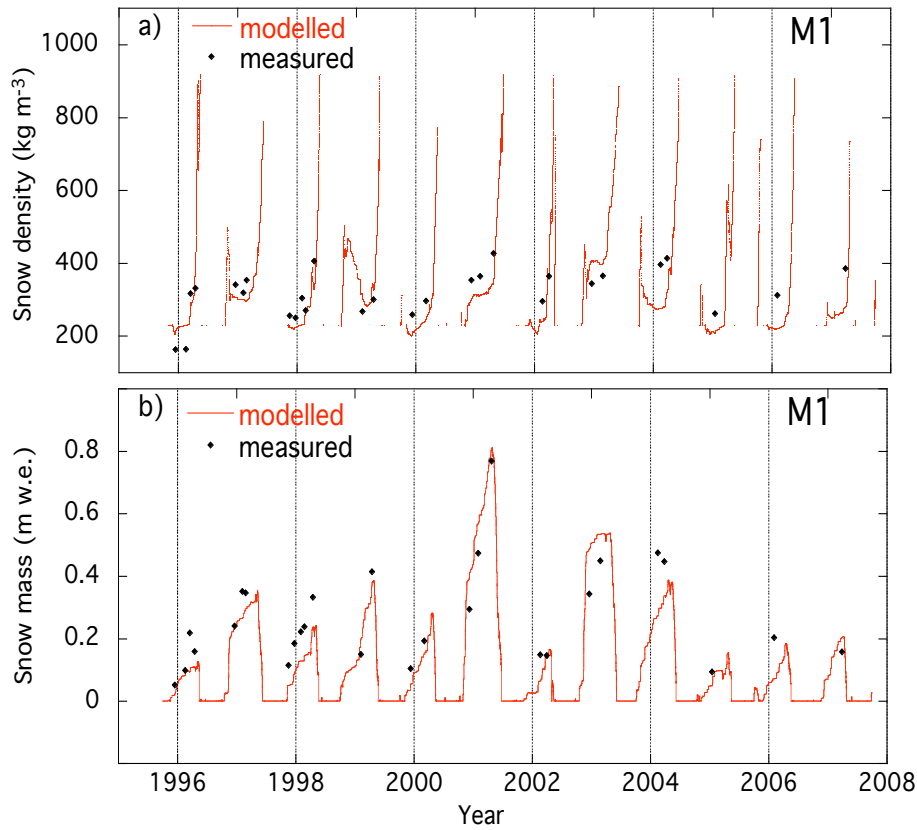


Fig. 4.15: Modeled and measured mean snow density (a) and snow mass (b) at M1 (2110 m a.s.l.).

stations and are used to force the model, as described in section 2.3.3. Figure 4.16 shows scatterplots of the daily mean modeled and measured air pressure (a), relative humidity (b), cloud fraction (c) and atmospheric temperature (d) at M1.

The air pressure estimates agree very well with the measured values on the glacier at M1. The average deviation of the daily mean values is only 0.5 hPa (table 4.3). The input values for the relative humidity are overestimated by on average 11.8%. The large discrepancy between the measured and modeled values is a result of uncertainties associated with the conversion of measured values at Corvatsch and Samedan to values on the glacier grid. The calculated cloud fraction agrees on average rather well with the values derived from observations at M1 (section 2.3.3). However, as can be seen in figure 4.16(c), the spread in the scatterplot of the daily mean cloud fraction is very large. Cloud cover estimates are smoothed by applying a 24-hour running mean to the original cloud cover estimates. Without this averaging, the spread in the scatterplot would be significantly larger. Note that the averaging procedure leads to input values that are on average closer to the mean modeled cloud fraction of 52%. Modeled atmospheric temperatures agree reasonably well with observed values, although low temperatures are slightly underestimated by the model. The deviation of

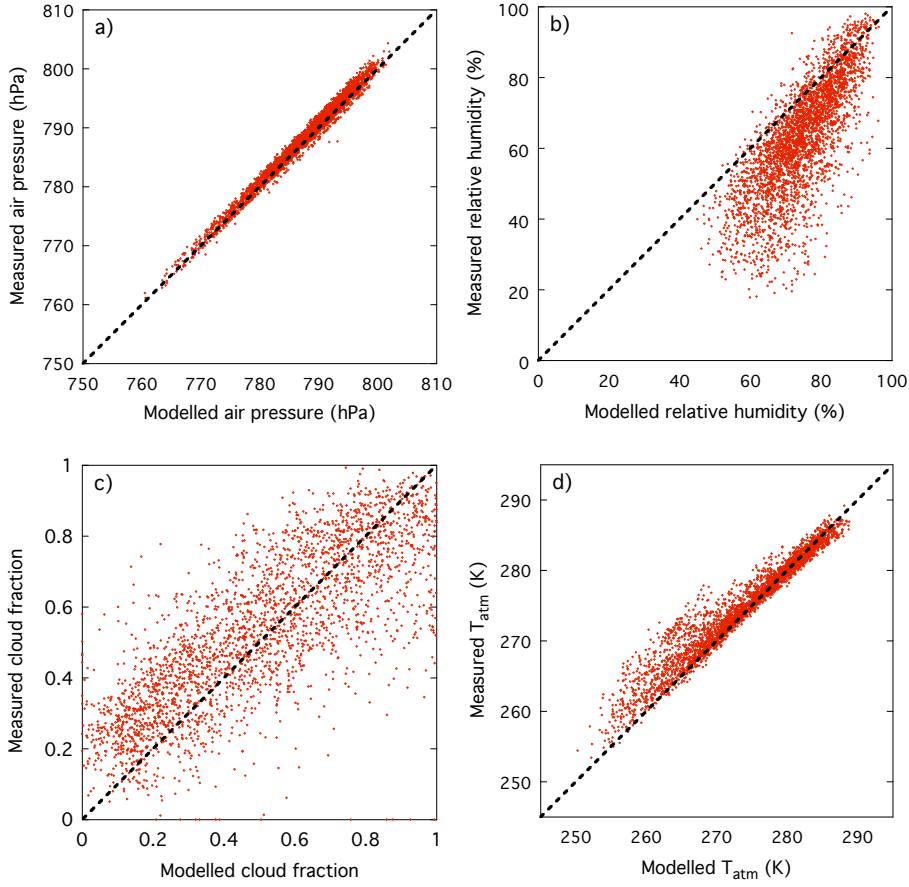


Fig. 4.16: Modeled versus measured daily mean air pressure (a), relative humidity (b), cloud fraction (c) and atmospheric temperature (d) at M1 (2110 m a.s.l.) from 8 July 1998 to 15 May 2007

the mean values is 1.14° , associated with a mean underestimation of modeled atmospheric temperature estimates at M1. Recall that the magnitude of the incoming longwave radiation, which is depending on the atmospheric temperature, is tuned to observations at M1 by Klok and Oerlemans (2002) in order to determine values for the parameters ϵ_{cl} and b (equations (3.20)-(3.22)). It is very well possible that the calibrated values of ϵ_{cl} and b compensate for the underestimation of the atmospheric temperature. Therefore, the low atmospheric temperatures are most likely not responsible for the previously mentioned underestimated surface temperatures.

4.3 Subsurface variables

In this section the impact of processes acting below the surface on the mass balance is investigated. Our main interest is to assess the effect of refreezing on the subsurface temperatures and densities and to examine its influence on

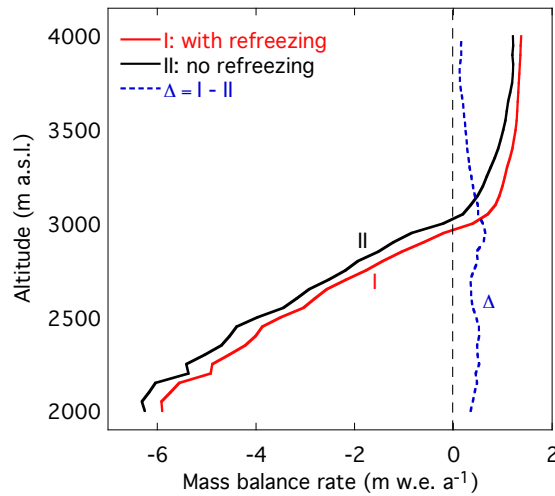


Fig. 4.17: Height profile of the mass balance rate (m w.e. a^{-1}) for a run with refreezing included (red) and a run without refreezing (black), calculated over the period from 1 October 1995 to 30 September 2000. The difference between the two runs (refreezing – no refreezing) is described by the dashed blue line.

the mass balance. In previous studies on the mass balance of the Morteratsch glacier, simplified subsurface models were used to determine the glacier heat flux on a two-dimensional grid (Klok and Oerlemans, 2002). The coupling of a two-dimensional energy balance model to a multi-layer snow model in order to assess the impact of temperature and density variations below the surface on the mass balance is new for this glacier.

Figure 4.17 presents the mean yearly mass balance for a run with refreezing of melt and rain water included and for a run with refreezing set to zero. Over the entire glacier, refreezing will add mass to the surface mass balance. Clearly, the effect of mass addition by refreezing is more important than the increased melting by a more positive glacier heat flux due to increased subsurface temperatures. The contribution of refreezing to the mass balance is on one hand determined by the availability of melt water, which decreases with altitude. On the other hand, refreezing can only occur if snow is present, which is more likely at greater altitudes. From figure 4.17, it can be seen that the largest contribution to the mass balance by refreezing is found at an altitude of about 3000 m a.s.l.. Ignoring the process of melt water (and rain water) refreezing would lead to an increase of the equilibrium line of about 50 m. Furthermore, the net mass balance would decrease by $0.41 \text{ m w.e. a}^{-1}$ if refreezing of water below the surface is not taken into account. Hence, the contribution of refreezing to the mass balance corresponds to 48% of the mean snow accumulation of $0.85 \text{ m w.e. a}^{-1}$.

Figure 4.18 shows the impact of refreezing (a) and internal accumulation (b) on the spatial pattern of the mass balance. It can be seen that refreezing is mainly affecting the mass balance around the equilibrium line in the eastern part of the glacier. Refreezing is largest in relatively flat regions around the equilibrium line, since these areas receive more solar radiation. Recall that internal accumulation is a term used to describe the amount of percolating water

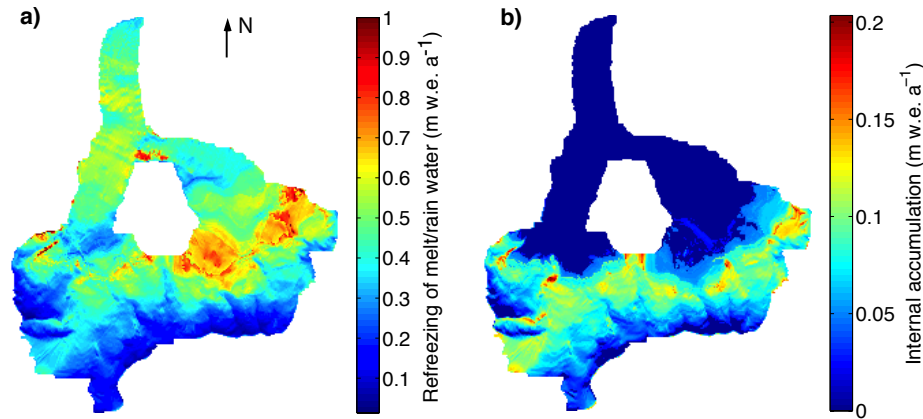


Fig. 4.18: Spatial distribution of the impact of refreezing (a) and internal accumulation (b) on the mass balance averaged over a 5-year period (1995-2000).

and irreducible water that refreezes below the summer surface of the previous year. It is interesting to assess the importance of this term, since traditional mass balance measurements do not account for this mass contribution in the accumulation zone (Schneider and Jansson, 2004). The area-averaged simulated internal accumulation is $0.04 \text{ m w.e. a}^{-1}$, which corresponds to about 3.5% of the sum of the mean accumulation by snow and refreezing. For comparison, Schneider and Jansson (2004) estimated an annual contribution 0.04 to 0.06 m w.e. , corresponding to 3 to 5% of the annual accumulation for Storglaciären, Sweden. Furthermore, Reijmer and Hock (2008) found a contribution of internal accumulation of 0.25 m w.e. , which amounted to about 20% of the winter balance. Note that internal accumulation can only occur in the accumulation zone, since the previous year's summer surface in the ablation zone is an impermeable ice layer, which disables vertical transport and refreezing of melt/rain water. Internal accumulation is largest in regions just above the equilibrium line, since surface melting is more significant in this region than at higher altitudes. Furthermore, snow accumulation decreases with altitude, which causes the summer surface of the previous year to be closer to the glacier surface and therefore favors the penetration of percolating water through the previous year's summer surface.

The mean subsurface temperatures and densities at certain depths are given as a function of altitude in figure 4.19. Lowest mean subglacial temperatures are found at the surface, which is typical for a temperate glacier. Close to the surface, the temperature of the medium is affected by the atmospheric temperature by means of the subsurface heat flux. Figure 4.19(a) also shows that subsurface temperatures decrease with altitude, which is a consequence of the negative mean atmospheric temperature gradient with altitude. Note that a remarkable bump in the subsurface temperature is found at a depth of 2 m below the surface in the accumulation zone. Refreezing of melt- and rain water is an important source of energy, even at 2 m below the surface in the accumulation zone. However, in the ablation zone, ice is usually found at a depth of 2 m below the surface, which disables the possibility of refreezing. Without refreezing in the model, all the temperature profiles would show a gradual decrease with

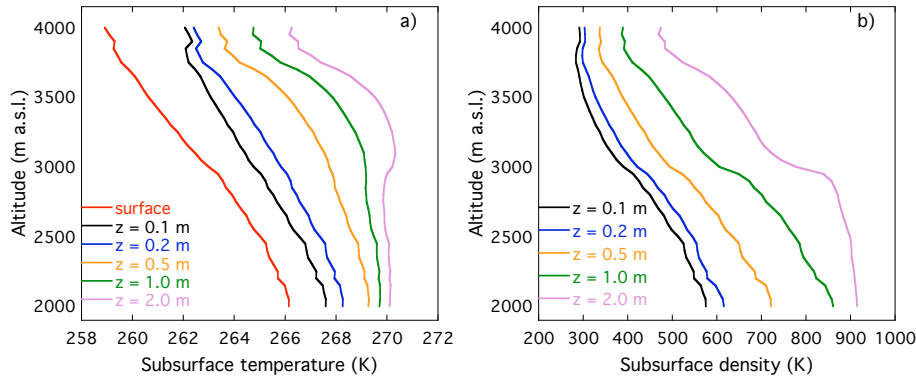


Fig. 4.19: Height profile of mean subsurface temperatures (a) and densities (b) at certain depths below the surface averaged over the 25-year period (1983-2008).

altitude.

The subsurface density profile at different depths (figure 4.19(b)) also shows a decrease with altitude. A notable drop in the density profiles is found around 3000 m a.s.l.. Above this altitude snow is present throughout the year, while below this height, the snow pack vanishes during the ablation season. At a depth of 2 m below the surface, the density is approximately equal to the density of ice, since a snow thickness larger than 2 m is quite exceptional in the ablation zone. The impact of refreezing on the density is less pronounced than the effect on the subsurface temperatures. Gravitational densification becomes more significant at higher temperatures (see figure 3.4) and is therefore more pronounced in the lower regions. This gravitational packing is mainly responsible for the increase of the density with depth, since older snow has had more time to settle.

The water content of the firn layer comprises slush water and irreducible water. In figure 4.20, the water content at M1 is plotted as a function of time for a 50-day period in the spring of 1999. Irreducible water is stored in a layer if the available amount of water exceeds the amount of water which can be refrozen. Recall that refreezing is limited by either the temperature of the layer, the density of the layer or the availability of water, as described in section 3.1.2. The irreducible water content of a layer can only decrease by refreezing or densification of the layer. Refreezing of irreducible water mainly occurs after surface cooling during the night, which explains the daily minima in the pattern of the irreducible water content. Once all the subsurface layers contain the maximum amount of irreducible water (equation 3.32), the melt water will reach the impermeable ice and a slush layer is formed. Slush water will leave the layer by (subsurface) runoff or refreezing, resulting in a drop of the slush water content during the night. As the snow pack becomes thinner and melt water keeps refreezing, the density of the firn layer may finally reach the density of ice to form a superimposed ice layer. During the last 10 days in figure 4.20 ice melt initiates and all the melt water runs off instantly.

Figure 4.21 displays the densification of the snow pack by the processes of gravitational packing (a), refreezing of percolating water (b) and vapor transport (c). Also the snow temperature is given since densification is strongly dependent on this temperature. Conversely, the snow temperature itself is also strongly

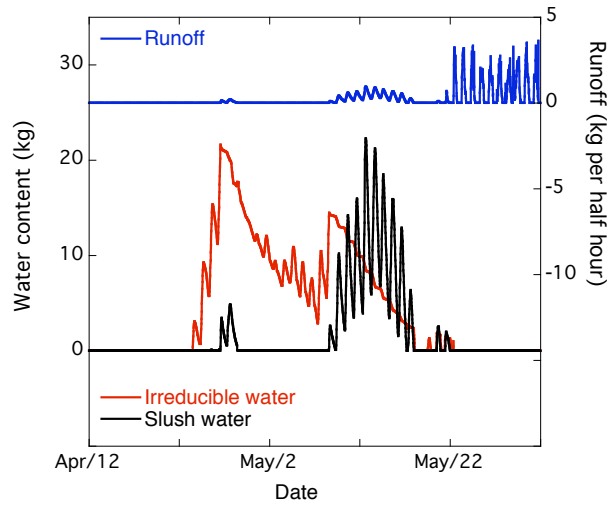


Fig. 4.20: The total amount of irreducible water (red) and slush water (black) stored in the snow pack during a 50-day period in 1999. The amount of runoff (kg per half hour) is given in blue.

influenced by the densification rate in case of refreezing.

Figure 4.21(a) shows that the patterns of the gravitational densification and the snow temperature are strongly correlated. Settling of the snow becomes increasingly important for higher snow temperatures, which is illustrated by the rapid increase of the densification after April 22, and by the pronounced daily cycle in the densification with lowest rates during the nights. The gravitational packing rate of the snow also depends on the difference between the snow density and the density of ice. As the density keeps increasing, this difference becomes smaller and consequently the gravitational densification rate will decrease gradually, as can be seen clearly after April 24.

The densification by refreezing of melt and rain water is depicted in figure 4.21(b). The first three peaks in the densification rate are related to direct refreezing of percolating melt water and are mainly responsible for the rapid rise of the mean snow temperature to melting point. If a slush layer is present (figure 4.20), refreezing of this slush water will occur (mainly) during the nights, which explains the peaks at May 9-11. In absence of slush water, irreducible water may refreeze. The peaks from May 4 to May 8 are most likely caused by refreezing of this irreducible water.

Figure 4.21(c) displays the densification of the snowpack due to vapor transport through the surface. Vapor transport will also take place between successive subsurface layers, however, these fluxes only transport mass from one layer to another without changing the total mass of the snowpack. The vapor transport at the interface between the bottom of the snowpack and the impermeable ice is assumed to be zero. Therefore, densification by vapor fluxes can only occur by means of mass exchange through the surface interface. The direction and magnitude of the vapor fluxes is depending on the vertical temperature gradient (equation (3.46)). The total densification of the snowpack is therefore depending on the temperature difference between the surface and the first subsurface layer.

4.3. SUBSURFACE VARIABLES

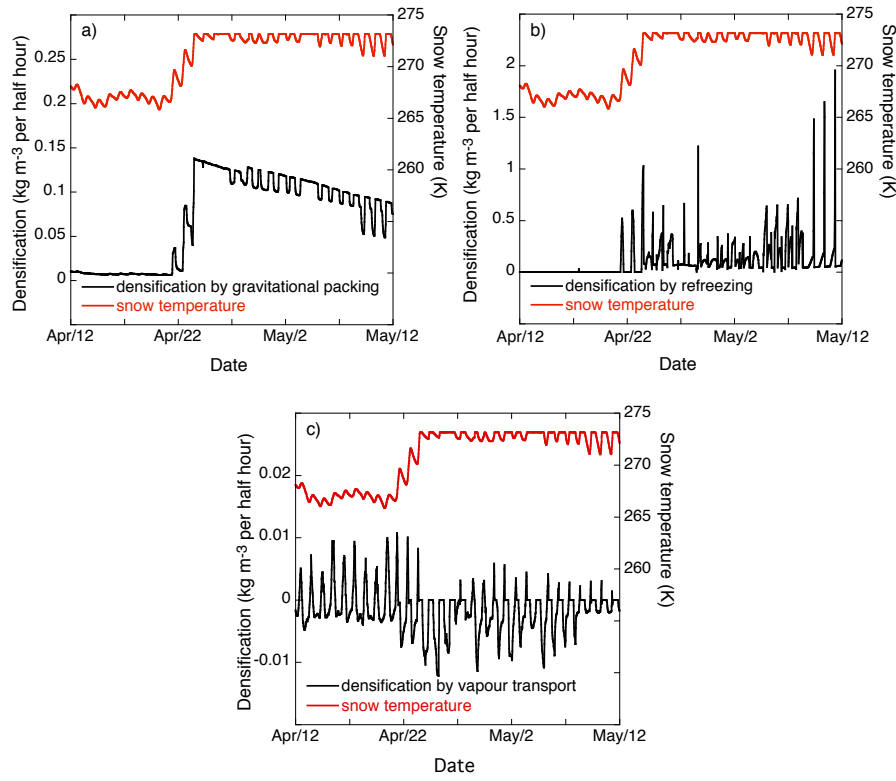


Fig. 4.21: The gravitational densification (a), densification by refreezing (b) and the densification by vapor transport through the surface (c) as a function of time for a 30-day period in 1999 at station M1. The mean snow temperature for this period is given in red.

The densification by vapor transport is on average negative, since the surface temperature is generally lower than the temperature of the first subsurface layer (figure 4.19(a)). Figure 4.21(c) shows a pronounced daily pattern in the vapor densification rate, with negative values during the night as a result of surface cooling and positive peaks during the day after heating of the surface. The response time of the vertical snow temperature profile to changes in the surface energy budget increases rapidly with depth, resulting in a temperature gradient between the surface and the first subsurface layer. Once the temperature of the entire snow pack is raised to 0 °C, then the densification by vapor transport cannot attain values greater than zero anymore, since the surface temperature is always equal or smaller than the subsurface temperatures.

Recall that both refreezing and vapor fluxes contribute to the total mass of the snowpack, while settling of the snow only affects the snow density and snow depth. The mean impact of refreezing on the total densification is of approximately similar magnitude as the impact of gravitational densification. On the other hand, the effect of densification by vapor transport on the total densification is about 20 times smaller.

The vertical profiles of the daily mean subsurface temperatures during a one-year period are presented in figure 4.22. The chosen period from 1 October

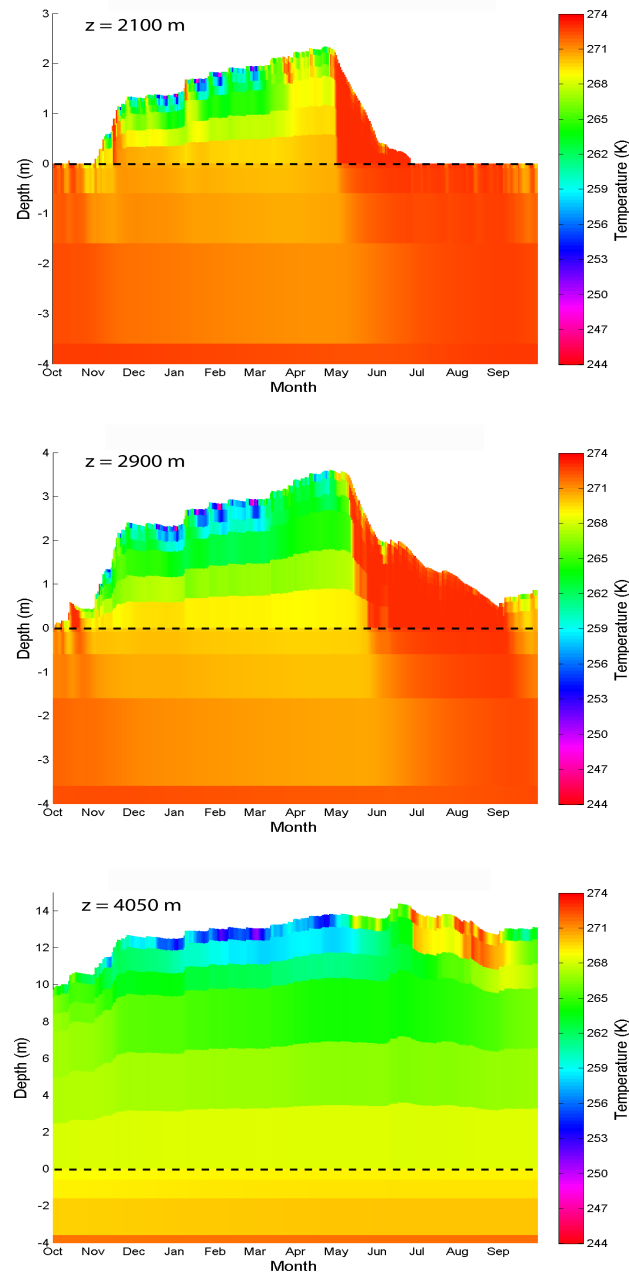


Fig. 4.22: Daily mean subsurface temperatures at certain depths as a function of time for the period from 1 October 2000 to 30 September 2001. The snow / ice interface is located at a depth of 0 m (dashed black line). The temperature profiles are given at 2100 m a.s.l., 2900 m a.s.l. and at 4050 m a.s.l..

4.3. SUBSURFACE VARIABLES

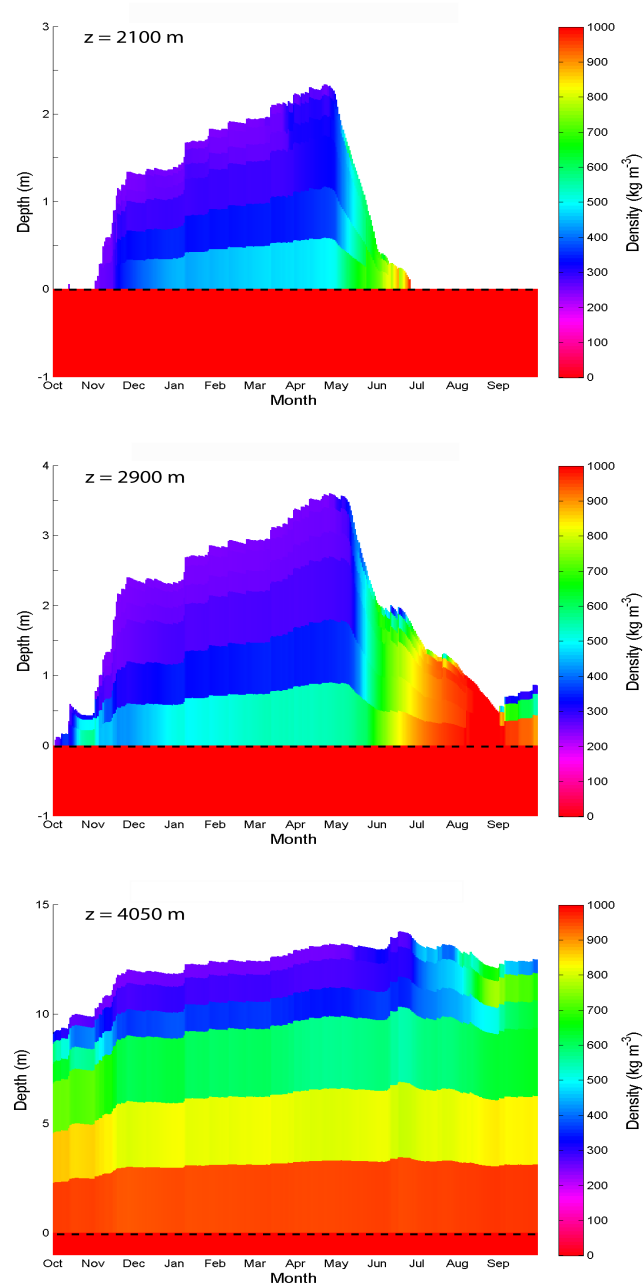


Fig. 4.23: Daily mean subsurface densities at certain depths as a function of time for the period from 1 October 2000 to 30 September 2001. The snow / ice interface is located at a depth of 0 m (dashed black line). The density profiles are given at 2100 m a.s.l., 2900 m a.s.l. and at 4050 m a.s.l..

2000 to 30 September 2001 is characterized by an exceptionally large amount of snow accumulation. This extensive snow fall resulted in a positive specific mass balance at 2900 m a.s.l. and a maximum snow depth at the tongue of more than 2 m. As we have shown before, the year 2001 was the only mass balance year since 1983 with a positive net mass balance.

At an altitude of 2100 m a.s.l. the grid cell is covered by snow from the beginning of November until the end of June. During the winter months, surface temperatures drop to very low values during cold periods. The response time of the subsurface temperatures to these lower surface temperatures is depending on the distance to the surface. At depths greater than 2 m below the surface, subsurface temperatures respond very slowly (on the order of weeks or longer) to surface temperature variations, and only a seasonal cycle is found in the subsurface temperatures. Note that a melting and refreezing event occurred at 2100 m a.s.l. in January, which significantly increased subsurface temperatures for a few weeks. At the end of April, the snow pack starts to melt and refreezing adds mass and heat to the snow layers. By the end of June, the snow pack has vanished and ice melt starts. Temperatures at and just below the surface are on average lower than subsurface temperatures at greater depths leading to a positive mean glacier heat flux. However, heating by refreezing and the lagging response of the subsurface temperatures to surface heating may lead to a temporary negative glacier heat flux. Recall that no heat is transported downwards at a depth of 10 m below the snow/ice interface (temperature set at 0 °C, thereby disabling the possibility of a mean negative glacier heat flux.

At an altitude of 2900 m a.s.l., snow is present during the entire year, which is unusual, since the equilibrium line is located at a height of about 3000 m a.s.l.. Subsurface temperatures are somewhat lower than at the glacier tongue. However, during the summer months, refreezing raises the temperature of the entire snow pack to melting point. It takes until the beginning of September, before all the water in the firn layer has been refrozen, and subsurface temperatures can drop below melting point again.

Even at a height of 4050 m a.s.l., some melting occurs during the summer months, heating the upper snow layers. The deeper layers are hardly affected by surface temperature variations.

The subsurface density profiles in figure 4.23 are strongly related to the subsurface temperatures in figure 4.22, since the gravitational densification rate is mainly depending on the temperature of the layer. Gravitational packing of the snow decreases the snow depth and is largest in layers with a higher temperature. Snow fall events add mass with a low density to the surface and therefore decrease the mean density of the snow pack. On the other hand, refreezing adds mass to the interior of the snow pack and therefore increases the mean snow density. Note that it takes much more time to raise the density by refreezing to the density of ice than to raise the snow temperature to melting point. At 4050 m a.s.l., densities are steadily increasing with depth. Large vertical gradients in the snow density are found as a result of the limited amount of snow layers in the model. A clear increase of the snow density with depth is seen since older snow has had more time to settle. Furthermore, the increasing temperatures with depth result in a higher densification rate of the deeper layers. Despite the low air temperatures and the limited amount of melting at 4050 m a.s.l., refreezing of melt water takes place up to several meters below the surface. Note that the firn density at an altitude of 2900 m a.s.l. is raised to the density

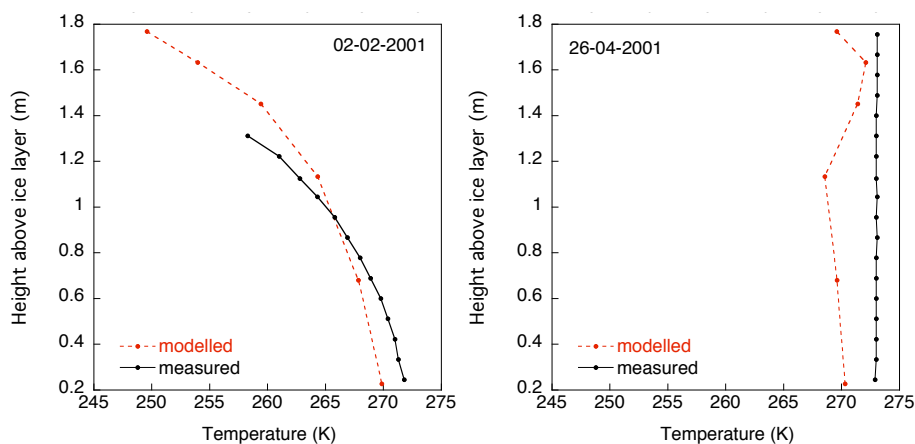


Fig. 4.24: Simulated (red) and measured (black) subsurface temperatures at M1 on 2 February 2001 (left) and 26 April 2001 (right).

of ice to form a super-imposed ice layer on top of the impermeable ice which is exposed at the surface in August. In September fresh snow starts accumulating on top of the super-imposed ice.

In figure 4.24, two subsurface temperature profiles are compared to observations at M1. At 2 February 2001 (left panel), the modeled snow depth is larger than the measured thickness of the snowpack. The simulated shape of the temperature profile seems to agree rather well with the shape of the observed profile. However, if we compare measured and modeled temperatures at equal distances to the surface, then the model strongly underestimates the snow temperatures. The modeled snow temperature profile at 26 April 2001 (right panel) again underestimates the subsurface temperatures significantly. The measured profile is at melting point throughout the snow pack, while melt water refreezing in the model was insufficient to heat the entire snow pack to $0\text{ }^{\circ}\text{C}$ by that time, which is the result of underestimated surface temperatures.

Modeled mean subsurface temperatures at M1 are on average $3.7\text{ }^{\circ}\text{C}$ lower than measured values. As mentioned before, the mean surface temperature is underestimated by $1.7\text{ }^{\circ}\text{C}$. However, surface temperatures in summer are generally not much lower than observed values, since the snow pack is at melting point most of the time. So the low mean surface temperature is mainly a consequence of underestimated surface temperatures in the winter season. Furthermore, subsurface temperatures are all measured when a snow pack is still present. Most likely, the discrepancies between the modeled and measured snow temperatures can be fully ascribed to an underestimation of the surface temperature.

4.4 Additional simulations

We performed some additional runs in order to study the effect of a changing ice albedo on the mass balance (section 4.4.1). Furthermore, the effect of incorporating a snow model has been investigated by applying the parameter set-up, proposed by Klok and Oerlemans (2002), to our model (section 4.4.2).

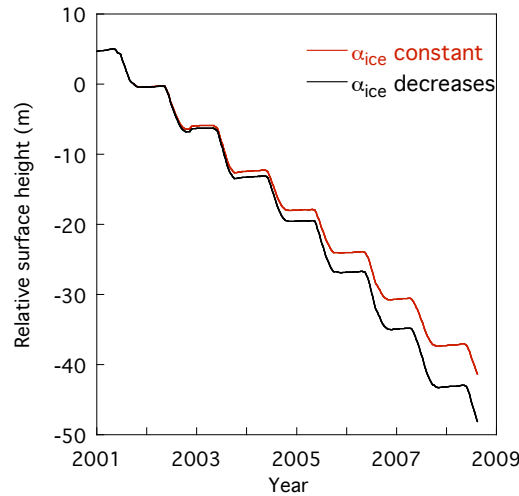


Fig. 4.25: Relative surface height at M1 for the period 2001 to 2008 for a run with a constant ice albedo (red) and a run with a decreasing albedo of ice after 2001 (black), based on measurements at M1.

4.4.1 Effect of a changing ice albedo

Debris deposition on the ice is known to have a major impact on the mass budget. Figure 4.25 illustrates this effect by showing the computed relative surface height at M1 for a simulation with a constant albedo and a run with a decreasing albedo since 2002 (with values calibrated with observations). It can be seen that at the start of 2008, the difference between the relative surface heights is already 5.9 m. This effect is comparable to the impact of a 1.4 °C temperature rise on the relative surface height. For comparison, Oerlemans *et al.* (2009) concluded that a 1.7 °C temperature increase would have a similar impact on the ablation as the decreasing ice albedo for the period 2003-2006. Note that α_{ice} has a significant impact on the summer mass balance, while the winter balance is hardly affected. Increased debris concentrations can rightfully explain the decrease of the measured albedo of ice since 2002 (Oerlemans *et al.*, 2009). However, further research is needed to study the spatial distribution of the debris concentrations in more detail. Current albedo parameterizations do not account for these variations in the debris deposition.

4.4.2 Effect of incorporating the snow model

We conclude this section by comparing the mass balance profile of two different runs: one with the standard parameter set-up of the model, and another one with the set-up proposed by Klok and Oerlemans (2002). The height profiles of the mass balance for these two runs and the mutual differences are presented in figure 4.26. Klok and Oerlemans (2002) calibrated certain parameters to match observations. However, they did not tune the mass balance itself, which was the main goal of the calibration procedure in this study. Klok and Oerlemans (2002) overestimated the mass balance with their model by 5 to 8% for the stations M1, M3 and M4. The differences in the parameter set-up adopted by Klok and Oerlemans (2002) and the set-up used in this study are given in

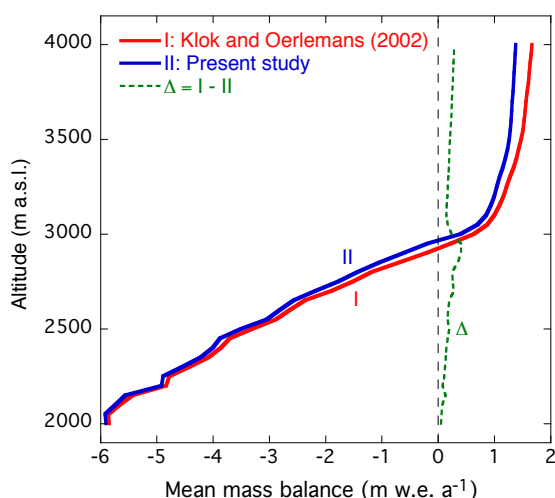


Fig. 4.26: The mean mass balance (m w.e. a^{-1}) over the period 1995-2000 for a run with the standard parameter settings of the model (blue) and a run with our model applying the parameter set-up used by Klok and Oerlemans (2002).

table 4.4. Note that certain processes which are contained in this model are not included in the model used by Klok and Oerlemans (2002). These processes, like refreezing, have a significant influence on the mass balance as shown in section 4.3. From figure 4.26, it is clear that the parameter set-up proposed by Klok and Oerlemans (2002) leads to a more positive mass balance with our model than with the standard set-up used in this study. Especially around the equilibrium line altitude, the difference is significantly large, which is mainly caused by the sensitivity of the mass balance to perturbations of γ_p and $T_{s/r}$ (figure 4.1(a)). At lower altitudes, the effect on the mass balance of the differences in the values for C_b and α_{ice} seem to oppose each other, while the differences in γ_p and $T_{s/r}$ do not have a major impact on the mass balance in this area. In the accumulation zone, the mutual difference in the mass balance can be to a large extent explained by the variations in the precipitation gradient γ_p . Running the model with the set-up proposed by Klok and Oerlemans (2002) leads to a significant overestimation of the mass balance. Note that a value for γ_p of 400 mm km^{-1} may lead to a better estimate of the snow depth at M4 (figure 4.14(b)). However, this adjustment of γ_p will deteriorate the modeled profile of the mass balance as compared to measured values and is therefore not applied. The incorporation of the snow model is the main difference between our model

Table 4.4: Comparison of the model set-up used by Klok and Oerlemans (2002) and the set-up used in this study.

Variable	This study	Klok and Oerlemans (2002)
α_{ice}	0.32	0.34
C_b	0.0032	0.0037
γ_p (m km^{-1})	0.250	0.400
$T_{s/r}$ (K)	274.4	274.5

Table 4.5: Mean mass balance sensitivity with respect to changes in air temperature (T_{atm}) and precipitation (P) over the period from 1 October 1995 to 30 September 2000. Klok and Oerlemans (2002) determined the mass balance sensitivity for the year 1999.

<i>Perturbation</i>	ΔMB (<i>m w.e. a⁻¹</i>)	<i>Klok and Oerlemans (2002)</i>
$T_{atm} + 2$ °C	-1.41	
$T_{atm} + 1$ °C	-0.68	-0.70
$T_{atm} - 1$ °C	+0.58	+0.65
$T_{atm} - 2$ °C	+1.00	
$P + 20$ %	+0.29	
$P + 10$ %	+0.15	+0.17
$P - 10$ %	-0.16	-0.16
$P - 20$ %	-0.32	

and the model used by Klok and Oerlemans (2002). It is not surprising that the set-up proposed by Klok and Oerlemans (2002) applied to our model leads to results that agree less well with observations, since Klok and Oerlemans (2002) tuned their model parameters while neglecting the effects of subsurface processes on the mass balance.

4.5 Climate sensitivity

Climate sensitivity experiments play a crucial role in the interpretation of the vulnerability of glaciers to variations in climate variables. The sensitivity of the mass balance to climatic changes is investigated by perturbing the input values of the air temperature and precipitation. The mass balance is a good indicator of climate change, since it responds directly to fluctuations in the mass and energy fluxes at the surface. On the other hand, the glacier responds to changes in the mass balance by adjusting its length as described by the linear response equation (Oerlemans, 2001). Length adjustments are not considered in this study, since the glacier geometry is kept fixed in the model.

The climate sensitivity of the mass balance is given in table 4.5 together with the values found by Klok and Oerlemans (2002). The mass balance is more sensitive to a positive temperature change than to a negative temperature change, which indicates that the mass balance response is nonlinear. The sensitivities found for the Morteratsch glacier by Klok and Oerlemans (2002) are quite similar to the values found in this study. The largest difference is found in the sensitivity after a negative temperature perturbation. Note that the results by Klok and Oerlemans (2002) are based on a 1-year simulation (1999), while we calculated the specific mass balance sensitivity over a period of 5 years (1995-2000). For comparison, Oerlemans (2000b, 2001) found a mass balance sensitivity of -0.41 m w.e. a^{-1} for both the Rhone glacier and Hintereisferner and Greuell and Böhm (1998) calculated a sensitivity of -0.90 m w.e. a^{-1} for the Pasterze after a positive change in the air temperature of 1 °C. Furthermore, Klok and Oerlemans (2004) found a mass balance sensitivity to temperature perturbations of -0.59 m w.e. a^{-1} per K and a sensitivity to precipitation perturbations of 0.17 m w.e. a^{-1} per 10%. Clearly, the mass balance variations after a change in the precipitation by 10% are much smaller than the response to a perturbation of the temperature by 1 °C. The effect of a 1 °C temperature

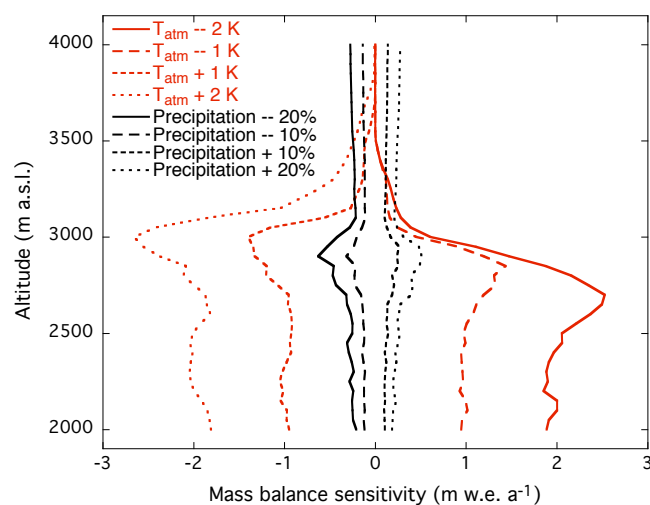


Fig. 4.27: Mass balance sensitivity to perturbations of the temperature (red) and the precipitation (black). The yearly mean mass balance sensitivity (m w.e. a^{-1}) is calculated over the period from 1 October 1995 to 30 September 2000.

rise is counteracted by a 45% increase in the amount of precipitation.

Figure 4.27 shows the sensitivity of the mass balance to climatic variations as a function of height. Air temperature sensitivities are largest in the ablation zone, since the length of the 'snow-free' period is affected by the air temperature. In the accumulation zone, atmospheric temperature perturbations have a small impact on the mass balance, since snow is present all year long. The precipitation sensitivity of the mass balance gradually increases with height in most regions, since the absolute perturbation of the amount of snowfall is larger at greater altitudes. A peak in the precipitation and air temperature sensitivity is found around 2900 m a.s.l., because the precipitation variations cause the equilibrium line to shift upward or downward, which has a major impact on the mass balance in these regions, as explained in section 4.1. Figure 4.27 also shows that the altitude of the peak in the mass balance sensitivity is dependent on the sign and magnitude of the temperature perturbation. The variations in the altitude of this peak are related to changes in the equilibrium line altitude. The previously mentioned nonlinearity in the mass balance response can be explained by this shift of the equilibrium line, since it marks the extent of the ablation zone and the mass balance is mainly sensitive to temperature variations in the area below the equilibrium line. In other words, if the extent of the ablation zone increases after a positive temperature perturbation then the net mass balance will be affected more strongly than in case of an ablation zone retaining its original size.

Chapter 5

Conclusion & discussion

A snow model has been coupled to a surface energy balance model in order to simulate the mass balance of the Morteratsch glacier for the period from 1983 to 2008. The energy balance model is developed along the lines presented by Klok and Oerlemans (2002). The snow model, based on a routine described by Greuell and Konzelmann (1994), is implemented to calculate subsurface profiles of temperature, density and water content after simulating storage, refreezing and runoff of melt and rain water below the surface. Refreezing of the available amount of water adds mass to the interior of the glacier and raises subsurface temperatures and densities, thereby affecting the amount of melt by means of the subsurface heat flux. The snow model in this study is more advanced than the simplified snow model used by Klok and Oerlemans (2002), which, most importantly, discounted the process of refreezing.

Measurements of climate variables around the glacier were used to determine the model input on the grid. Observations of melt, snow properties, radiative fluxes and climate variables on the glacier were adopted for calibration and validation of the model results. Several model parameters have been adjusted in order to match the calculated mass balance and snow properties to observations. After this tuning, the modeled and measured mass balance agreed reasonably well. Discrepancies are most likely caused by uncertainties in the albedo, wind-driven snow drift and the geographic location of the measurement sites. In the model, measurement sites on the glacier are assumed to be at a fixed geographic location. However, in reality, these stations move with the glacier and are displaced upstream to their original geographic location every 2 to 3 years. The resulting deviations are currently not accounted for by the model. Using GPS-data from the measurement sites on the glacier would allow for dynamic positioning of the stations in the model. High time-resolution observations of the wind speed and direction to study the evolution of the wind pattern would allow for more accurate simulation of processes like wind-driven snow drift.

The net mass balance from 1983 to 2007 is -0.78 m w.e. per year, with a mean altitudinal gradient of the mass balance of 0.006 m w.e. $\text{a}^{-1} \text{m}^{-1}$. Refreezing of water below the surface contributes on average 0.41 m w.e. per year to the mass balance, which corresponds to 48% of the mean snow accumulation. The major contribution of refreezing to the mass budget is found around the equilibrium line altitude. Internal accumulation below the previous year's end-of-summer surface contributes 0.04 m w.e. a^{-1} to the mass budget, which is equal to about

3.5% of the mean accumulation by refreezing and snow fall. The model by Klok and Oerlemans (2002) uses a different parameter set-up, which compensates for unconsidered effects like refreezing on the mass balance. Applying the parameter set-up by Klok and Oerlemans (2002) to the model in this study therefore leads to an overestimation of the mass balance.

Parameter sensitivity experiments show a strong sensitivity of the mass balance to perturbations in the albedo parameters. The used albedo parameterization by Oerlemans and Knap (1998) accounts for snow aging, but does not depend on the air or snow temperature or the water content, which leads to an overestimation of the albedo of melting snow. Measurements of shortwave fluxes show a clear decrease of the albedo of ice since 2002 as a result of debris deposition (Oerlemans *et al.*, 2009), which has an impact on the mass balance at the tongue, similar to the effect of a 1.4 °C temperature rise. Currently, a limited understanding of the distribution and evolution of debris concentrations on the glacier complicates accurate simulation of the ice albedo. The sensitivity of the mass balance to perturbations in the subsurface parameters is found to be small.

Climate sensitivity experiments show that an air temperature deviation of 1 °C causes a shift in the specific mass balance of about 0.63 m w.e. a⁻¹, while a deviation of the precipitation of 10% results in a change of the mass balance of about 0.16 m w.e. a⁻¹.

A discrepancy between modeled and measured outgoing longwave fluxes was found, corresponding to a mean underestimation of the surface temperature of 1.7 °C, with largest deviations during wintertime. The turbulent fluxes have a major impact on the surface temperature, especially in winter, as shown with the sensitivity experiments. Assuming that all the significant energy fluxes are contained in the model, this underestimation of the surface temperature can be to a large extent ascribed to an underestimation of turbulent transport. A comparison with eddy correlation measurements of the turbulent fluxes is needed to verify this.

Snow temperatures and densities are strongly affected by refreezing of water below the surface. The mean underestimation of the snow temperatures of 3.7 °C during the accumulation season is most likely the result of the low surface temperatures. More frequent snow temperature and density measurements are needed to validate the results of the snow model. E.g. the scarceness of these data complicates the validation of the simulated impact of refreezing on the snow temperature and density.

The cloud cover estimates, derived from insolation measurements at Corvatsch are uncertain and do not capture daily variations. A different method to improve the accuracy of the estimated cloud fraction is therefore desirable.

Water transport between neighboring grid cells is not considered by the model. Instead, a certain fraction of the slush water below the surface runs off every time-step, depending on the slope of the grid cell. Simulation of melt water tracks would help to determine the evolution of the slush water content of the grid cells more accurately. However, simulating these melt water tracks is complicated by the absence of a detailed topography of the glacier surface. Crevasses and local variations in the slope determine to a large extent the direction of the flow. Furthermore, the depth-dependence of the runoff rate is not fully understood yet.

In the future, this coupled snow and energy balance model could be applied

to other glaciers to assess the impact of subsurface processes on the mass balance. It could be useful to couple a snow model with a higher vertical resolution (more layers) to a surface energy balance model to investigate the evolution of the density, temperature and water content of the snow pack in more detail in order to gain more insight in the impact of subsurface processes, like refreezing, on the mass balance.

Bibliography

- Arnold, N., Willis, I., Sharp, M., Richards, K., and Lawson, W. (1996). A distributed surface energy-balance model for a small valley glacier. I. Development and testing for Haut Glacier d’Arolla, Valais, Switzerland. *Journal of Glaciology*, **42**(140), 77–89.
- Atwater, M. and Brown Jr, P. (1974). Numerical Calculation of the Latitudinal Variation of Solar Radiation for an Atmosphere of Varying Opacity. *J. App. Meteorol*, **13**, 289–297.
- Bartelt, P. and Lehning, M. (2002). A physical SNOWPACK model for the Swiss avalanche warning Part I: numerical model. *Cold Regions Science and Technology*, **35**(3), 123–145.
- Bougamont, M., Bamber, J., and Greuell, W. (2005). A surface mass balance model for the Greenland Ice Sheet. *Journal of Geophysical Research-Earth Surface*, **110**(F4), F04018.
- Braithwaite, R. (1995). Positive degree-day factors for ablation on the Greenland ice sheet studied by energy-balance modelling. *Journal of Glaciology*, **41**(137), 153–160.
- Brock, B., Willis, I., and Sharp, M. (2000). Measurement and parameterization of albedo variations at Haut Glacier d’Arolla, Switzerland. *Journal of Glaciology*, **46**(155), 675–688.
- Colbeck, S. (1993). The vapor diffusion coefficient for snow. *Water Resources Research*, **29**(1).
- Dozier, J. and Frew, J. (1989). Rapid calculation of terrain parameters for radiation modeling from digital elevation data. In *Geoscience and Remote Sensing Symposium, 1989. IGARSS’89. 12th Canadian Symposium on Remote Sensing., 1989 International*, volume 3.
- Dyer, A. (1974). A review of flux-profile relationships. *Boundary-Layer Meteorology*, **7**(3), 363–372.
- Dyurgerov, M. and Meier, M. (2005). *Glaciers and the changing Earth system: a 2004 snapshot*. Institute of Arctic and Alpine Research, University of Colorado Boulder.
- Greuell, W. (2000). Melt-water accumulation on the surface of the Greenland ice sheet: Effect on albedo and mass balance. *Geografiska Annaler. Series A. Physical Geography*, pages 489–498.

BIBLIOGRAPHY

- Greuell, W. and Böhm, R. (1998). 2 m temperatures along melting mid-latitude glaciers, and implications for the sensitivity of the mass balance to variations in temperature. *Journal of Glaciology*, **44**(146), 9–20.
- Greuell, W. and Konzelmann, T. (1994). Numerical modelling of the energy balance and the englacial temperature of the Greenland Ice Sheet. Calculations for the ETH-Camp location (West Greenland, 1155 m a. s. l.). *Global and planetary change*, **9**(1-2), 91–114.
- Greuell, W., Knap, W., and Smeets, P. (1997). Elevational changes in meteorological variables along a midlatitude glacier during summer. *Journal of Geophysical Research-Atmospheres*, **102**(D22).
- Herron, M. and Langway, C. (1980). Firm densification: an empirical model. *J. Glaciol.*, **25**(93), 373–385.
- Hock, R. (1999). A distributed temperature-index ice- and snowmelt model including potential direct solar radiation. *Journal of Glaciology*, **45**(149), 101–111.
- Holtslag, A. and De Bruin, H. (1988). Applied modeling of the nighttime surface energy balance over land. *Journal of Applied Meteorology*, **27**(6), 689–704.
- Houghton, H. (1954). On the annual heat balance of the northern hemisphere. *Journal of the Atmospheric Sciences*, **11**(1), 1–9.
- IPCC (2007). Climate Change 2007: The Physical Science Basis. *Summary for Policy Makers, Contribution of Working Group I to the Fourth Assessment Report of the Intergovernmental Panel on Climate Change*.
- Iqbal, M. (1983). *An introduction to solar radiation*. Academic Press Canada, Ontario, Canada.
- Jacka, T. and Li, J. (1994). The steady-state crystal size of deforming ice. *Annals of Glaciology*, **20**, 13–13.
- Janssens, I., Huybrechts, P., Autor, K., and Huybrechts, P. (2000). The treatment of meltwater retardation in mass-balance parameterizations of the Greenland ice sheet. *Annals of Glaciology*, **31**, 133–140.
- Jordan, R. (1991). A one-dimensional temperature model for a snow cover: Technical documentation for SNTHERM. 89.
- Kimball, B., Idso, S., and Aase, J. (1982). A model of thermal radiation from partly cloudy and overcast skies. *Water resources research*, **18**(4).
- Klok, E. and Oerlemans, J. (2002). Model study of the spatial distribution of the energy and mass balance of Morteratschgletscher, Switzerland. *Journal of Glaciology*, **48**(163), 505–518.
- Klok, E. and Oerlemans, J. (2004). Modelled climate sensitivity of the mass balance of Morteratschgletscher and its dependence on albedo parameterization. *International Journal of Climatology*, **24**(2).

- Klok, E., Greuell, W., and Oerlemans, J. (2003). Temporal and spatial variation of the surface albedo of Morteratschgletscher, Switzerland, as derived from 12 Landsat images. *Journal of Glaciology*, **49**(167), 491–502.
- Kondratyev, K. (1969). Radiation in the atmosphere. *International Geophysics Series*, **12**, 912.
- Konzelmann, T., Van de Wal, R., Greuell, W., Bintanja, R., Henneken, E., and Abe-Ouchi, A. (1994). Parameterization of global and longwave incoming radiation for the Greenland Ice Sheet. *Global and Planetary Change*, **9**(1), 143–164.
- Kuhn, M. (1993). Possible future contributions to sea level change from small glaciers. *Climate and Sea Level Change: Observations, Projections and Implications*, page 134.
- Kuipers Munneke, P., Reijmer, C., van den Broeke, M., König-Langlo, G., Stammes, P., and Knap, W. (2008). Analysis of clear-sky Antarctic snow albedo using observations and radiative transfer modeling. *J. Geophys. Res.*, **113**.
- Li, J. and Zwally, H. (2004). Modeling the density variation in the shallow firn layer. *Annals of Glaciology*, **38**(1), 309–313.
- McDonald, J. (1960). Direct absorption of solar radiation by atmospheric water vapor. *Journal of the Atmospheric Sciences*, **17**(3), 319–328.
- Meier, M. (1965). Glaciers and climate. *The Quaternary of the United States*, **795**, 805.
- Meier, M. (1984). Contribution of small glaciers to global sea level. *Science*, **226**(4681), 1418–1421.
- Meyers, T. and Dale, R. (1983). Predicting daily insolation with hourly cloud height and coverage. *Journal of Applied Meteorology*, **22**(4).
- Munro, D. (1991). A surface energy exchange model of glacier melt and net mass balance. *International Journal of Climatology*, **11**(6).
- Oerlemans, J. (1992). Climate sensitivity of glaciers in southern Norway: application of an energy-balance model to Nigardsbreen, Hellstugubreen and Alftobreen. *J. Glaciol.*, **38**(129), 223–232.
- Oerlemans, J. (2000a). Analysis of a 3 year meteorological record from the ablation zone of Morteratschgletscher, Switzerland: energy and mass balance. *Journal of Glaciology*, **46**(155), 571–579.
- Oerlemans, J. (2000b). Holocene glacier fluctuations: is the current rate of retreat exceptional? *Annals of Glaciology*, **31**, 39–44.
- Oerlemans, J. (2001). *Glaciers and climate change*. Balkema Lisse.
- Oerlemans, J. and Fortuin, J. (1992). Sensitivity of glaciers and small ice caps to greenhouse warming. *Science*, **258**(5079), 115–117.

BIBLIOGRAPHY

- Oerlemans, J. and Grisogono, B. (2002). Glacier winds and parameterisation of the related surface heat fluxes. *Tellus A*, **54**(5), 440–452.
- Oerlemans, J. and Hoogendoorn, N. (1989). Mass balance gradients and climatic change. *J. Glaciol*, **35**(121), 399–405.
- Oerlemans, J. and Klok, E. (2004). Effect of summer snowfall on glacier mass balance. *Annals of Glaciology*, **38**, 97–100.
- Oerlemans, J. and Knap, W. (1998). A 1 year record of global radiation and albedo in the ablation zone of Morteratschgletscher, Switzerland. *Journal of Glaciology*, **44**(147), 231–238.
- Oerlemans, J., Giesen, R., and Van Den Broeke, M. (2009). Retreating alpine glaciers: increased melt rates due to accumulation of dust (Vadret da Morteratsch, Switzerland). *Journal of Glaciology*, **55**(192), 729–736.
- Ohmura, A. (2004). Cryosphere during the twentieth century. *Geophysical monograph*, **150**, 239–257.
- Parry, V., Nienow, P., Mair, D., Scott, J., Hubbard, B., Steffen, K., and Wingham, D. (2007). Investigations of meltwater refreezing and density variations in the snowpack and firn within the percolation zone of the Greenland ice sheet. *Annals of Glaciology*, **46**, 61.
- Reijmer, C. and Hock, R. (2008). Internal accumulation on Storglaciären, Sweden, in a multi-layer snow model coupled to a distributed energy-and mass-balance model. *Journal of Glaciology*, **54**(184), 61–72.
- Rick, U., Rajaram, H., and Pfeffer, T. (2008). Surface Meltwater Runoff and Retention in the Accumulation Zone of the Greenland Ice Sheet. In *American Geophysical Union, Fall Meeting 2008, abstract# C31B-0497*.
- Schneider, T. and Jansson, P. (2004). Internal accumulation in firn and its significance for the mass balance of Storglaciären, Sweden. *Journal of Glaciology*, **50**(168), 25–34.
- Smith, W. (1966). Note on the relationship between total precipitable water and surface dew point. *Journal of Applied Meteorology*, **5**(5), 726–727.
- Sturm, M., Holmgren, J., König, M., and Morris, K. (1997). The thermal conductivity of seasonal snow. *Journal of Glaciology*, **43**(143), 26–41.
- Tribbeck, M., Gurney, R., Morris, E., and Pearson, D. (2004). A new Snow-SVAT to simulate the accumulation and ablation of seasonal snow cover beneath a forest canopy. *Journal of Glaciology*, **50**(169), 171–182.
- Van de Wal, R., Oerlemans, J., and Van der Hage, J. (1992). A study of ablation variations on the tongue of Hintereisferner, Austrian Alps. *J. Glaciol*, **38**(130), 319–324.
- Van den Broeke, M., van As, D., Reijmer, C., and van de Wal, R. (2004). Assessing and improving the quality of unattended radiation observations in Antarctica. *Journal of Atmospheric and Oceanic Technology*, **21**(9), 1417–1431.

- Van den Broeke, M., Reijmer, C., Van As, D., and Boot, W. (2006). Daily cycle of the surface energy balance in Antarctica and the influence of clouds. *International Journal of Climatology*, **26**(12), 1587–1606.
- Winther, J. (1993). Short- and Long-Term Variability of Snow Albedo. *Nordic Hydrology NOHYBB*, **24**(2), 199–212.
- Yen, Y. (1981). *Review of thermal properties of snow, ice and sea ice*. U.S. Army, Corps of Engineers, Cold Regions Research and Engineering Laboratory.
- Zuo, Z. and Oerlemans, J. (1996). Modelling albedo and specific balance of the Greenland ice sheet: calculations for the Sondre Stromfjord transect. *Journal of Glaciology*, **42**(141), 305–317.
- Zwally, H. and Li, J. (2002). Seasonal and interannual variations of firn densification and ice-sheet surface elevation at the Greenland summit. *Journal of Glaciology*, **48**(161), 199–207.